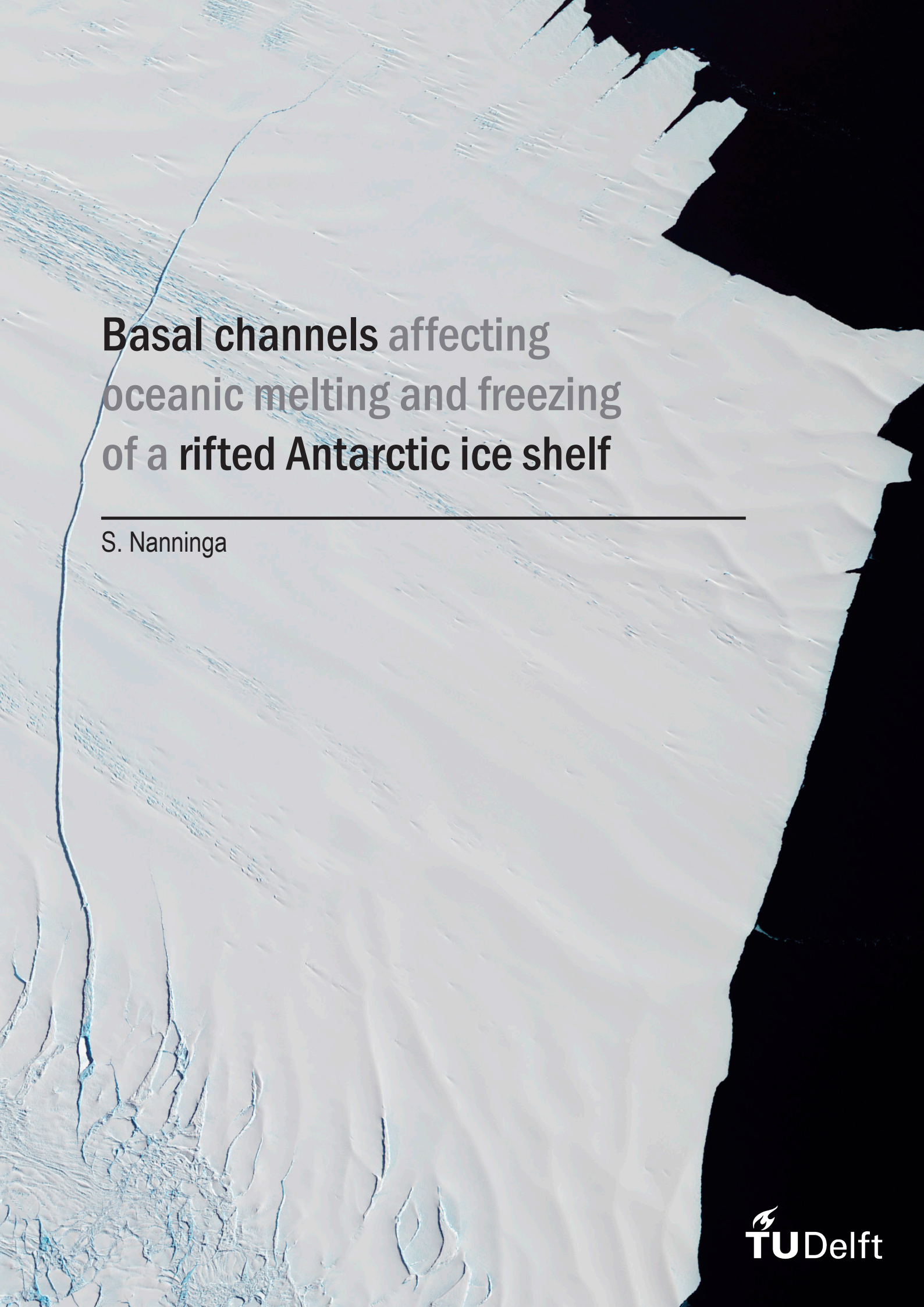

Basal channels affecting oceanic melting and freezing of a rifted Antarctic ice shelf

S. Nanninga

TU Delft

Basal channels affecting oceanic melting and freezing of a rifted Antarctic ice shelf

by

S. (Stefanie) Nanninga

In partial fulfilment of the requirements for the degree of

Master of Science

in Civil Engineering

at Delft University of Technology,
to be defended publicly on Friday the 4th of November 2022, 03:00 PM.

Student number:	4555236	
Thesis committee:	Dr. M. Vizcaino (chair),	TU Delft
	Ir. M. Poinelli (supervisor),	TU Delft, University of California & NASA JPL
	Prof. Dr. C.A. Katsman,	TU Delft

An electronic version of this thesis is available at http://repository.tudelft.nl/.

On the cover: Rift on Pine Island Glacier - November 13, 2011 - NASA Earth Observatory image created by Jesse Allen, using data provided courtesy of NASA/GSFC/METI/ERSDAC/JAROS, and U.S./Japan ASTER Science Team.

TU Delft

Preface

Dear reader,

This work contains the reporting of my graduation work, the final requirement to obtain my Master of Science degree in Civil Engineering. As I followed the track of Hydraulic Engineering, I could further explore my interest in earth sciences. Hence, as a master student, I developed a great appreciation for the interconnection between the Earth's atmosphere and ocean.

As a lot of physical processes on earth are not yet understood, the beauty of numerical modelling is that you have a chance to use your creativity to study them. This is one of the many things I learned from Mattia Poinelli, who I want to thank for the daily supervision of my research process. Although we never physically met and our schedules were eight hours of time difference apart, you showed me the interesting field of ice-ocean modelling and encouraged me to explore the possibilities of MITgcm. I would also like to thank my other two committee members, Miren Vizcaino and Caroline Katsman, for their enthusiasm and feedback. You taught me that research is not only about the actual results, but also about how you present and formulate your findings. I would like to thank my family for their endless support and interest in my work, which is encouraging. Lastly, I would like to thank my friends, who made my time as a student one never to forget.

Stefanie Nanninga
Delft, November 2022

Abstract

Floating ice shelves regulate Antarctic ice sheet mass loss by buttressing land ice discharge toward the ocean. Next to basal melting, iceberg calving following the propagation of rifts has the potential to reduce this buttressing effect. However, rift propagation is largely unpredictable and generally not resolved in coarse climate models. The sub-shelf ocean circulation is believed to play an important role in rift propagation as it is closely related to ice shelf melting and freezing. Previous work suggests that the sub-shelf circulation of an intact ice shelf is altered by the presence of km-wide basal channels. As it could impact freezing and melting, the potential effect of basal channels on a rifted Antarctic ice shelf should be explored.

In this study, the Massachusetts Institute of Technology general circulation model was applied to explore for the first time the potential effect of basal channels on the melting and freezing of a rifted Antarctic ice shelf. To this end, four simulations were performed with a high-resolution ocean model for the domain of an ice shelf cavity with idealized boundary conditions. These simulations correspond to a cavity with melt channels, a prominent rift close to the ice shelf front, both, and none of them. The effects of channels, a rift or the combination of both on melt, freezing and ocean circulation in the cavity were assessed through a comparison of these four simulations. Following previous research, results show that basal channels decrease ice shelf basal melting. We found that the addition of only a rift does not change the melt intensity or pattern. In addition, it was found that basal channels increase the freezing inside a rift. A sub-shelf boundary current on the Coriolis favoured side of the domain without channels is reformed to a clockwise circulation in each channel, resulting in an adjusted flow pattern inside the rift from one single large clockwise return flow to a smaller one behind each channel. Hence, buoyant cold shelf meltwater does not only enter the rift in the boundary current but after every topographic incision, and the thermal forcing is increased. Furthermore, the multiple return flow pattern enlarges the average frictional velocity inside the rift, which is positively related to the freezing rate intensity. In an offline calculation, it was found that the contribution of the thermal forcing to the total freezing amount is approximately three times larger than the friction velocity.

From our simulations, we conclude that the presence of basal channels in a rifted ice shelf decreases basal melting at the grounding line and increases freezing inside rifts. Previous work on rift propagation suggests that these results imply that marine ice accretion inside the rift could increase, and fracture propagation could be reduced. Given these connections between ice shelf processes, this study stresses the importance of including basal channels and rifts in ice shelf cavity models to robustly reproduce Antarctic sub-shelf circulation and basal melt.

Contents

Preface iii

Abstract v

Nomenclature x

List of Figures xii

1 Introduction 1
- 1.1 Scientific background . . . 2
  - 1.1.1 Uncertainty in sea level rise projections . . . 2
  - 1.1.2 Antarctic Ice Sheet mass loss . . . 3
  - 1.1.3 Oceanic circulation forcing Antarctic ice shelf change . . . 4
  - 1.1.4 Rift propagation impacted by the cavity circulation . . . 8
  - 1.1.5 Cavity circulation altered by basal channels . . . 10
- 1.2 Research objective . . . 11
- 1.3 Outline & approach . . . 12

2 Methodology 13
- 2.1 MITgcm equations and set-up . . . 14
  - 2.1.1 Oceanic equations of motion . . . 14
  - 2.1.2 Hydrostatic pressure assumption . . . 16
  - 2.1.3 Equation of state . . . 16
  - 2.1.4 Forcing and dissipation of momentum . . . 16
  - 2.1.5 Diffusion of temperature and salinity . . . 17
  - 2.1.6 Ice-ocean interaction . . . 17
  - 2.1.7 Packages . . . 19
  - 2.1.8 Numerical schemes . . . 19
- 2.2 Model domain . . . 19
  - 2.2.1 Domain size & spatial resolution . . . 19
  - 2.2.2 Bathymetry . . . 19
  - 2.2.3 Ice-ocean interface . . . 19
  - 2.2.4 Partial cell formulation . . . 21
- 2.3 Initial & boundary conditions . . . 22
  - 2.3.1 Reference data: Thwaites Ice Shelf . . . 23
  - 2.3.2 Initial conditions . . . 24
  - 2.3.3 Boundary conditions . . . 25
- 2.4 Temporal resolution . . . 26
  - 2.4.1 Time step . . . 26
  - 2.4.2 Quasi-steady state . . . 27
  - 2.4.3 Three-monthly mean . . . 27
- 2.5 Diagnostics . . . 27
  - 2.5.1 Parameters . . . 27
  - 2.5.2 Area definitions . . . 28
- 2.6 Runs . . . 29

3 Results 31
- 3.1 Mean basal melting and freezing rates . . . 32
  - 3.1.1 Annual mean freshwater flux . . . 32
  - 3.1.2 Mean freezing rate . . . 32
  - 3.1.3 Summary mean melting/freezing results . . . 33

3.2 Melting/freezing & horizontal flow pattern . . . 34
3.2.1 Ice shelf basal surface . . . 34
3.2.2 Inside and in the proximity of the rift . . . 39
3.2.3 Summary freshwater flux and flow pattern results . . . 39
3.3 Influence channels on freezing rate inside the rift . . . 42
3.3.1 Three-equation freezing rate calculation . . . 42
3.3.2 Contribution heat transfer coefficient and thermal forcing . . . 44
3.3.3 Summary freezing rate rift results . . . 45

4 Discussion **47**
4.1 Model evaluation . . . 48
4.1.1 Basal melt rate evaluation . . . 48
4.1.2 Rift and melt channel evaluation . . . 48
4.2 Result analysis . . . 49
4.2.1 Rifted ice shelf basal melting affected by basal channels . . . 49
4.2.2 Basal channels altering circulation in and around rift . . . 50
4.2.3 Basal channels altering freezing inside rift . . . 51
4.2.4 Summary . . . 52
4.3 Implications & further research . . . 52

5 Conclusions and recommendations **55**
5.1 Conclusions . . . 56
5.2 Recommendations . . . 57
5.2.1 Basal channels and rifts in ice shelf cavity models . . . 57
5.2.2 Return flow at the ocean boundary in ice shelf cavity models . . . 57
5.2.3 A 3D plume model explicitly modelling frazil ice . . . 57
5.2.4 Non-hydrostatic modelling . . . 58
5.2.5 Variation in initial and boundary conditions . . . 58
5.2.6 Variation in channel geometry . . . 58
5.2.7 Monitoring of mélange and ice shelf thickness in the presence of channels . . . 58

Bibliography **62**

A MICI & MISI **63**

B Isomorphic equations of motion **65**

C Derivation maximum crest depth **67**

D Derivation sine function channel cross-section **69**

E Reference measurements initial and boundary conditions **71**

F Salinity time series **73**

Nomenclature

Abbreviations

$AABW$	Antarctic Bottom Water
ACC	Antarctic Circumpolar Current
$ADCP$	Acoustic Doppler Current Profiler
AIS	Antarctic Ice Sheet
AP	Antarctic Peninsula
$AR6$	Sixth Assessment Report
ASC	Antarctic Slope Current
CDW	Circumpolar Deep Water
CTD	Conductivity Temperature Depth
DNS	Direct Numerical Simulation
$EAIS$	Eastern Antarctic Ice Sheet
EAP	Eastern Antarctic Peninsula
GIA	Glacial Isostatic Adjustment
$GMSL$	Global Mean Sea Level
HPE	Hydrostatic Primary Equations
$HSSW$	High Salinity Surface Waters
$IPCC$	Intergovernmental Panel on Climate Change
ISW	Ice Shelf Water
LES	Large Eddy Simulation
$MICI$	Marine Ice Cliff Instability
$MISI$	Marine Ice Sheet Instability
$MITgcm$	Massachusetts Institute of Technology general circulation model
MOC	Meridional Overturning Circulation
$NADW$	North Atlantic Deep Water
$RANS$	Reynolds-averaged Navier Stokes
SH	Southern Hemisphere
$WAIS$	Western Antarctic Ice Sheet
WAP	West Antarctic Peninsula

Greek symbols

ϵ_{nh}	non-hydrostatic parameter	–
η	stability parameter	–
γ_S	turbulent exchange coefficient salinity	ms^{-1}
γ_T	turbulent exchange coefficient temperature	ms^{-1}
$\kappa_{I,T}$	thermal diffusivity	m^2s^{-1}
ν	kinematic viscosity sea water	m^2s^{-1}
ρ	density	kgm^{-3}
ρ^*	density integrated over the ice shelf base	kgm^{-3}
ρ_c	constant reference density	kgm^{-3}
ρ_I	density ice	kgm^{-3}
ρ_o	density water	kgm^{-3}
θ	potential temperature	°C
ξ_N	stability constant	–

Other symbols

$\Delta L_{x,y,z}$	spatial resolution	m
Δt	time step	s

$\hat{k}$	unit vector in the vertical	–
$\vec{\mathbf{v}}$	velocities u, v and w	ms^{-1}
$\vec{\mathbf{v}}_h$	horizontal velocity u and v	ms^{-1}
A_4	horizontal biharmonic friction	m^4s^{-1}
A_h	lateral viscosity	m^2s^{-1}
A_v	vertical viscosity	m^2s^{-1}
C	Courant number	–
$c_{\mathrm{p,I}}$	specific heat capacity of the ice shelf	$Jkg^{-1}K^{-1}$
c_p	specific heat at constant pressure	$Jkg^{-1}K^{-1}$
c_d	drag coefficient	–
d_c	channel crest depth in longitudinal direction	m
d_k	ice shelf base in longitudinal direction	m
$d_{c,max}$	maximum crest depth	m
$d_{c,x}$	channel crest depth in cross shelf direction	m
f	Coriolis parameter	$rads^{-1}$
g	gravitational constant	ms^{-2}
h	height ice shelf base	m
k	Von Kármán constant	–
K_4	horizontal biharmonic diffusion	m^4s^{-1}
K_h	horizontal diffusion	m^2s^{-1}
$K_{\mathrm{v,S}}$	vertical eddy diffusivity salinity	m^2s^{-1}
$K_{\mathrm{v,T}}$	horizontal eddy diffusivity temperature	m^2s^{-1}
K_v	vertical diffusion	m^2s^{-1}
k_a	shape factor	–
k_b	shape factor	–
k_c	shape factor	–
k_d	shape factor	–
L_q	latent heat	Jkg^{-1}
$N_{channel}$	channel number	–
p	pressure	Pa
p_0	constant reference pressure	mbar
p_b	pressure at ice base	dbar
p_a	atmospheric pressure	Pa
Pr	Prandtl number	–
q_i	ice shelf freshwater flux	$myear^{-1}$
q_{ocean}	oceanic freshwater flux	$kgm^{-2}s^{-1}$
R	gas constant dry air	$Jkg^{-1}K^{-1}$
S	salinity	PSU
S_I	ice shelf salinity	PSU
S_b	salinity boundary layer	PSU
T	temperature	°C
t	time	s
T_b	temperature boundary layer	°C
T_f	freezing point temperature	°C
T_s	surface temperature ice shelf	°C
u	horizontal cross shelf velocity	ms^{-1}
u_*	friction velocity	ms^{-1}
v	horizontal along shelf velocity	ms^{-1}
w	vertical velocity	ms^{-1}
$x_{channel,max}$	channel width	m
x_{tot}	cross shelf width of the domain	m
z	depth	m

List of Figures

1.1 Primary contributors to sea level rise and how sea level rise uncertainties affect coastal protection planning. . . . 2
1.2 A schematized representation of the AIS and details of its two main mass loss processes. 3
1.3 The global atmospheric and oceanic circulations. . . . 5
1.4 Adjusted figure of the Antarctic ice-shelf ice-thickness change rate Δ T/Δt in the period of 2003–2008, together with the estimated average sea-floor potential temperatures (in °C) from the World Ocean Circulation Experiment Southern Ocean Atlas (pink to blue), as shown in Pritchard et al., 2012. The figure is overlain with the Antarctic bathymetry in dark grey. Light grey circles show relative ice losses for ice-sheet regions in the period of 1992-2006. The dotted lines highlight the Antarctic Peninsula (AP) and Western Antarctic Ice Sheet (WAIS). The western part of the AP is called the Western Antarctic Peninsula (WAP) and the eastern part is the Eastern Antarctic Peninsula (EAP). The remaining area is defined as the Eastern Antarctic Ice Sheet (EAIS). The Thwaites ice shelf, referred to in Chapter 2, is indicated with a black dot. . . . 6
1.5 A schematic representation of the near-coast overturning circulation in the Southern Ocean and the relevant water masses for cold and warm water regions. . . . 7
1.6 A theoretical framework of oceanic circulation in the proximity of and inside the cavity, in cold and warm water regions. . . . 8
1.7 An along shelf schematized representation of the circulation in a rift for warm (red) and cold (blue) areas as described by Jordan et al., 2014. . . . 9
1.8 Basal channels observed and mapped by Alley et al., 2016. . . . 10
1.9 Schematized representation of an ice shelf including basal channels. . . . 11

2.1 The ice-ocean interface excluding melt channels and a rift, together with the bathymetry. 20
2.2 A visualisation of the parameters used to define the channel dimensions in the ice-ocean interface. . . . 21
2.3 The ice-ocean interface including 10 melt channels with a maximum depth of 100 [m] and a rift (at n_y[255:259]). Subfigure 2.3(a) shows the top view with the grid point elevation in colours. In 2.3(b), two along shelf sections can be observed. The section at n_x = 100 represents a channel trough and at n_x = 150 a crest. A full 3D visualization is shown in 2.3(c). . . . 22
2.4 Along shelf section of the model, including ten melt channels and a rift, together with initial and boundary conditions. . . . 23
2.5 Potential temperature measured in the deep troughs near the Thwaites Ice Shelf. . . . 24
2.6 The first subfigure from the left shows the Historical S_A vs Θ CTD data from two basins, as given in A. Wåhlin et al., 2021. Information about the meltwater mixing line, winter water and high melt water concentration can be found in A. Wåhlin et al., 2021 and is not further used in this study. The second subfigure from the left gives locations where these salinity and potential temperature combinations were measured. . . . 24
2.7 Velocity recordings using an ADCP. . . . 25
2.8 Monitoring time in days against mean salinity of the domain excluding channels and a rift. 27
2.9 An along shelf section of the parameter areas. . . . 28

3.1 The four runs mentioned in section 2.6 against the resulting freshwater flux [m/year], the average of all the ice-ocean boundary melting and freezing rates. . . . 32
3.2 Mean freezing rates [m/year] for the four runs as introduced in section 2.6. These rates are calculated as the average of all negative melt rates on the ice-ocean boundary. . . . 33

3.3 A contour plot of the ice shelf freshwater flux in the boundary layer for base run N_0r_0, together with the horizontal velocity vector pattern at the first grid point beneath the ice-ocean interface (2.5.2). To obtain a proper visualisation, only every fifth value of the diagnostics is shown. 35
3.4 A contour plot of the ice shelf freshwater flux in the boundary layer for run N_0r_2, together with the horizontal velocity vector pattern at the first grid point beneath the ice-ocean interface (2.5.2). To obtain a proper visualisation, only every fifth value of the diagnostics is shown. 36
3.5 A contour plot of the ice shelf freshwater flux in the boundary layer for run $N_{10}r_0$, together with the horizontal velocity vector pattern at the first grid point beneath the ice-ocean interface (2.5.2). To obtain a proper visualisation, only every fifth value of the diagnostics is shown. The locations of the channel troughs are indicated with green lines. 37
3.6 A contour plot of the ice shelf freshwater flux in the boundary layer for run $N_{10}r_2$, together with the horizontal velocity vector pattern at the first grid point beneath the ice-ocean interface (2.5.2). To obtain a proper visualisation, only every fifth value of the diagnostics is shown. The locations of the channel troughs are indicated with green lines. 38
3.7 A detail of contour plot 3.4 containing the ice shelf freshwater flux in the boundary layer for run N_0r_2, together with the horizontal velocity vector pattern at the first grid point beneath the ice-ocean interface (2.5.2). In contrast with figure 3.4, all the diagnostics values are shown. 40
3.8 A detail of contour plot 3.6 containing the ice shelf freshwater flux in the boundary layer for run $N_{10}r_2$, together with the horizontal velocity vector pattern at the first grid point beneath the ice-ocean interface (2.5.2). In contrast with figure 3.6, all the diagnostics values are shown. The locations of the channel troughs are indicated with green lines. . 41

4.1 An illustration of the sub-shelf circulation along the base of a rifted ice shelf without and with ten basal channels. 51

A1 Schematized representation of MICI and MISI. 63

D1 A visualisation of the parameters used to define the channel dimensions used in the ice-ocean interface. 70

E1 Detail of a figure in A. Wåhlin et al., 2021: regions of interest in A. Wåhlin et al., 2021. . 72

F1 Monitoring time in days against mean salinity of the domain for run N_0r_2 (F.1(a)), $N_{10}r_0$ (F.1(c)) & $N_{10}r_2$ (F.1(e)). Detail from day 250 until day 1825 for run N_0r_2 (F.1(b)), $N_{10}r_0$ (F.1(d)) & $N_{10}r_2$ (F.1(f)). 74

1

Introduction

An introduction is given to the research topic, starting with the background information in section 1.1. The objective (section 1.2) shows the main goal of the study, and the questions to be answered. Section 1.3 describes the outline of the thesis and research approach.

1.1. Scientific background

This section describes the importance and background of the research topic. First, the uncertainty in global sea level rise projections is explained (subsection 1.1.1). As it is one of the important drivers of this uncertainty, current knowledge about Antarctic Ice Sheet mass loss is presented in subsection 1.1.2. Antarctic Ice Sheet mass loss is governed by the oceanic circulation, trough basal melting and iceberg calving, described in subsection 1.1.3. Subsection 1.1.4 presents further information on the relatively unexplored impact of oceanic circulation on rift propagation before iceberg calving. Current knowledge about the presence of basal channels potentially altering this circulation is given in subsection 1.1.5.

1.1.1. Uncertainty in sea level rise projections

Driven by economic and population growth, greenhouse gas emission has been increasing drastically since the pre-industrial era while forcing the global climate to change [Shukla et al., 2022b]. The atmosphere and ocean are warming, snow and land ice mass are shrinking, and the global mean sea level (GMSL) is rising [Pachauri and Meyer, 2014]. GMSL rise is related to near-shore sea level rise and potentially requires coastal protection planning as flooding, shoreline erosion and storm hazards are enhanced [Hinkel et al., 2010]. Since a large part of the world's population and food production is situated in low-lying coastal areas, GMSL rise is one of the most important and threatening consequences of anthropogenic climate change [Portner et al., 2019] and has been for a long time [Vellinga and Leatherman, 1989].

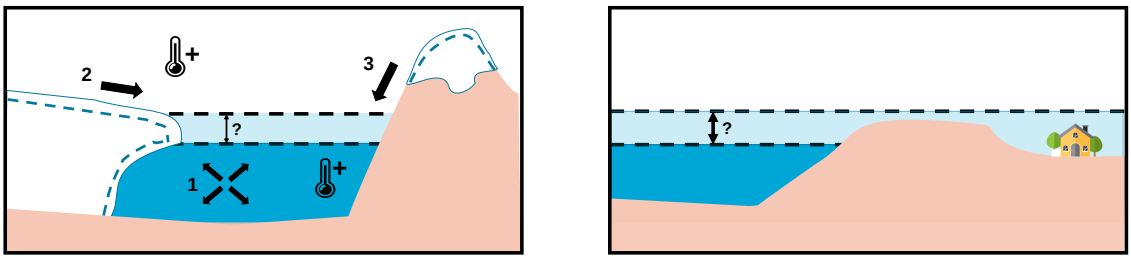

(a) (b)

Figure 1.1: (a) Primary contributors to sea level rise due to a warming ocean and atmosphere (represented by thermostats): thermal expansion of the ocean (1) and land ice mass loss. Land ice mass loss originates from ice sheets (2) and glaciers (3). The influence of Glacial Isostatic Adjustment [Peltier, 1999] and gravitational effects are neglected in this figure. (b) An illustration of how sea level rise uncertainties affect coastal protection planning.

GMSL rose 0.20 meters between 1901 and 2018, with an acceleration since the late 1960s [Shukla et al., 2022a]. Figure 1.1(a) shows the current primary contributors to sea level rise because of a warming ocean and atmosphere. The influence of Glacial Isostatic Adjustment (GIA) [Peltier, 1999] and gravitational effects on sea level rise are neglected in this figure, as this study focuses on sea level rise as a result of global warming since the pre-industrial era. Primary contributors [Portner et al., 2019] were the thermal expansion of the ocean [McKay et al., 2011] (figure 1.1(a), 1), together with land ice mass loss from ice sheets [Rignot et al., 2019] (figure 1.1(a), 2) and glaciers [Marzeion et al., 2014] (figure 1.1(a), 3). Thermal expansion was the dominant contributor in the 20th century. However, ice-sheet mass loss increased by a factor of four between 1992 and 2019, thereby causing GMSL rise to be dominated by land ice mass loss during the early 21st century [Shukla et al., 2022b].

In the longer term, the sea level will continue to rise and be elevated for thousands of years [Clark et al., 2016]. Accurate global predictions by numerical climate models are therefore an important part of designing durable coastal protection and mitigation measurements [Bamber et al., 2019]. Future emission rates remain however unknown and cause a large uncertainty in model projections and required coastal protection measurements, as illustrated in figure 1.1(b). The Intergovernmental Panel on Climate Change (IPCC) describes five possible emission scenarios in the Sixth Assessment Report (AR6) [Shukla et al., 2022a], varying from low to high greenhouse gas rates, to explore the

corresponding global warming and sea level rise intensities. When regarding the two most extreme scenarios, GMSL is expected to rise over the next 200 years within a range of 0.3 - 3.1 meters (very low emission, warming limited to ~1.5 °C) to 1.7 - >15 meters (very high emissions, warming of ~4.5 °C) relative to 1900. Sea level rise thus does not only vary greatly between but also within scenarios, an uncertainty partly caused by Antarctic Ice Sheet (AIS) mass loss [Portner et al., 2019].

Between 2006 and 2015, the AIS lost an ice volume equivalent to ~0.43 millimetres of sea level rise per year [Portner et al., 2019]. The IPPC AR6 [Shukla et al., 2022a] projects that the AIS will be responsible for 0.07-0.37 meters (low emission) to 0.60-2.89 m (high emission) of sea level rise by 2300, with respect to 1900. Under sustained high greenhouse gas emissions, Antarctica might contribute even more than the mentioned ranges. Sea level rise of 7-14 meters cannot be ruled out due to two potential AIS instability processes with rapid and large mass loss: Marine Ice Sheet Instability (MISI) and Marine Ice Cliff Instability (MICI) (Appendix A). The contribution of the AIS to GMSL rise is thus under strong scientific debate [Haasnoot et al., 2020], partly because of a limited understanding of its mass loss processes [Shukla et al., 2022b]. The present-day knowledge of AIS mass loss is discussed below.

1.1.2. Antarctic Ice Sheet mass loss

An ice sheet is a glacial land ice mass that covers more than 50,000 square kilometres [NSIDC, 2021]. Figure 1.2 shows a schematized representation of the AIS and its ice flow; and its main mass loss processes. The AIS gains mass by accumulating snowfall in compact and dense layers of ice (figure 1.2, 1). Under its weight, this is channelled downwards through a network of glaciers and ice streams toward the ocean into outlet glaciers [Shepherd et al., 2018] (figure 1.2, 2). The outlet glaciers move ice out to the ocean, where it might break off to form an iceberg. If an iceberg is not directly formed, glacier ice loses contact with the bathymetry and becomes a floating ice shelf (figure 1.2, 3) instead. Ice shelves can be up to 2500 m thick, cover up to 500,000 km^2 [Dinniman et al., 2016], and fringe about 75 % of the Antarctic coastline [DeWeerdt, 2019]. The point of detachment is called the grounding line (figure 1.2, 4) [Bentley et al., 2007], and the area beneath the ice shelf is referred to as the cavity. The upstream discharge is restrained by the ice shelves, reducing the rate at which snow and ice propagate to the ocean (figure 1.2, 5), an effect that is also known as buttressing [Fürst et al., 2016].

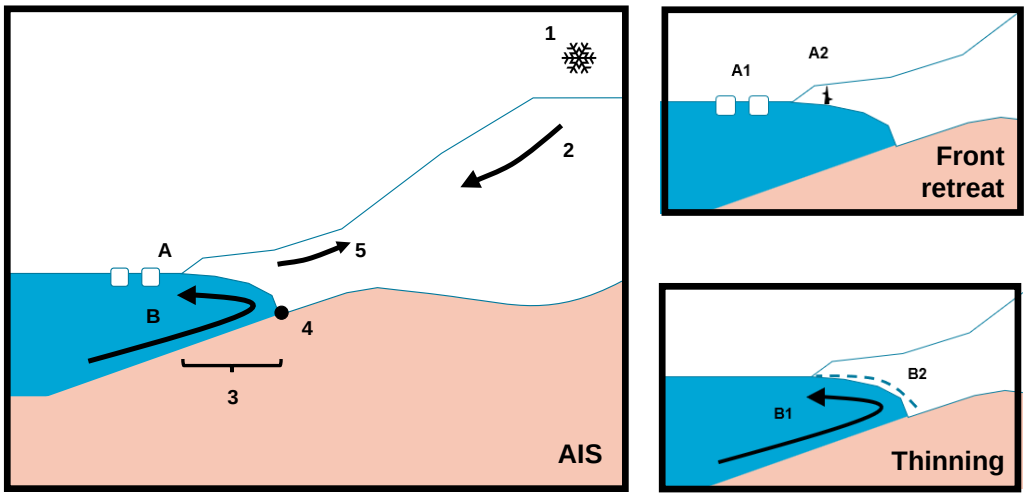

Figure 1.2: A schematized representation of the AIS (left) and details of its two main mass loss processes (right). Ice sheet features and processes are: snowfall (1), glacier and ice stream flow (2), ice shelf (3), grounding line (4), buttressing effect (5), ice shelf front retreat (A), iceberg calving (A1), rift (A2), ocean circulation within the cavity (B), oceanic heat exchange within the cavity (B1) and ice shelf basal thinning (B2).

Ice sheets can lose mass to the ocean both in the form of meltwater and solid ice discharge [Bentley et al., 2007]. Meltwater originates from atmospherically forced surface run-off and ice shelf basal melting by the ocean [Lenaerts et al., 2019]. Surface run-off in Antarctica is negligible, due to the relatively cold atmosphere and a high re-freezing rate [Huybrechts and De Wolde, 1999]. The AIS primarily loses mass through oceanic forced ice shelf change, in the form of solid ice discharge (figure 1.2, A) and basal melting by the ocean circulation within the cavity (figure 1.2, B). Since ice shelves are floating, their presence does not directly influence sea level rise. However, as ice shelves support the upstream flow by the buttressing effect, their change can accelerate inland glaciers and ice streams that flow into the sea [Pritchard et al., 2012]. Mass loss through solid ice consists of the earlier-mentioned flow of glaciers and ice streams toward the ocean, which results in iceberg formation (figure 1.2, A1). Icebergs follow the propagation of rifts (figure 1.2, A2; subsection 1.1.4): through-surface fractures in the ice shelf. The formation of an iceberg is also known as calving [Lenaerts et al., 2019] and leads to a frontal retreat of the ice shelf. Oceanic heat exchange within the cavity (figure 1.2, B1) [Fahnestock et al., 2001; Pritchard et al., 2012] occurs at the base of the ice shelves when the sea temperature is higher than the freezing point at a certain depth and thins the ice shelf (figure 1.2, B2).

Ice shelf thinning and frontal retreat thus govern AIS mass loss. Both processes are influenced by the circulation in the cavity, thermally as well as dynamically, as they are a result of oceanic forcing. Ice shelf thinning is directly impacted by the thermal and dynamic forcing of the ocean. Thermally refers to the temperature of the ocean influencing basal melting, where a warmer ocean results in a higher melt rate [Pritchard et al., 2012]. Since the velocity magnitude is positively related to basal melting intensity, the dynamical impact is also relevant [Millgate et al., 2013]. Frontal retreat could be altered as the circulation possibly influences the propagation of rifts [Larour et al., 2021], a more unexplored process that is further discussed in 1.1.4. Additionally, thinning and frontal retreat might cause mutual enhancement: ice shelf thinning possibly leads to an increase in iceberg calving [Liu et al., 2015] and basal melting could enlarge linearly with frontal retreat [Bradley et al., 2022]. It must be mentioned that a more recent study by Larour et al., 2021 contradicts the finding by Liu et al., 2015 that ice shelf thinning enhances frontal retreat. Although the influence of cavity circulation on ice shelf change is thus an important factor in AIS mass loss, it is not fully understood. Before discussing unknown processes, first theoretical frameworks for the oceanic circulation outside and ultimately the resulting circulation inside the cavity are presented below.

1.1.3. Oceanic circulation forcing Antarctic ice shelf change

The Antarctic oceanic circulation is partially forced by the global atmospheric circulation through the formation of meridional surface winds [Turner et al., 2009]. Since the equator yearly receives about five times as much radiation as the poles, a temperature difference arises in the atmosphere [Trenberth and Caron, 2001]. Due to this equator-to-pole temperature difference, the warm air flows to the colder regions at high altitudes. A schematized representation of the global atmospheric circulation is shown in figure 1.3(a). The red (blue) arrows represent the flow of warm (cold) air. As air rises (sinks) low (high) pressure systems are formed, represented with L (H). As Antarctica is the area of interest in this study, further description of the atmospheric circulation focuses on the Southern Hemisphere (SH). Under the influence of the Coriolis force, imposed by the rotational movement of the Earth, the equator-to-pole flow deflects to the left in the SH until it reaches the maximum point of deflection; at 30 °S, 60 °S, and 90 °S latitude. In combination with mass conservation, this results in the formation of the Hadley, Ferrel, and Polar cells respectively (figure 1.3(a)). The deflecting surface flows under influence of the Coriolis force result in three types of meridional surface winds: Tropical Easterlies (0-30 °S), Westerlies (30-60 °S) & Polar Easterlies (60-90 °S) [Turner et al., 2009]. The westerlies and polar easterlies force local winds around the Antarctic continent that play an important role in the global oceanic and near-shore circulation, processes that are further described below.

Figure 1.3(b) shows a schematic representation of the global oceanic circulation, the Meridional Overturning Circulation (MOC). The explanation of the MOC in this study will emphasise the central role of the Southern Ocean, as this is the area of interest. The Atlantic, Pacific, Indian, and Southern Ocean basins are shown in grey. Transport of water masses between the four basins occurs due to density differences and the meridional surface winds. The density of sea water increases with a

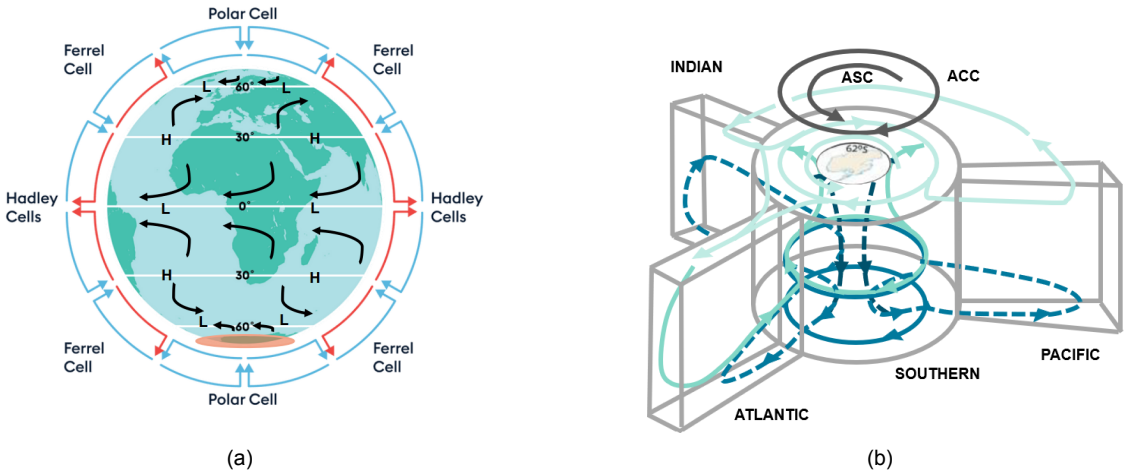

(a) (b)

Figure 1.3: The global atmospheric (a) and oceanic (b) circulations. (a) A schematized representation of the global atmospheric circulation, altered from a figure by encounteredu.com, 2022, including the three types of circulation cells: the Hadley, Ferrel, and Polar Cells. Where air rises (sinks) low (high) pressure systems occur, represented by L (H). The arrows represent the cell circulation, where red represents warm and blue cold air. Three types of surface winds are shown in black arrows: Tropical Easterlies (0-30 °), Westerlies (30-60 °) & Polar Easterlies (60-90 °). The location of Antarctica is highlighted in orange. (b) A schematized representation of the MOC while emphasizing the role of the Southern Ocean, based on a figure by Turner et al., 2009. The figure shows the four ocean basins in grey: the Indian, Pacific, Atlantic, and Southern Oceans. The upper cell of the MOC is shown in light blue & turquoise. The lower part of the overturning circulation is given in turquoise and dark blue. The sinking of AABW is indicated in navy. The ACC and ASC are represented by a grey circle and a semi-enclosed circle respectively.

decreasing temperature, and with a higher salinity [Buckley and Marshall, 2016]. The water warms at the equator in the Indian, Pacific, and South Atlantic Oceans; and cools near the poles in the Southern and North Atlantic Oceans. The motion of the water masses is initiated by the Southern Hemisphere westerlies that force the Antarctic Circumpolar Current (ACC), shown as a dark grey circle in figure 1.3(b). The ACC is a major eastward flowing current enclosing the continent [Turner et al., 2009]. Under the influence of the Coriolis force, the westerly winds deflect the fresh Antarctic surface water from the ACC towards the other three more northern ocean basins (figure 1.3(b), light blue). Due to mass conservation, upwelling of relatively warm and saline Circumpolar Deep Water (CDW) originating from the Atlantic, Pacific and Indian Oceans replaces the surface waters near the Antarctic coastline (figure 1.3(b), turquoise). It must be noted that the nuance between CDW and North Atlantic Deep Water (NADW) is neglected in this explanation, and can be found in Turner et al., 2009. The deflected surface waters eventually cool off and increase in density in the Arctic part of the Atlantic Sea, after which they sink. The resulting overturning motion represents the upper part of the MOC [Lumpkin and Speer, 2007] (figure 1.3(b), light blue and turquoise). The circulation of the lower cell of the MOC is initiated by the formation of Antarctic Bottom Water (AABW). AABW consists of High Salinity Surface Waters (HSSW), very saline water with a temperature equal to that of the surface formed during sea ice formation [Grumbine, 1991], and CDW. Due to the high salinity and therefore density of the CDW and HSSW, the water masses partially cascade down along the continental shelf as AABW [Orsi et al., 1999] (figure 1.3(b), navy) while, together with the upwelling of CDW, forcing the lower overturning cell of the MOC [Lumpkin and Speer, 2007] (figure 1.3(b), turquoise and dark blue). Besides becoming AABW, CDW and HSSW can also reach into ice shelf cavities. In contrast with HSSW, the ability of CDW to enter the cavity is variable along the continent. The difference in CDW intrusion into an ice shelf cavity is generally caused by the local influence of the Antarctic Slope Current (ASC) (figure 1.3(b), dark grey semi-enclosed circle) [Nakayama et al., 2021]. The ASC, forced by the polar easterlies, is a westward flowing surface current close to and along a large part of the Antarctic coastline [Thompson et al., 2018]. Under the influence of Coriolis, surface water transport occurs southwards in the direction of the coastline. The ASC can thus locally counterbalance the near-coast northward transport and CDW upwelling by the ACC. Since the CDW is relatively warm, near-coast sea-floor temperatures and ocean circulation are also locally variable.

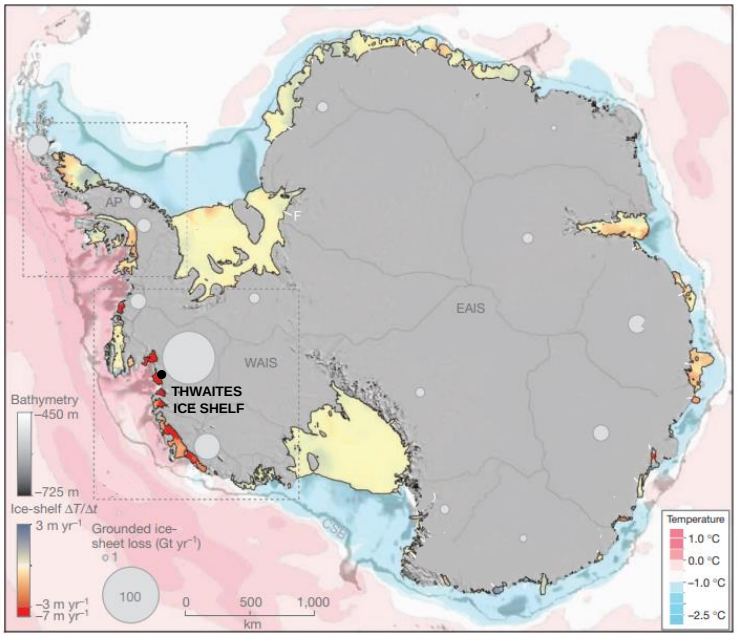

Figure 1.4: Adjusted figure of the Antarctic ice-shelf ice-thickness change rate Δ T/Δt in the period of 2003–2008, together with the estimated average sea-floor potential temperatures (in °C) from the World Ocean Circulation Experiment Southern Ocean Atlas (pink to blue), as shown in Pritchard et al., 2012. The figure is overlain with the Antarctic bathymetry in dark grey. Light grey circles show relative ice losses for ice-sheet regions in the period of 1992-2006. The dotted lines highlight the Antarctic Peninsula (AP) and Western Antarctic Ice Sheet (WAIS). The western part of the AP is called the Western Antarctic Peninsula (WAP) and the eastern part is the Eastern Antarctic Peninsula (EAP). The remaining area is defined as the Eastern Antarctic Ice Sheet (EAIS). The Thwaites ice shelf, referred to in Chapter 2, is indicated with a black dot.

Figure 1.4 shows a map of Antarctica and its bathymetry where the three main regions are indicated: the Antarctic Peninsula (AP), the Western Antarctic Ice Sheet (WAIS) and, the Eastern Antarctic Ice Sheet (EAIS). The average near-coast seabed temperature is shown from warm to cold (pink to blue) in °C. From figure 1.4 it can be observed that the ocean seabed temperature shows a bimodal distribution around the Antarctic continent. CDW is warm and saline, and so are the seabeds near ice shelves to where it has uninhibited access. Figure 1.4 shows that waters near the WAIS & WAP are warm, in contrast with waters near the East Antarctic Ice Sheet (EAIS) & Eastern Antarctic Peninsula (EAP). Mean temperature and salinity magnitudes observed in cold Antarctic regions (EAIS & EAP), at the seabed for depths shallower than 1500 m for the period 1975 to 2012, were ranging from -1.0 - -2.0 °C and 34.45 - 34.95 PSU. In warm regions (WAIS & WAP), observations of 1.0 - 1.4 °C and 34.65 - 34.9 PSU were common [Schmidtko et al., 2014]. The intensity and influence of the ASC are minor in the Western Antarctic Peninsula (WAP) and West Antarctic Ice Sheet (WAIS) (1.4) due to three features: the topography of the Antarctic Peninsula, a local difference in the strength of the easterlies and the locations of two major near-coast gyres. As the Antarctic Peninsula extends northward, into latitudes dominated by the ACC, the ASC is not circumpolar. The surface currents at the WAP and WAIS are therefore mainly influenced by the ACC. The easterly winds above the two western Antarctic seas, the Bellingshausen and the Amundsen Sea, are also relatively weak. Furthermore, the WAP and WAIS regions largely reside outside of areas controlled by the clockwise circulating Weddell and Ross Gyres that also deflect near-coast surface water to the south under the influence of Coriolis. Next to the seabed temperature, figure 1.4 also shows light grey circles that represent the relative ice sheet losses in ice shelf regions from 1992 to 2006 in thickness over time ($\Delta T/\Delta t$). Furthermore, the ice shelf mass loss or gain in meters per year is indicated with a colour spectrum from red to blue respectively. It can be observed that ice sheet mass loss is generally larger in regions with warm seabed temperatures (WAP & WAIS)[Pritchard et al., 2012], where CDW enters the ice shelf cavity. This rapid retreat increases the possible occurrence of MICI and MISI (Appendix A), making especially WAIS and WAP potential contributors to sea level rise [Portner et al., 2019]. To emphasize the difference in warm and cold water regions, a schematic section of the near-coast overturning circulation in the Southern Ocean and the relevant water masses is given in figure 1.5. A darker colour blue represents a higher sea water

density. Black arrows represent the flow of the different water masses. The upper dots visualize the ACC and ASC, where a cross refers to a wind traveling in and a dot to a wind traveling out of the page. It must be noted that figure 1.5 shows a schematization of the average ice shelf in these regions and does not cover local variations caused by for example shelf geometry and bathymetry [Wen et al., 2010]. Figure 1.5(a) shows the circulation in a cold water region. The ASC partially counteracts the northern transport of surface waters by the ACC, preventing upwelling of warm CDW near the ice shelf cavity. Only HSSW, formed during the freezing of sea ice, enters the cavity. Figure 1.5(b) represents the circulation in a warm water region, where upwelling of CDW by the ACC is not counteracted by the ASC. Therefore, a combination of HSSW and CDW enters the cavity. Figure 1.5(a) and 1.5(b) both also show the dense AABW cascading down along the continental shelf. As the near-coast ocean circulation differs between warm and cold water regions, the cavity circulation and thus the affected ice shelf change does as well. The ice shelf cavity circulation for warm and cold water regions is described below.

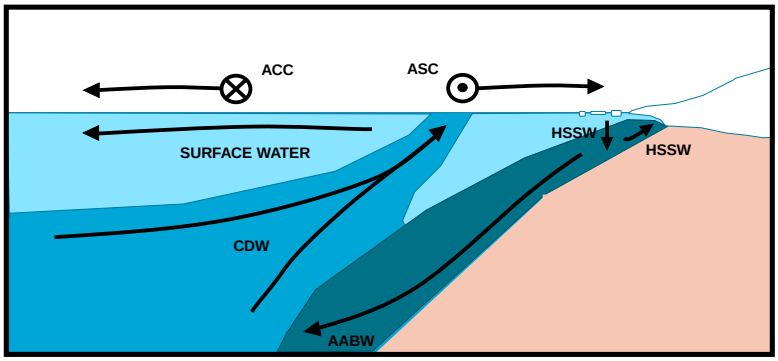

(a)

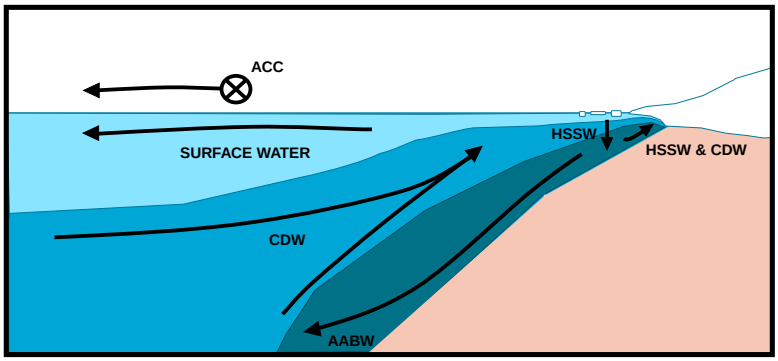

(b)

Figure 1.5: A schematic representation of the near-coast overturning circulation in the Southern Ocean and the relevant water masses for cold (a) and warm (b) water regions. An ice shelf is shown on the right-hand side of both sub-figures. Turner et al., 2009 is used as a reference. However, the nuance between CDW and NADW is neglected. The shades of blue represent the density differences between the water masses. A darker blue corresponds with a higher density. The black arrows show the flow of the water masses. (a) The overturning circulation in cold water regions is dominated by the ACC and ASC. The upper dots represent the ACC and ASC, where the cross refers to the wind flowing into the page and the circle to the wind traveling out of the page. The arrows from the dots visualize the transport of surface waters by Coriolis deflection of the ACC and ASC. (b) In contrast with cold water regions, the overturning circulation in warm water regions is solely dominated by the influence of the ACC. The cross refers to the wind traveling into the page and the black arrow to the transport of surface waters under Coriolis deflection.

Like outside the cavity, the circulation inside the cavity is driven by density differences between entering and leaving water masses [Hellmer and Olbers, 1989]; and wind forcing. The circulation in the proximity of and inside the ice shelf cavity of cold and warm water regions is visualized in figure 1.6, together with the ice shelf change processes and the buttressing effect. The ACC and ASC are again represented by a cross or dot, depending on whether the wind travels out of or into the paper respectively. The flow of a water mass is indicated with a black arrow in the water. Furthermore, basal melting is indicated with a blue dotted line. Iceberg calving is represented by fracture formation in the ice and the buttressing effect by a large black arrow in the ice shelf. Depending on whether the ice shelf is situated in a cold (figure 1.6(a)) or warm (figure 1.6(b)) region, only HSSW or HSSW in combination with CDW enters the cavity respectively. As discussed above, upwelling of CDW by the ACC near the ice shelf cavity is prevented in cold water regions by the ASC. Both CDW and HSSW are more saline and therefore denser than fresh cavity water. Since the system is horizontally stratified, dense HSSW and CDW flow beneath the fresh cavity water towards the grounding line or sink along the continental shelf as AABW. As the freezing point of sea water is pressure-dependent, it decreases (gets closer to zero) with increasing pressure and depth. Both water masses are warmer than the freezing point near the grounding line: HSSW since it maintained a temperature comparable to that of surface water, and CDW since it originates from the warmer Atlantic, Pacific, and Indian Oceans. Ice Shelf Water (figure 1.6, ISW) forms during basal melting (1.6, basal melting), which is cold and fresh, and rises along the ice shelf base towards the front. Basal melting continues under this rising motion. When the buoyant plume has reached the in-situ freezing point, marine ice forms, and saline water is ejected again. This saline water is dense, therefore sinks and joins the circulation. In literature, this mechanism is often referred to as 'the ice pump' [Lewis and Perkin, 1983]. Since in warm water regions the ice pump is forced by HSSW and CDW, instead of only HSSW, basal melting is more intense. This is presumed to be one of the reasons for the relatively large ice sheet mass loss in the WAIS and WAP. In addition to basal melting, iceberg calving following rift propagation could also potentially be influenced by cavity circulation [Larour et al., 2021]. However, this process is relatively unexplored. Current knowledge is discussed below.

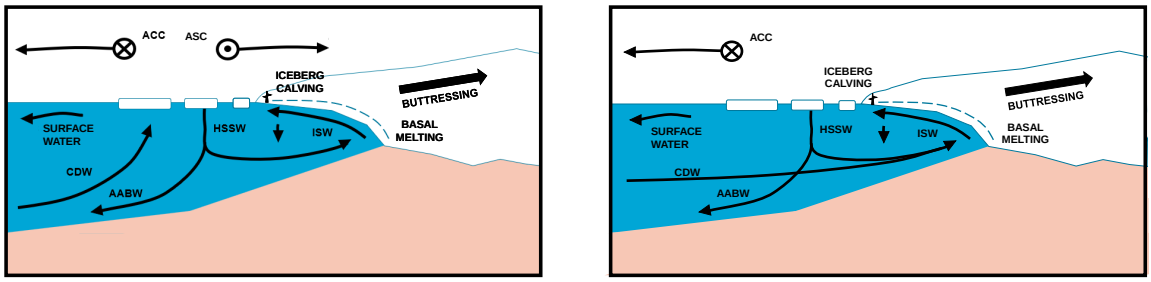

(a) (b)

Figure 1.6: A theoretical framework of oceanic circulation in proximity of and inside the cavity, in the cold (a) and warm (b) water regions. Both figures include the shelf retreat processes, iceberg calving, and basal melting. Furthermore, the buttressing effect is visualized. (a) Oceanic circulation in cold water regions is dominated by the ACC and ASC. The ACC and ASC are represented with dots, where the cross refers to the wind flowing into the page and the circle to the wind traveling out of the page. Transport of surface waters forced by a Coriolis deflection to the left in the Southern Hemisphere results in surface waters being partially deflected offshore and partially onshore. Only HSSW reaches into the cavity, not CDW. (b) In warm regions, a significant difference is the uninhabited access of CDW to the cavity due to the absence of ASC preventing near-coast upwelling. Therefore, CDW can comparably reach the ice shelf as the HSSW.

1.1.4. Rift propagation impacted by the cavity circulation

Rifts observed all around the Antarctic continent [Walker et al., 2013], are m- to km-wide fractures that propagate over the full width and through the entire thickness of the ice shelf. Eventually, rifts become boundaries where icebergs detach from the shelf. The direction of propagation can be along shelf, but cross shelf is more commonly observed [Heeszel et al., 2014]. Internal glaciological stress - stress induced by the gravitational spreading of the ice - largely dominates rift formation [Joughin and MacAyeal, 2005;J. N. Bassis et al., 2008]. Glaciological stress is believed to also promote rift

propagation, in addition to tidal and wind stresses [J. N. Bassis et al., 2008]. Tidal currents bend the ice [Rosier and Gudmundsson, 2018]. Furthermore, strong winds can exert a substantial frictional drag force on the ice shelf surface. Nevertheless, fracture propagation is a relatively unexplored process, especially the potential influence of the oceanic circulation implied by previous studies, as the small-scale km-wide rifts are often not resolved in coarse climate models.

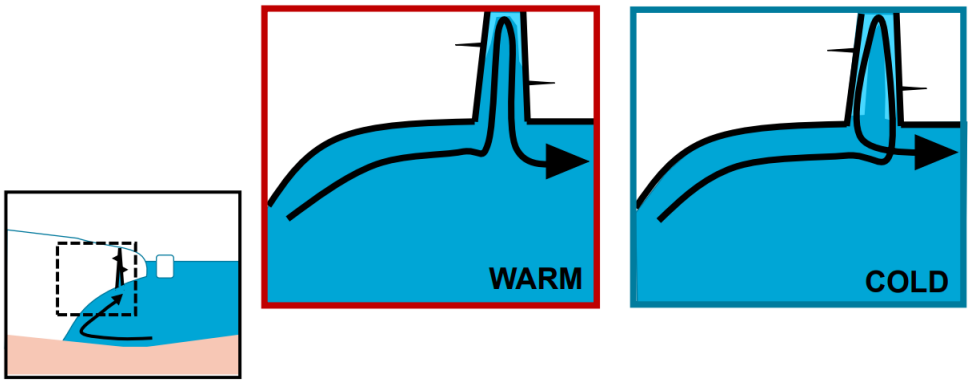

Figure 1.7: An along shelf schematized representation of the circulation in a rift for warm (red) and cold (blue) areas as described by Jordan et al., 2014. Light blue illustrates freezing in the rift. The black arrow represents sub-shelf circulation.

Several studies [Larour et al., 2004, J. Bassis et al., 2005, Hulbe, 1998] suggest that the episodic character of rift propagation is controlled by ice mélange formation at the top of the rift. Mélange is a mixture of iceberg fractures, snow, and frozen marine ice [Amundson et al., 2020]; and can become thick, mechanically resistant, and cohesive when it accumulates and freezes over time. Fracture propagation can therefore be ceased [Larour et al., 2004], possibly slowing down ice sheet mass loss through frontal retreat. A study by Khazendar and Jenkins, 2003 indicates that cavity circulation can facilitate the accretion of marine ice, a component of mélange. Marine ice is defined by Khazendar and Jenkins, 2003 as a body of ice that forms because of the consolidation of small floating frazil ice crystals. Frazil ice crystals are formed when heat is withdrawn from water in a turbulent state at its freezing point. As described by the plume model of Khazendar and Jenkins, 2003, cavity circulation (1.1.3) facilitates the accretion of marine ice formation due to melt-driven convection at the rift sides. Fresh ice shelf water rises into the rift due to buoyancy while melting the sides, after which it freezes as marine ice at higher altitudes due to the pressure and height dependency of the freezing point. The type of circulation that occurs in the rift due to the melt-driven convection is more closely studied with a 2D model by Jordan et al., 2014. Figure 1.7 shows with black arrows two types of along shelf rift circulation. Which type of circulation occurs depends on the ocean temperature. Two types of vertical flow patterns are distinguished: freeze- (cold, figure 1.7) and melt-driven (warm, figure 1.7). In cold areas, a freeze-driven circulation is formed. After buoyant meltwater rises along the ocean side of the rift, this motion is driven by strong freezing at the top due to the pressure dependency of the freezing point. As latent heat and salinity are released, a dense layer of sea water is formed. The relatively dense water in the top of the rift causes an unstable overturning circulation, where the flow cascades downwards at the grounding line side of the rift. In warm areas, less freezing and dense water production occurs. The circulation in the rift is then primarily driven by meltwater rising on the grounding line side before sinking on the ocean side. The melt-driven movement is faster and more stable than the freeze-driven. Hence, cavity circulation is believed to be important for marine ice accretion inside rifts in warm and cold water regions but the freezing intensity differs. As marine ice is a component of mélange, fracture propagation could potentially be delayed. Recent studies imply that the cavity circulation of an intact ice shelf can be altered by the presence of basal channels [Millgate et al., 2013; Gladish et al., 2012]. This process might also impact the circulation beneath a rifted ice shelf, and therefore potentially fracture propagation. The current knowledge of basal channels is further discussed below.

1.1.5. Cavity circulation altered by basal channels

Irregularities of the ice shelf base enlarged by concentrated oceanic melting initiate the formation of km-wide regularly spaced sub-ice shelf channels, orientated in the direction of the ice flow [Gladish et al., 2012]. Such an incision originates from the grounding line side, where the HSSW and/or CDW melt the ice shelf as described in subsection 1.1.3, and terminates at the ocean side of the ice shelf. Channel formation has also been linked to the release of subglacially released meltwater: buoyant freshwater outflow beneath the ice sheet [Alley et al., 2016]. Alley et al., 2016 mapped and documented Antarctic basal melt channel characteristics with typical sizes of 1-5 km across and 50-250 m deep in the ice shelf base measured with satellite imagery, airborne ice-penetrating radar and satellite laser altimetry from 2002 to 2014, as shown in figure 1.8. Figure 1.8 shows an Antarctic map including bathymetry, mean seabed near-shore temperature from warm to cold (red to blue) and the main seas with their corresponding longitude segregation. They distinguish three channel categories, based on the formation mechanism: ocean- (figure 1.8, navy dot), subglacially- (figure 1.8, green dot), and grounding line-sourced (figure 1.8, light blue dot). Depending on whether the CDW and HSSW melt the shelf at the grounding line or above, grounding line- or ocean-sourced channels are formed. Subglacially-sourced channels occur due to freshwater outflow from the ice sheet near the grounding line. From figure 1.8 it can be observed that channel formation largely occurs in WAIS and WAP, warm water regions. This observation can be explained by the uninhibited access of CDW to the shelf base, which favours channel carving (1.1.3). Furthermore, figure 1.8 highlights areas where channels possibly occur but could not be confirmed given the available data with orange dots. Lastly, Alley et al., 2016 identified polynyas (figure 1.8, red triangle) - stretches of open water surrounded by sea ice near the shelf front - which are believed to be an indication of basal channel presence [Bindschadler et al., 2011;Mankoff et al., 2012]. The coloured arrows in figure 1.8 show examples of measurement types. As ice shelf change is governed by oceanic circulation, this study neglects subglacially-sourced channels. Furthermore, recent studies by Millgate et al., 2013 and Gladish et al., 2012 focus on understanding the physical processes of grounding line-sourced channels observed near the Petermann Gletscher's Ice Shelf in Greenland. Therefore, this research builds further on their obtained knowledge by neglecting ocean-sourced channels.

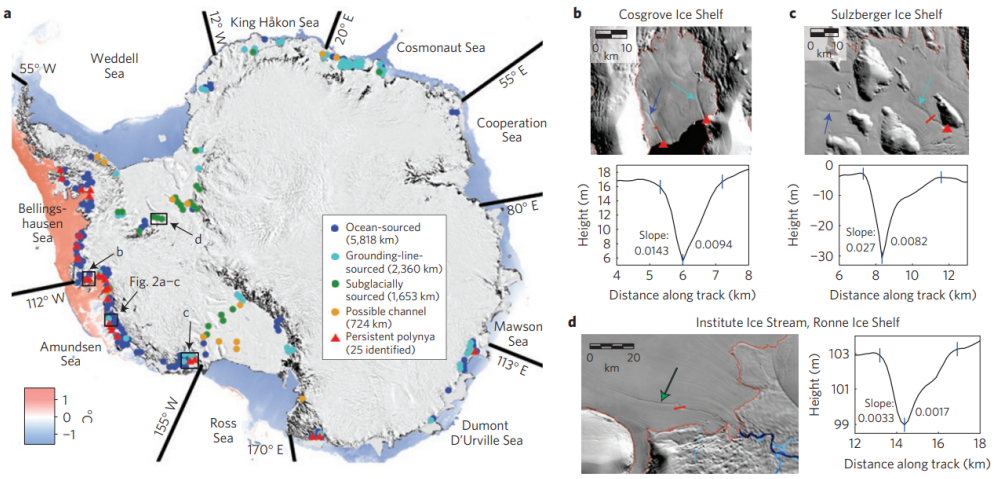

Figure 1.8: Basal channels observed and mapped by Alley et al., 2016 (a). Alley et al., 2016 five types of channel characteristics with different colours. Three characteristics depend on the channel's formation mechanism: ocean-sourced (dark blue), grounding line-sourced (light blue), and subglacially-sourced (green). The orange dots represent possible channels. Furthermore, persistent polynya's that are believed to be indicators of channel presence are highlighted with red triangles. The seabed near-shore temperature is given from warm to cold (red to blue) and the main Antarctic seas are shown. Sub-figures (b), (c), and (d) show details of channel geometry. The arrows indicate channel types.

Due to the spatial dimension, basal channels are also often not resolved in coarse climate models. Nevertheless, numerical 3D ice shelf models of Millgate et al., 2013 and Gladish et al., 2012 imply that grounding line-sourced channels observed in Greenland impact ice shelves by reducing basal melting. Basal melt channels alter the sub-shelf circulation pattern [Stanton et al., 2013], where flow velocity strength is related to the melting/freezing intensity. Figure 1.9 shows a schematized representation of

an ice shelf including basal channels. An example of a cross shelf section where channels are included is shown in section A, where the crests are indicated with turquoise and the troughs with light green. The cavity circulation along the ice shelf base horizontal plane (section B) is given for three scenarios: no channels, wide channels, and narrow channels. The black arrows represent the circulation in the horizontal plane. Without the incisions, intense melting would coincide with a strong boundary current (figure 1.9, no channel), from the grounding line towards the ocean, on the Coriolis favoured side of the ice shelf. Channels redistribute the flow to a return flow in each channel. The type of circulation depends on the channel width, where wide channels cause a horizontal (figure 1.9, wide) and narrow channels a vertical return flow (1.9, narrow). Strong currents and melting then occur on the channel flanks, in contrast with the crests where so-called no-flow regions arise. The no-flow regions then contain little melting, potentially resulting in a lower mean basal mass loss rate [Millgate et al., 2013]. Basal channel presence thus alters the cavity circulation of an intact ice shelf, indicating that a comparable process could also occur beneath a rifted ice shelf.

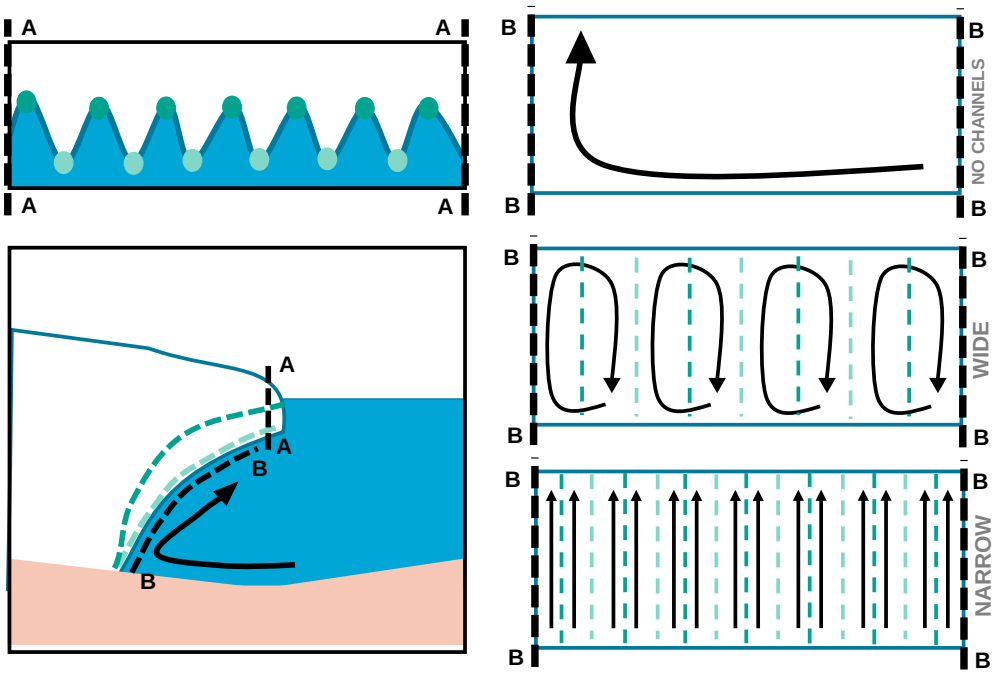

Figure 1.9: Schematized representation of an ice shelf including basal channels. The location of channel crests is indicated with turquoise and troughs with light green. Section A shows a cross shelf section with seven channels in the ice shelf base. Section B is a section along the ice shelf base and is given for three scenarios: no channels, wide channels, and narrow channels. The wide channel example contains four channels and the narrow channel example seven. The arrows beneath the shelf refer to the circulation in the horizontal plane as described by Millgate et al., 2013.

1.2. Research objective

Previous work showed that basal channels alter the cavity circulation of an intact ice shelf. A study exploring the potential effect of basal channels on a rifted Antarctic ice shelf is however still missing and could advance process understanding of cavity circulation. Since the sub-shelf flow pattern is potentially altered, the circulation inside the rift and therewith ice accretion might be impacted as well. As for an intact ice shelf, a decrease in basal melting could occur. Since the sub-shelf circulation thus potentially impacts processes related to ice shelf change, the presence of basal channels on a rifted ice shelf could influence its buttressing capacity. This potential impact is possibly important for Antarctic ice sheet mass loss as basal channels mainly occur in warm water regions like the WAIS and WAP, where ice sheet mass loss is relatively large and instability processes might occur. Hence, the main objective of this research is to gain insight into the potential impact of basal melt channels on the oceanic melting and freezing of a rifted Antarctic ice shelf.

The main research question to be answered is:

What is the effect of basal channels on the oceanic melting and freezing of a rifted Antarctic ice shelf?

To answer the main research question, multiple sub-questions are proposed. Millgate et al., 2013 show that melt channels alter the oceanic circulation beneath an intact ice shelf, and therefore basal melting decreases. For a rifted ice shelf, a potential decrease in basal melting could occur as well but this effect is not explored yet. Therefore, it should first be determined whether the basal melting of a rifted ice shelf is also decreased by the presence of melt channels. The resulting first sub-question is:

- What is the effect of basal channels on the oceanic melting of a rifted ice shelf?

Basal channels alter the oceanic circulation beneath an intact ice shelf. If this takes place beneath a rifted ice shelf, the circulation inside and in the proximity of the rift might change as well. The corresponding sub-question to be answered is:

- What is the influence of basal channels on the circulation inside and in the proximity of the rift?

The circulation beneath an ice shelf is related to melting and freezing intensities. If the circulation inside and in the proximity of the rift would be altered by the presence of melt channels, the freezing in the rift would also be impacted. Therefore, the third sub-question is:

- How is the oceanic freezing inside the rift altered by basal channels?

1.3. Outline & approach

In this study, the Massachusetts Institute of Technology general circulation model (MITgcm) is applied to answer the research questions. A detailed description of the methodology is presented in Chapter 2. As this study investigates the potential impact of basal channels on a rifted ice shelf for the first time, the research uses an idealized ice shelf model to investigate physical processes. As basal channels are mainly observed in warm water regions, which are also more sensitive to potential instability processes, the model will represent an ice shelf in a warm water region. The three-dimensional model includes a simplified ice shelf from the grounding line to the front over the full width of the domain. Only the inclusion of a rift and basal channels in the ice-ocean interface will be varied. One rift width, channel number, and channel dimension are chosen. An open ocean, tides and, seasonality are excluded. The cavity circulation will be forced by a return flow placed at the ocean boundary. A simplified bathymetry is applied, and the model is of high spatial resolution to allow for the addition of the km-wide rift and basal channels. Four sensitivity runs are performed, where the ice-ocean interface includes basal channels, a rift, both, and none. These simplifications suit the goal of this study: to determine a qualitative description of the physical processes potentially caused by basal channel presence on a rifted Antarctic ice shelf. With this approach, key physical processes of interest are distinguished from specific cases influenced by varying bathymetry, seasonality, tides, and ice shelf geometry. The computational time, which can be long for high-resolution ice shelf models, is also limited. As previous studies showed that basal channels affect the melting, freezing, and oceanic circulation of an ice shelf, these physical aspects of the sensitivity runs are compared to answer the sub-questions and ultimately the main research question. These model results are shown in Chapter 3. The model evaluation, result analysis, and implications are given in Chapter 4. Chapter 5 contains the conclusions and recommendations.

2

Methodology

To study the influence of basal melt channels on rifted ice shelf melting/freezing, an idealized numerical model representing an ice shelf cavity is applied. The equations behind and set-up of MITgcm, the model used, are discussed in section 2.1. Furthermore, the model domain (section 2.2), initial and boundary conditions (section 2.3), and temporal resolution (section 2.4) are described. Lastly, the returned diagnostics (section 2.5) are discussed after which the sensitivity runs (section 2.6) are proposed.

2.1. MITgcm equations and set-up

MITgcm, the numerical model implemented in this study, has been extensively applied to investigate atmospheric and oceanic phenomena [Adcroft et al., 2008]. The applicability varies from small turbulent to global scale. In this section, the equations of motion for the ocean are discussed (2.1.1). The hydrostatic approximation as applied in this work and the equation of state are described in (2.1.2) and (2.1.3). The forcing and dissipation terms in the momentum equation (2.1.4) and the diffusion of temperature and salinity (2.1.5) are shown. Additionally, the inclusion of the influence of ice on the state of the ocean (2.1.6) is mentioned. Furthermore, the use of several packages (2.1.7) is explained. The numerical schemes used are introduced in subsection 2.1.8.

2.1.1. Oceanic equations of motion

An isomorphic system of hydrodynamical equations represents the evolution of the atmosphere or ocean in time, as described by Marshall et al., 1997. These equations of motion are derived from the three-dimensional Navier-Stokes equations for momentum, the continuity equation, the equation of state, and the conservation equation of salinity and potential temperature. Two types of assumptions are applied that reduce computational time and complexity. The Boussinesq approximation can be used when density variations are small and presumes that variations in density only give rise to buoyancy. In practice, this means that density differences are ignored in all terms in the momentum equations except the ones multiplied by the gravitational constant. A constant reference density ρ_c is assumed in the horizontal momentum equations and the pressure term in the vertical momentum equation. Furthermore, the flow is assumed to be incompressible. The compression or expansion of a fluid goes to zero and the density of a parcel is constant as it moves with the flow. By applying the two assumptions, the incompressible Boussinesq equations in spherical coordinates as shown in Appendix B are obtained.

Since the system of equations is isomorphic, one can solve the atmospheric or oceanic state in time depending on the chosen vertical parameter in the corresponding momentum equation. For an oceanic circulation model, the depth z [m] is chosen [Adcroft et al., 2008]. As MITgcm can be used to study large- and small-scale problems, the most general form of the formulation is given in spherical coordinates. The domain of this study will only cover one ice shelf, which will be smaller than one latitude or longitude. Since the horizontal length scale is much smaller than one latitude or longitude degree [Kundu et al., 2015], a simplified Cartesian system is used [Adcroft et al., 2008]. The assumption implies that the curvature terms in the momentum equations in Appendix B are neglected. Due to this relatively small horizontal length scale, Coriolis can be assumed constant with latitude by using the f-plane approximation [Pietrzak, 2020]. The resulting incompressible Boussinesq oceanic equations of motion in Cartesian coordinates are discussed below.

The oceanic equations of motion are seven expressions with an equal amount of unknowns to solve in time and space: u, v, w, ρ, p, S, and θ.

Horizontal momentum equation

The horizontal momentum equation is:

$$\frac{D\vec{\mathbf{v}}_h}{Dt} + f\hat{k} \times \vec{\mathbf{v}}_h + \frac{1}{\rho_c}\nabla_h p = \vec{\mathcal{F}}_h \qquad \text{(I.2.1.1)}$$

The terms in equation I.2.1.1 represent, from left to right, the total horizontal derivative (consisting of equation I.2.1.2 & I.2.1.3), a Coriolis term, a pressure term, and a forcing term. Further information on the horizontal and vertical forcing can be found in 2.1.4. The variables used are defined as: $\vec{\mathbf{v}}_h$ the horizontal velocity in u and v [m/s], t time [s], $\hat{k}$ the unit vector in the vertical [-], f the Coriolis parameter equal to -1.4 10^{-4} [rad/s], ρ_c a constant reference density of water equal to 1027.5 [kg/m^3], p the pressure [Pa], g the gravitational constant 9.81 [m/s^2] and $\vec{\mathcal{F}}$ the forcing and dissipation of momentum.

The total derivative in equations I.2.1.1, I.2.1.4, I.2.1.8, and I.2.1.9 can be written as:

$$\frac{D}{Dt} = \frac{\partial}{\partial t} + \vec{\mathbf{v}} \cdot \nabla \tag{I.2.1.2}$$

With the expression for the gradient operator as:

$$\nabla = \nabla_h + \nabla_z = \frac{\partial}{\partial x} + \frac{\partial}{\partial y} + \frac{\partial}{\partial z} \tag{I.2.1.3}$$

Vertical momentum equation
Vertical momentum is described as:

$$\epsilon_{\mathrm{nh}} \frac{Dw}{Dt} + \frac{g\rho}{\rho_c} + \frac{1}{\rho_c}\frac{\partial p}{\partial z} = \epsilon_{\mathrm{nh}} \mathcal{F}_w \tag{I.2.1.4}$$

The terms in I.2.1.4 are, from left to right, the total derivative of vertical velocity (consisting of I.2.1.2 & I.2.1.3), the buoyancy term, the pressure term, and the forcing term. Parameter ϵ_{nh} is the non-hydrostatic parameter [-], which is further explained in 2.1.2. The non-constant density is expressed as ρ [kg/m^3].

Continuity equation
The continuity equation, after the application of the incompressible flow assumption, is:

$$\nabla_z \cdot \vec{\mathbf{v}}_h + \frac{\partial w}{\partial z} = 0 \tag{I.2.1.5}$$

With the expression for ∇_z:

$$\nabla_z = \frac{\partial}{\partial z} \tag{I.2.1.6}$$

Equation of state
The equation of state describes the density as a function of potential temperature (θ) and salinity S [PSU].

$$\rho = \rho(\theta, S) \tag{I.2.1.7}$$

A detailed explanation is given in 2.1.3.

Advection-diffusion equations for potential temperature and salinity
The final two equations represent the advection-diffusion of potential temperature (I.2.1.8) and salinity (I.2.1.9):

$$\frac{D\theta}{Dt} = \mathcal{Q}_\theta \tag{I.2.1.8}$$

$$\frac{DS}{Dt} = \mathcal{Q}_s \tag{I.2.1.9}$$

The terms on the left-hand side are the total derivatives, fully written as I.2.1.2. Furthermore, Q is the forcing and dissipation of θ or S. Term Q will be explained in 2.1.5.

2.1.2. Hydrostatic pressure assumption

The horizontal length scale of an ice shelf is generally large compared to the vertical length scale. A model domain with this aspect allows for the neglection of vertical accelerations by applying the hydrostatic pressure assumption. Non-hydrostatic computations are possible, but more suitable for small-scale problems as they are a lot more computationally heavy as well. For MITgcm, applying the hydrostatic pressure assumption implies that the non-hydrostatic parameter ϵ_{nh} in equation I.2.1.4 is zero. The pressure term is then equal to the buoyancy [Adcroft et al., 2008]. The vertical momentum equation I.2.1.4 reduces to the hydrostatic pressure equation:

$$\frac{\partial p}{\partial z} = -g\rho \tag{I.2.1.10}$$

The oceanic equations of motion now represent the Hydrostatic Primary Equations (HPE).

2.1.3. Equation of state

One can calculate the density by applying an equation of state [Pietrzak, 2020]. The expression can be solved by either using a linear or polynomial approximation. The version chosen for this study is a modified UNESCO formula by Jackett and Mcdougall, 1995, which uses the potential temperature and salinity as input. The Boussinesq incompressible form of the equation of state is given by I.2.1.7 and has no pressure dependency. Therefore, the expression reduces to the one-atmosphere equation of state of sea water by Millero and Poisson, 1981:

$$\rho = \rho_0 + AS + BS^{3/2} + CS \tag{I.2.1.11}$$

With ρ the density of sea water in kg/m^3, ρ_0 the density of water 999.8 kg/m^3 and, S the salinity in PSU. The expressions of ρ_0, A, B, and C form a 15-term equation and can be found in Millero and Poisson, 1981. Since there is no pressure dependency, the in-situ temperature t [° C] in the parameters can be replaced by θ [° C] [Jackett and Mcdougall, 1995].

2.1.4. Forcing and dissipation of momentum

Parameter $\vec{\mathcal{F}}_h$ represents the horizontal forcing and dissipation of momentum. The two terms are equal to [Adcroft et al., 2008]:

$$\mathcal{F}_u = D_u + \mathcal{F}_{u,source} = -\nabla_h \cdot (-A_h \nabla_h u) - \frac{\partial}{\partial z}\left(-A_z \frac{\partial u}{\partial z}\right) - A_4 \nabla_h^4 u + \mathcal{F}_{u,source} \tag{I.2.1.12}$$

$$\mathcal{F}_v = D_v + \mathcal{F}_{v,source} = -\nabla_h \cdot (-A_h \nabla_h v) - \frac{\partial}{\partial z}\left(-A_z \frac{\partial v}{\partial z}\right) - A_4 \nabla_h^4 v + \mathcal{F}_{v,source} \tag{I.2.1.13}$$

The terms on the right-hand side of the equations are respectively lateral dissipation, vertical dissipation, biharmonic frictions, and source term. $F_{h,source}$ depends on the chosen forcing, which is further described in 2.3.3.

Expressing the momentum dissipation and friction terms is one of the main challenges of numerical circulation modelling. Flows are often turbulent and therefore unsteady with a large range of motion scales. When one wants to capture all flow scales by using Direct Numerical Simulation (DNS), a fine mesh is required which makes the approach very computationally expensive. Large Eddy Simulation (LES) is a commonly used alternative to DNS, where large-scale eddies of the flow are directly computed and small-scale motions are parameterized. LES uses the knowledge that most of the turbulent kinetic energy is in the large-scale part of the energy spectrum and that dissipation at the small-scale has a low dependence on the large-scale motion. Furthermore, large-scale eddies are highly isotropic whereas small-scale eddies are more homogeneous and easier to model. LES is applied in MITgcm since it is less computationally expensive than DNS but more accurate than the conventional Reynolds-averaged Navier Stokes Approach (RANS), where only the average motion is

solved and the turbulent fluxes are parameterized [Zhiyin, 2015]. A turbulence closure scheme is required to model the sub-grid small-scale motion. A modified Leiht viscosity scheme [Adcroft et al., 2008] is used where the lateral and vertical viscosity coefficients A_h and A_z are equal to 0 [m^2/s]. The forcing/dissipation expressions only depend on the term containing A_4, the horizontal coefficient for biharmonic friction, equal to 2.0 [m^4/s]. This set-up is chosen for model stability.

2.1.5. Diffusion of temperature and salinity

Equations I.2.1.8 and I.2.1.9 represent the advection and diffusion of salinity and potential temperature. The right-hand side of the equation, $\mathcal{Q}_{\theta,S}$, can be derived from the expression below [Adcroft et al., 2008]:

$$D_{T,S} = \nabla \cdot [K\nabla(T,S)] + K_4\nabla_h^4(T,S) + F_{\mathrm{T,S}} \tag{I.2.1.14}$$

The shape of the dissipation equation is similar to that of momentum (I.2.1.12 and I.2.1.13): lateral and vertical dissipation together with biharmonic diffusion. K is the diffusion tensor and K_4 is the horizontal biharmonic diffusion coefficient. Parameters are chosen while using Poinelli, 2022 as a reference, where the biharmonic viscosity is assumed to be zero. Flux $F_{T,S}$ is used to include the effects of an ice shelf and will be discussed in 2.1.6. For the idealized model, the lateral and vertical diffusion coefficients are chosen constant. Matrix K reduces to:

$$K = \begin{pmatrix} K_h & 0 & 0 \\ 0 & K_h & 0 \\ 0 & 0 & K_v \end{pmatrix} \tag{I.2.1.15}$$

K_h is equalized to 0 [m^2/s] and vertical mixing is solved with a Nonlocal K-Profile Parameterization (KPP) scheme [Large et al., 1994]. Vertical eddy diffusivity parameters $K_{v,T}$ and $K_{v,S}$ are equal to $5.44*10^{-7}$ [m^2/s].

It must be noted that the equation of potential temperature [Gill and Adrian, 1982] has to be used to convert D_T to Q_θ.

$$\theta = T\left(\frac{p_0}{p}\right)^{R/c_p} \tag{I.2.1.16}$$

with p_0 the constant reference pressure [mbar], R the gas constant for dry air [J/kg K], and c_p the specific heat at constant pressure [J/ kg K].

2.1.6. Ice-ocean interaction

The SHELFICE package requires a shelf ice topography as additional input next to a regular bathymetry file, which will be discussed in subsection 2.2. The implementation of an ice shelf has two primary consequences: a total pressure adjustment and the use of the three-equation model to resolve the potential temperature and salinity forcing in the advection-diffusion equations (I.2.1.8, I.2.1.9) [Adcroft et al., 2008].

Total pressure in the ocean

The influence of the ice shelf on the total pressure is given in Losch, 2008. The ice on top of the surface will result in additional pressure in the water column. The total pressure in the ocean p_{tot} under the hydrostatic assumption is defined as the sum of the pressure at the top of the water column p_{top} and the hydrostatic pressure:

$$p_{\mathrm{tot}} = p_{\mathrm{top}} + \int_z^{\eta-h} g\rho dz \tag{I.2.1.17}$$

With p_{top} being a combination of the atmospheric pressure p_a (101325 [Pa]) and the weight of the ice shelf depending on an ice density profile ρ^* integrated over the shelf depth h [m]:

$$p_{\text{top}} = p_a + \int_{-h}^{0} g\rho^* dz \tag{I.2.1.18}$$

Three-equation model

The freezing and melting processes create a freshwater flux q_{ocean} (< 0 for freezing) at the base of the ice shelf, which is represented by an infinite small boundary layer between the shelf and the ocean [D. M. Holland and Jenkins, 1999]. A three-equation model is used to determine the temperature T_b [° C] and salinity S_b [PSU] in the boundary layer together with the freshwater flux q_{ocean} [kg/m^2s].

$$\rho_I c_{p,I} \kappa_{I,T} \frac{(T_S - T_b)}{h} = c_p \rho_c \gamma_T (T_b - T) + L q_{\text{ocean}} \tag{I.2.1.19}$$

$$\rho_c \gamma_S (S - S_b) = -q_{\text{ocean}} (S_b - S_I) \tag{I.2.1.20}$$

$$T_f = (0.0901 - 0.0575 S_b) - 7.61 \times 10^{-4} p_b \tag{I.2.1.21}$$

The equations above are the budget for temperature, the budget for salinity, and the expression for the freezing point temperature of sea water T_f [° C] as given by Jenkins et al., 2001. Equation I.2.1.19 is a balance between the diffusive flux from the ice (LHS), advective heat that is carried by the freshwater mass flux (RHS, term 1), and the latent heat flux due to melting and freezing (RHS, term 2). The obtained values are implemented in equation I.2.1.22, to determine the temperature and salinity flux to substitute in the advection-diffusion equations I.2.1.14:

$$F_{T,S} = \left(\rho_c \gamma_{T,S} - q_{\text{ocean}}\right) ((T,S)_b - T,S) \tag{I.2.1.22}$$

T [° C] and S [PSU] are the in-situ temperature, the values at the first ocean grid point close to the ice shelf.

The parameters in the three-equation model and I.2.1.22 must be interpreted as: ρ_I the density of ice 917 [kg/m^3], ρ_c the density of sea water 1027.5 [kg/m^3], $\kappa_{I,T}$ the thermal diffusivity 1.54 10^{-6} [m^2/s], T_S the surface temperature of the ice shelf -20.0 [° C], $(T,S)_b$ the temperature or salinity at the interface [° C, PSU], S_I the salinity of the ice shelf [PSU], $c_{p,I}$ the specific heat capacity of the ice shelf 2000 [J/kg K], γ_S the salinity turbulent exchange coefficient 5.05 10^{-4} [m/s] * γ_T, L_q the latent heat 334 10^3 [J/kg] and p_b the pressure at the ice base [dBar] equal to p_{top} [dBar] (equation I.2.1.18). Generally it is assumed that the salinity of the ice shelf can be neglected (S_I=0).

The heat transfer coefficient γ_T [m/s] is calculated while following the approach of D. M. Holland and Jenkins, 1999:

$$\gamma_T = \frac{u_*}{\Gamma_{\text{Turb}} + \Gamma^T_{\text{Mole}}} \tag{I.2.1.23}$$

$$\Gamma_{Turb} = \frac{1}{k} \ln\left(\frac{u_*^2 \xi_N \eta_\xi^2}{f 5 v}\right) + \frac{1}{2\xi_N \eta_*} - \frac{1}{k} \tag{I.2.1.24}$$

$$\Gamma^T_{\text{Mole}} = 12.5(\text{Pr})^{2/3} - 6 \tag{I.2.1.25}$$

The parameters used are the Von Kármán constant 0.4 [-], the stability constant ξ_N 0.052 [-], the stability parameter η 1 [-], the Coriolis parameter f 1.4*10^{-4} [1/s], the kinematic viscosity of sea water 1.95*10^{-6} [m^2/s] and the Prandtl number 13.8 [-]. Frictional velocity u* [m/s] is calculated with:

$$u_*^2 = c_d \left(u_m^2 + v_m^2\right) \quad \text{(I.2.1.26)}$$

Where c_d is the drag coefficient equal to 0.0021 [-]. Parameters u_m and v_m represent the ocean surface layer velocity components [m/s], which are further discussed in section 2.5. Since Γ^T_{Mole} is a constant value and predominantly large compared to Γ_{Turb} [D. M. Holland and Jenkins, 1999], the heat transfer coefficient is generally linearly related to the frictional velocity:

$$\gamma_T \sim u_* \quad \text{(I.2.1.27)}$$

2.1.7. Packages

Multiple so-called ´packages´ are included in MITgcm and can be added to a model [Adcroft et al., 2008]. Next to the default gfd package, the model in this study includes KPP for vertical mixing (2.1.5). To include boundary conditions, OBCS is applied (2.3.3). To obtain information about the parameters which will be analysed, the diagnostics package is used (2.5). The effect of basal melting underneath a floating ice shelf is included by applying the SHELFICE (2.1.6) package.

2.1.8. Numerical schemes

The equations mentioned in 2.1.1 are solved by applying temporal and spatial discretization schemes [Adcroft et al., 2008]. For the majority of the expressions the default setting is applied, where the temporal scheme is the quasi-second order Adams-Bashforth and the advection scheme is the second order centered finite difference. For the advection of salinity and potential temperature (equations I.2.1.9 & I.2.1.8), the 2^{nd}order Flux Limiter advection scheme is used instead of the second order centered finite difference method for model stability.

2.2. Model domain

MITgcm requires various input files. The chosen domain size (2.2.1) and the applied interfaces (2.2.2 & 2.2.3) are discussed below. Furthermore, the used partial cell formulation is explained (2.2.4).

2.2.1. Domain size & spatial resolution

The chosen domain has the following size: 50 km wide, 80 km long, and 600 meters deep. Since large melt channel dimensions observed in the Antarctic are between 1-5 km across and 50 - 250 deep [Alley et al., 2016], this size is assumed to be sufficient to include the channels. As channels are wider than deep, one can conclude that the vertical resolution should be smaller than the horizontal. The resolution is chosen equal to: dx = dy = 250 m and dz = 10 m. The grid will therefore consist of 200 points in cross shelf direction (x-), 320 points in along shelf direction (y-), and 60 points in depth (z-direction).

2.2.2. Bathymetry

A MITgcm model including an ice shelf requires two input files representing different interfaces: the bed and the ice-ocean interface. Such an input file has the shape of a two dimensional matrix [x,y] representing the z-coordinate. Figure 2.1 shows an along shelf section of the ice-ocean interface and bathymetry, together with a top view of the ice-ocean interface. The bathymetry consist of a simplified retrograding slope, visualized in figure 2.1(a) with orange [Poinelli, 2022].

2.2.3. Ice-ocean interface

The ice-ocean interface, including an ice shelf, is designed while following the approaches of Millgate et al., 2013 and Poinelli, 2022 to implement melt channels and a rift respectively. Although the Millgate et al., 2013 study focuses on modelling basal channels in Greenland with MITgcm, the physical processes are assumed to be comparable.

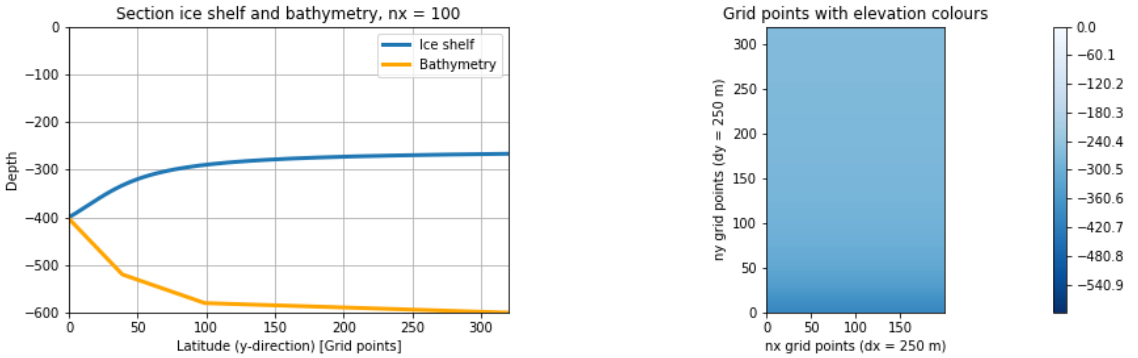

(a) (b)

Figure 2.1: The ice-ocean interface excluding melt channels and a rift, together with the bathymetry. In 2.1(a), one along shelf section can be observed at n_x=100: the ice-ocean interface excluding melt channels and a rift (blue), together with the bathymetry (orange). Subfigure 2.1(b) shows the top view of the ice-ocean interface with the grid point elevation in a colour gradient.

Ice shelf

The ice shelf starts at the grounding line (z = -400 [m], y=0 [km]) and thins towards the surface (z = 0 [m], y= 80 [km]). The shape is constant in cross shelf direction. The ice shelf will cover the full width and length at the top of the domain (z = 0 [m]). The base of the ice shelf follows a tangent function [Millgate et al., 2013]:

$$d_k = k_a \left(\arctan\left(k_b \left(y - k_c\right)\right)\right) - k_d \tag{I.2.2.28}$$

With k_a, k_b, k_c and k_d the shape factors. Because of the vertical grid size, a gentle cavity slope is applied. The parameters are equal to k_a = 75, k_b = 0.025, k_c = 15 and k_d = 375. Parameter d_k is the depth [m] and y the grid points in along shelf direction, both in along-shelf direction. An along shelf section of the ice-ocean interface without a rift or channels is shown in blue in figure 2.1(a). A top view of the ice-ocean interface is given in a colour gradient in figure 2.1(b), where the darker the blue the deeper the interface at that location.

Melt channels

Melt channels can be included in the ice-ocean interface in two steps by following the approach of Millgate et al., 2013. First, an expression for a single channel crest evolution in along shelf direction d_c is derived. The channel crest evolution can be divided into two different shapes. The transition occurs where the maximum channel depth $d_{c,max}$ is assumed to occur. In the idealized model, the $d_{c,max}$ is defined at grid point y = 50. The channel crest depth equations are:

$$d_c = \begin{cases} ay^2 + by + c & \text{if } y \leq 50\ [-] \\ -d + ey & \text{if } y > 50\ [-] \end{cases} \tag{I.2.2.29}$$

The parameter values depend on the chosen maximum channel crest depth $d_{c,max}$, further explained in section 2.6. After the along shelf evolution of a single channel is defined, an expression for total multi-channel shape in the x,y,z-plane is determined. The cross shelf shape of the melt channels will follow a sine function.

$$d_{c,x} = \frac{d_c - d_k}{2} \sin\left(\frac{2\pi}{\Delta x_{channel,max}}\left(x - \frac{3\Delta x_{channel,max}}{4}\right)\right) + \left(d_k + \frac{d_c - d_k}{2}\right) \tag{I.2.2.30}$$

A full derivation of the expression is given in Appendix D. Parameter x represents the grid points in cross shelf direction. The definitions are also visualized in figure 2.2. The channel profile in cross

shelf direction is black, the maximum crest depth is orange, the cavity base is green and the width of one channel is blue. For a single model run the total width of the domain will be fixed, together with the maximum crest height $d_{c,max}$. Melt channels are assumed to cover the full width of the cross shelf domain, which is following Millgate et al., 2013. Due to these assumptions, the channel width and steepness will depend on the channel number. The channel width is defined as:

$$x_{channel,max} = \frac{x_{tot}}{N_{channel}} \tag{I.2.2.31}$$

Where x_{tot} = 200 [grid points] and $N_{channel}$ the number of channels. The chosen number of channels is discussed in section 2.6.

The depth of the ice shelf base for a run without melt channels will be equal to the average value of the channel crest and base.

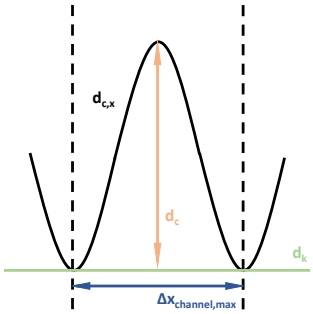

Figure 2.2: A visualisation of the parameters used to define the channel dimensions in the ice-ocean interface: $d_{c,x}$ is the channel profile in cross shelf direction, $d_{c,max}$ the maximum crest depth, d_k is the cavity base, and $\Delta x_{channel,max}$ the width of one channel. One channel is defined from trough to trough.

Rift

A rift can be added by including a shallow area in the ice-ocean interface [Poinelli, 2022]. A rectangular shape of -15 [m] deep, approximately 2 [km] wide along-shelf and uniform in cross shelf direction shows the rift. The top of the rift area is enclosed by along shelf grid points 255 till 262 [63.75 - 65.50 km] and the bottom of the rift by 254 till 263 [63.50 - 65.75 km]. Therefore, the rift is on average 2 km wide. The 15 meters of ice shelf is a schematized representation of ice mélange. Currently, MITgcm does have the option to include an accurate representation of mélange. Therefore, in this study the approximation is made that mélange is of the same composition as the ice shelf although it is softer and warmer [Larour et al., 2021].

An ice-ocean interface including melt channels and a rift is shown together with the bathymetry in figure 2.3. Subfigure 2.3(a) shows the top view of the ice-ocean interface with the grid point elevation in a blue colour spectrum. The darker the blue the deeper the ice-ocean interface at that gridpoint. Subfigure 2.3(b) gives two along shelf sections of the ice-ocean interface and one of the bathymetry (orange). An along shelf section of a channel crest (trough) is visualized in pink (blue). A 3D visualization of the ice-ocean interface (black to pink through blue) and bathymetry (orange) is given in subfigure 2.3(c), where the rift is indicated with yellow and a deeper ice-ocean interface is black.

2.2.4. Partial cell formulation

Bathymetry in an oceanic circulation model is commonly represented with a so-called 'step topography', where steps are fitted to the model grid. However, this approach is rather crude and only suitable for models with very high vertical resolutions. To increase representation accuracy of the ice-ocean interface and bathymetry, partial cell formulation based on Adcroft et al., 1997 is applied. Although Adcroft et al., 1997 describe two methods, only partial step is currently supported in MITgcm due to the storage requirement of shaved cells [Adcroft et al., 2008]. In contrast with ´step topography´, in this

approach model cells fit the topography. In practice, this results in model cells being only partly filled with ice or bed instead of fully.

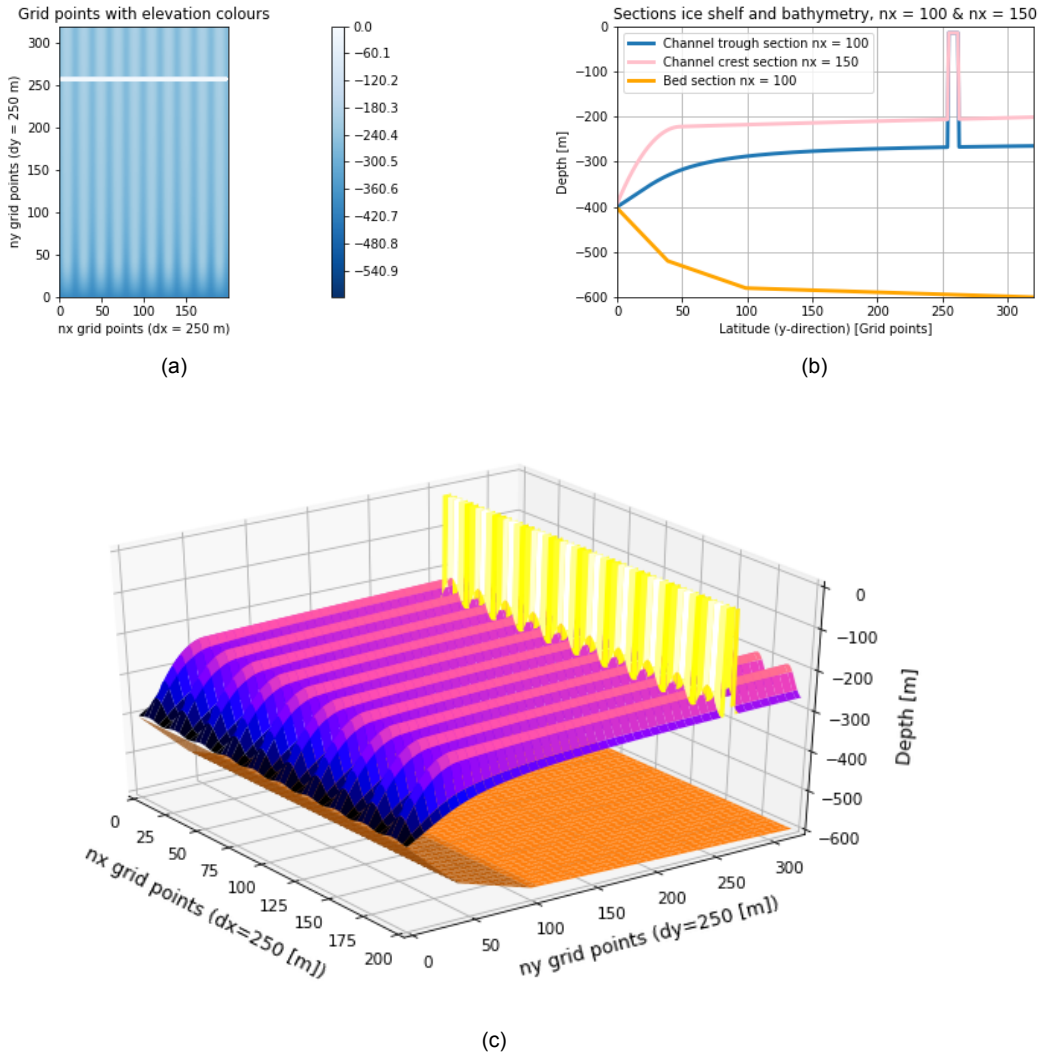

(a) (b)

(c)

Figure 2.3: The ice-ocean interface including 10 melt channels with a maximum depth of 100 [m] and a rift (at n_y[255:259]). Subfigure 2.3(a) shows the top view with the grid point elevation in colours. In 2.3(b), two along shelf sections can be observed. The section at n_x = 100 represents a channel trough and at n_x = 150 a crest. A full 3D visualization is shown in 2.3(c).

2.3. Initial & boundary conditions

To robustly reproduce cavity circulation, the model must be initialized and constrained with idealized oceanic profiles. Ocean temperature can influence basal melting (1.1.4). As this study focuses on cavity circulation, the open ocean can be neglected and replaced by a return flow at the ocean boundary of the domain. This is also beneficial as an open ocean is generally computationally heavy. To obtain the required initial and boundary conditions+ temperature, salinity, and horizontal velocity profiles are required. The profiles can be obtained by schematizing Antarctic temperature, salinity, and velocity field data from the available literature. This study uses Conductivity Temperature Depth (CTD) and Acoustic Doppler Current Profiler (ADCP) measurements taken near the Thwaites Ice Shelf [A. Wåhlin et al., 2021], the reasoning behind this choice is further explained in subsection 2.3.1. The initial conditions are assumed to be homogeneous in the horizontal plane (x,y). Furthermore, the boundary conditions are presumed to also vary in the vertical direction only. The derivation and inclusion of initial and boundary conditions are further discussed in subsections 2.3.2 and 2.3.3.

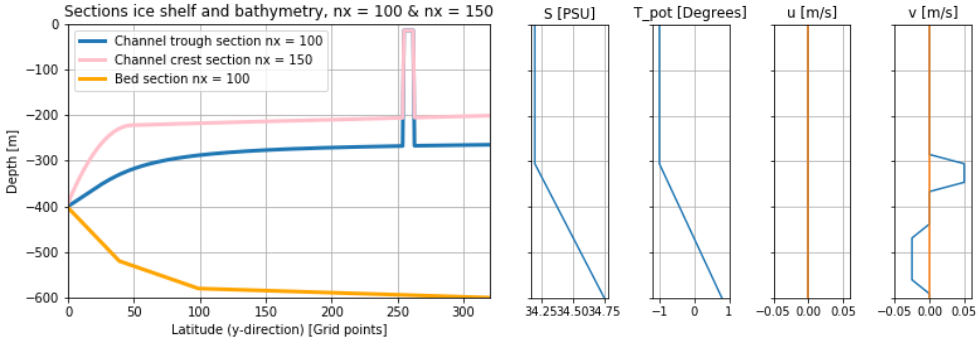

Figure 2.4: Along shelf section of the model, including ten melt channels and a rift, together with initial and boundary conditions. The first figure from the left shows two along shelf sections of the ice-ocean interface, where the channel crest (trough) is pink (blue). The bathymetry is orange. The other four figures show salinity, temperature, u and v profiles from left to right respectively. The dark orange lines in the last two plots indicate zero velocity. The salinity and potential temperature profiles are the same for initial and boundary conditions.

2.3.1. Reference data: Thwaites Ice Shelf

Whether Antarctic field data from literature can be used as a reference for the initial and boundary condition profiles in this model depends on the location and type of measurements. Temperature, salinity, and velocity should be measured at multiple points in the water column. The chosen location should be near or preferably beneath an ice shelf. The area must be in the proximity of melt channels, as mapped by Alley et al., 2016. It is preferable that the bathymetry beneath the ice shelf is deepening from the grounding line towards the ocean. Furthermore, it is advantageous if the width and depth of the cavity are comparable to the magnitudes used for the model domain.

While considering the requirements and preferences above, CTD and ADCP data sets obtained near the Thwaites Ice Shelf (5499 km^2 [Rignot et al., 2013]) between February and March 2019 [A. Wåhlin et al., 2021] are used in this study. Although values from inside the cavity would be preferable, accessing this region is difficult and dangerous [Dinniman et al., 2016]. Therefore, relevant data from an actual cavity in the proximity of melt channels is currently not available. The measurements by A. Wåhlin et al., 2021, made at an average 1.5 km distance from the ice shelf front, are used as the best alternative. The velocities obtained are of comparable magnitude with results from beneath the Larson C ice shelf by Davis and Nicholls, 2019. Furthermore, potential temperature and salinity are assumed to be carried into the cavity with the baroclinic flow [A. K. Wåhlin et al., 2020].

The study by A. Wåhlin et al., 2021 covers two troughs near the Thwaites Ice Shelf front (figure E1 in Appendix E), where T2 shows a clear in- and outflow in the along-shelf direction. Therefore, the measurements of this area are used to create the required ocean profiles. The size of the ice shelf is comparable to the one used in the model, together with the depth, deepening bathymetry towards the ocean boundary, and ice front thickness at T2. Lastly, it must be noted that the Thwaites Ice Shelf is situated in the Amundsen Sea, which has a relatively large influence of CDW and therefore warm and saline bottom values compared to locations on the East coast of Antarctica (1.1.3).

Since measurements by A. Wåhlin et al., 2021 will be used as a reference while determining the initial (2.3.2) and boundary conditions (2.3.3), the mean basal melt rate of the Thwaites Ice Shelf can be used for a model evaluation in Chapter 4.1. The mean basal melt rate of the Thwaites Ice Shelf is estimated at 17.7 ± 1.0 [m/year] in a modelling study by [Rignot et al., 2013].

2.3.2. Initial conditions

For an initial state that is homogeneous in the horizontal plane (x,y), the model requires a one-dimensional array [z] as input. Idealized potential temperature and salinity profiles are schematized from CTD data measured by A. Wåhlin et al., 2021. Figure 2.5 shows two along shelf sections of the model ice-ocean interface together with the bathymetry; and the profiles for salinity, temperature, cross shelf horizontal velocity, and along shelf horizontal velocity from left to right respectively. The derivations of the profiles are discussed below.

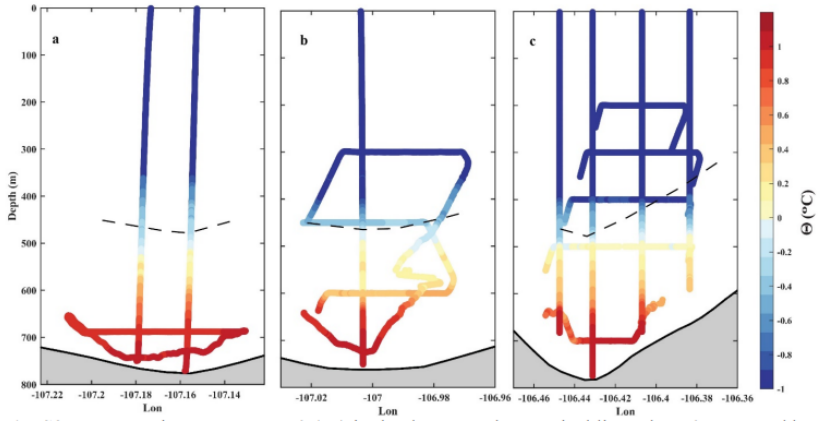

Figure 2.5: Potential temperature from CTD data measured in the deep troughs near the Thwaites Ice Shelf. Potential temperature is indicated with a colour spectrum where blue (red) represents cold (warm). The black dotted line shows the 300 meter elevation with respect to the seabed. Sub-figures a and b show the western and easter branch of trough T2 and c trough T3 (2.4).

The profile for potential temperature (figure 2.4, second profile from the left) is derived from the left sub-figure of 2.5, containing the potential temperature from CTD data measured near the Thwaites Ice Shelf. Blue (red) indicates cold (warm) water. Since the channel trough is a deeper than the bathymetry used in the model, the values are scaled to a depth of -600 [m] instead of -750 [m]. The potential temperature is assumed to be -1 [° C] in the surface layer till a depth of -300 [m], which is following the observations in figure 2.5. Furthermore, the temperature increases from -1 [° C] at -300 [m] to +0.8 [° C] at the seabed.

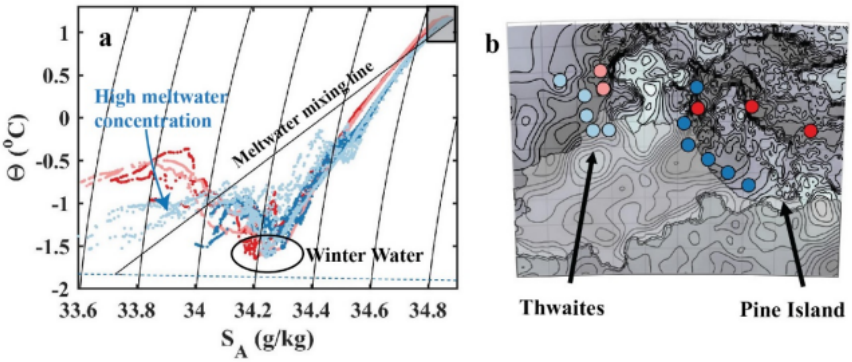

Figure 2.6: The first subfigure from the left shows the Historical S_A vs Θ CTD data from two basins, as given in A. Wåhlin et al., 2021. Information about the meltwater mixing line, winter water and high melt water concentration can be found in A. Wåhlin et al., 2021 and is not further used in this study. The second subfigure from the left gives locations where these salinity and potential temperature combinations were measured.

The salinity profile (figure 2.4, first profile from the left) is derived while using the assumed potential temperature values and figure 2.6 from A. Wåhlin et al., 2021. Figure 2.6 shows two subfigures, where

the left one gives the salinity against corresponding potential temperature and the right one the locations where the measurements were taken. The light blue and red colours indicate measurements around the Thwaites Ice Shelf. For $\Theta = -1$ [° C], S_A = 34.2 [PSU] and for $\Theta = +0.8$ [° C], S_A = 34.75 [PSU]. The shape of the salinity profile is assumed to be comparable to the potential temperature (see figure 2.4). The upper layer of the water column is mixed. From d = -300 [m] to the bed, the profiles increase linearly.

2.3.3. Boundary conditions

Temperature, salinity, and velocity matrices [x,z] are required to include boundary conditions in the model. The domain can be regarded as a box with six boundaries: four horizontal and two vertical boundaries. The vertical boundaries represent the top (d = 0 [m]) and bottom (d = -600 [m]) of the domain and will be closed off, referring to all boundary parameters being equal to zero, with the ice shelf and bathymetry respectively. In the horizontal direction, the model contains an ocean boundary (ny = 320 [-]), two sides (nx = 0 [-] & nx = 200 [-]) and a boundary at the grounding line (ny = 0 [-]). Since the model represents an ice shelf that is enclosed at the sides by topography, this study will only focus on transport that is perpendicularly flushing the cavity. Therefore, only the ocean boundary will be opened.

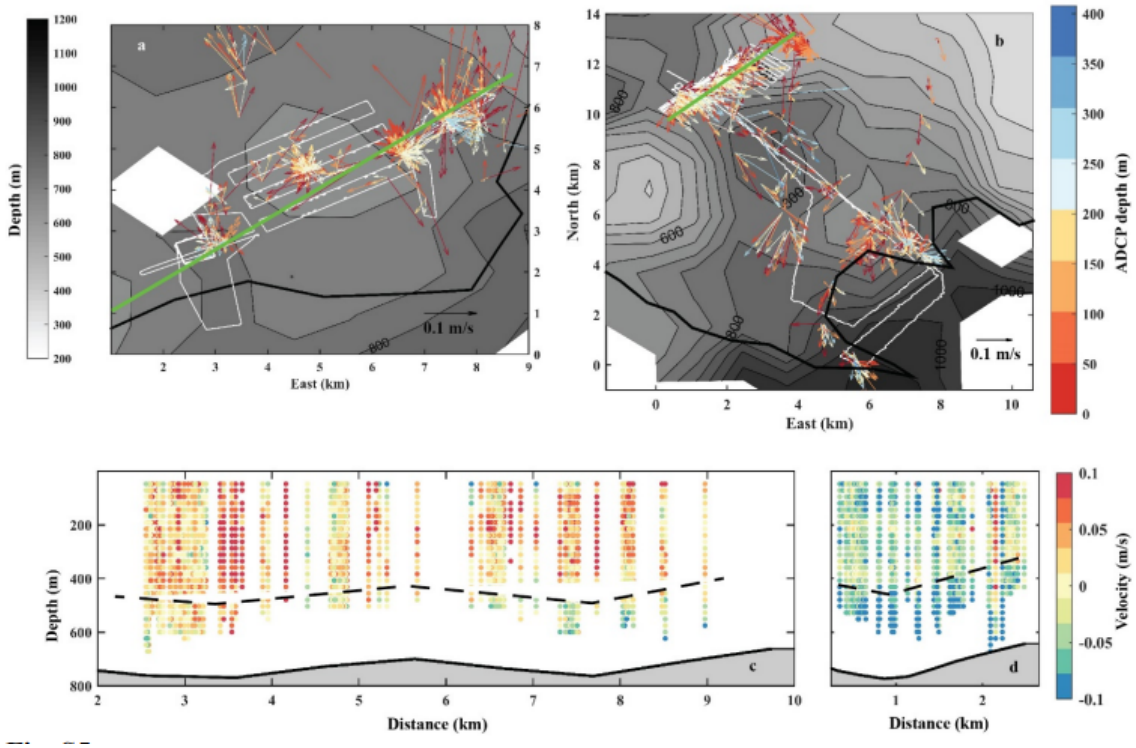

Figure 2.7: Velocity recordings using an ADCP. a-b: data averaged over 15 minutes and 96 m bins shown as arrows, colours corresponding to different depths. The thick black line is the ice front. The bathymetry is shown in grey, where a deeper part is darker. ADCP trajectories are given whit white lines. a: data in trough T2. b: data in trough T3. c: all along-channel components from within 500 meters of the green line in a. d: along-channel components from within 500 meters of the green line in b. The dashed black line represents the 300 m distance from the seabed [A. Wåhlin et al., 2021].

Open boundary

Four matrices [x,z] for the ocean boundary are given as model input. The salinity and potential temperature profiles are chosen equal to the initial conditions (figure 2.4) to keep model adjustment time and instabilities minimal. Cross shelf velocities u [m/s] (figure 2.4, second profile from the right) are assumed to be zero because only perpendicular transport is applied. The intrusion of CDW and HSSW from the open ocean into the cavity and the exit of ISW out of the cavity is reproduced by applying a return flow in along shelf direction on the ocean boundary of the domain. The along-shelf

velocities v [m/s] (figure 2.4, first profile from the left) are derived from ADCP data measured by A. Wåhlin et al., 2021, as can be found in figure 2.7. The lower left subfigure of 2.7 shows measurements around T2, where the flow changes direction around the black-striped line. Furthermore, the lower right figure contains data from T3. The upper two figures shows the corresponding ADCP trajectories in white and the measurment depths in a colour spectrum from red (shallow) to blue (deep). This study used data from T2, the lower left figure. Here, the velocity direction in along shelf direction is visualized at different depths with a colour spectrum from blue (towards the shelf) to red (from the shelf). Since more data is available from the upper part of the water column, an average estimate of these measurements is used as a starting point for the outflow magnitude. Furthermore, the ratio of in and outflow areas is applied to the ocean boundary as well. From figure 2.7 it is assumed that the area of inflow is approximately two times as small as the area of outflow. Since mass should be conserved in the model and only the ocean boundary will open, the same amount of water should go out and into the domain. Since the in- and outflow areas differ, the velocities must be scaled to keep the volumes the same. Furthermore, an area of zero velocity and transition points are applied to prevent model instability by creating large velocity gradients. The resulting shape can be observed in the first profile on the left from figure 2.4.

Inflow at the bottom of the domain represents the warm and saline intrusion, whereas outflow near the ice shelf depicts the fresh meltwater plume. Since all the other boundaries are closed, the mass should be conserved by equalizing the inflow to the outflow magnitude at the ocean boundary. The balancing option of the OBCS package is used to correct for small deviations that could occur. Furthermore, an area of zero velocity is placed in between to ensure model stability and keep the in- and outflow from mixing. A so-called 'sponge layer' is applied at grid points ny[310:319], which damps the effect of the enforced boundary conditions on the model [Adcroft et al., 2008].

Closed boundaries
To solve the HPE, kinematic boundary conditions are needed at the vertical and horizontal closed boundaries. The vertical kinematic boundary conditions are imposed at the bottom and surface [Adcroft et al., 2008]:

$$\text{bottom: } w = 0 \text{ at } z = z_{bottom} \tag{I.2.3.32}$$

$$\text{surface: } w = 0 \text{ at } z = z_{surface} \tag{I.2.3.33}$$

The horizontal kinematic boundary condition states that at every horizontal closed boundary there should occur no normal flow:

$$\vec{\mathbf{v}} * \hat{n} = 0 \text{ with } \hat{n} \text{ the unit vector in the normal horizontal direction} \tag{I.2.3.34}$$

2.4. Temporal resolution

The model requires an end time T_{end} [s] and time step Δt [s]. The applied time step (2.4.1) and obtained quasi-steady state after five years of numerical time (2.4.2) are discussed below. Furthermore, a three-monthly mean (2.4.3) is computed in addition to the five years to acquire diagnostics.

2.4.1. Time step

To ensure model stability for the advection scheme used (2.1.8), the Courant number should be smaller than 0.3 [Adcroft et al., 2008]. The expression for the Courant number is equal to [Zijlema, 2021]:

$$C = \frac{|u_{x,y,z}|\Delta t}{\Delta L_{x,y,z}} \tag{I.2.4.35}$$

With velocity $u_{x,y,z}$ [m/s], time step Δt [s] and spatial resolution $\Delta L_{x,y,z}$ [m]. For a three-dimensional model, the condition should be satisfied in the vertical and two horizontal directions. The time step is

limited by the vertical resolution since it is an order of magnitude smaller than the horizontal. Taking the above-mentioned into consideration, a time step equal to 60 [s] is chosen.

2.4.2. Quasi-steady state

A quasi-steady state must be reached to ensure the influence of the initial state on the solution vanishes [Zijlema, 2021]. The mean salinity of the model domain is used as an indicator for quasi-steady state after a certain numerical time since the diagnostic is only influenced by the in- and outflow together with the freshwater flux. The salinity at a moment in time should not deviate more than 1 % from its mean value over a certain period. The period used in this study to determine whether quasi-steady state occurs is one year, 365 days. The monitoring frequency used is one day.

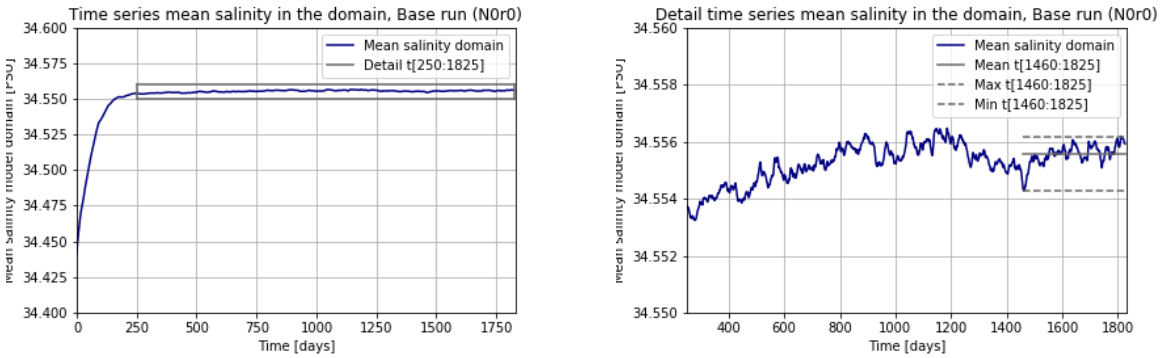

(a) (b)

Figure 2.8: (a) Monitoring time in days against mean salinity of the domain. (b) Detail of figure (a) from day 250 until day 1825.

Whether the model is in quasi-steady state is determined in Appendix F, by observing salinity time series for all model runs (2.6). An example of this determination is shown in figure 2.8, representing the base run (as described in 2.6). Subfigure 2.8(a) shows the monitoring time in days on the x-axis against the mean salinity of the domain. The spin-up time can be observed up until day 250. The period after day 250 is indicated with a grey box and shown in subfigure 2.8(b). Quasi-steady state is assumed to occur after five years of numerical time, T_{end} = 1825 [days], when the time series shows little deviation from the mean values of one year. The min, max and mean value of this period are indicated with the grey lines in subfigure 2.8(b). The last year is thus defined from day 1460 until day 1825, where the relative difference between the maximum value and the mean is 0.0018 %. The relative difference between the minimum value and the mean is 0.0037 %. Both dissimilarities are smaller than the earlier mentioned limit of 1 %. The computational required to calculate until day 1825 is equal to 6,5 days.

2.4.3. Three-monthly mean

As a default, MITgcm returns only snapshots of model parameters. Mean values can be obtained by using the diagnostic package (2.1.7). However, this package is computationally heavy. To minimize computational time, diagnostics are only calculated after the model is in quasi-steady state. In addition to the initial five years, the model is assigned another three months of numerical calculation to determine a three-monthly mean of the required diagnostics (2.5).

2.5. Diagnostics

While using the diagnostics package (2.1.7) the model returns the parameters, required for this study, discussed in subsection 2.5.1. The area definitions used in the result (3.1, 3.2 & 3.3) and discussion (4) chapters are shown in subsection 2.5.2.

2.5.1. Parameters

The model returns the oceanic freshwater flux, horizontal velocities, salinity, and temperature. The definitions of the diagnostics in this study are explained below. The oceanic freshwater flux is computed

at the boundary layer while the velocities, temperature, and salinity at the first grid point beneath the ice-ocean interface are used.

Freshwater flux
The ice shelf freshwater flux, the melting or freezing rate for every grid point at the ice-ocean interface, is obtained by using the oceanic freshwater flux q_{ocean} $[kg/m^2s]$ (subsection 2.1.7 & 2.1.6) returned by the model. The ice oceanic freshwater flux is related to the ice shelf freshwater flux q_i as:

$$q_i = -q_{ocean} \tag{I.2.5.36}$$

where a negative (positive) q_i represents freezing (melting). The freshwater flux at the ice-ocean interface referred to in this study is expressed in [m/year] by:

$$q_i = -q_{ocean} * (\frac{1}{\rho}) * (3600 * 24 * 365) \tag{I.2.5.37}$$

With ρ= 1000 $[kg/m^3]$.

Horizontal velocities
The horizontal velocities u and v [m/s] are solved with the Hydrostatic Primary Equations from subsection 2.1.1 and 2.1.2. Parameter u is the cross shelf velocity and v is the along shelf velocity. This study only considers the velocities in the first grid points beneath the ice-ocean interface (2.5.2).

Temperature and salinity
The temperature and salinity are determined from the equations in subsection 2.1.5. The flux term $F_{T,S}$ is computed with equation I.2.1.22 from 2.1.6. Only the values in the first grid points beneath the ice-ocean interface are considered (2.5.2).

2.5.2. Area definitions

Three different areas are regarded in result sections 3.1, 3.2 & 3.3: the total basal ice shelf area, the area inside the rift, and the area inside and in the proximity of the rift.

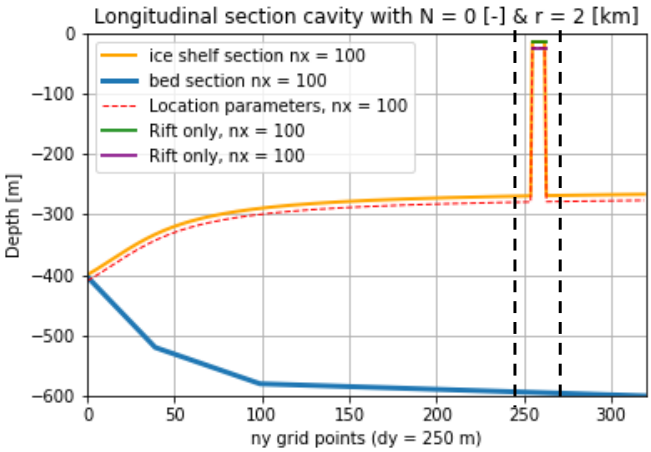

Figure 2.9: An along shelf section of the parameter areas, as used in Chapter 3.1, 3.2 & 3.3. The freshwater flux is computed on the ice-ocean interface. For this diagnostic, the total basal area is shown in orange and green together, and the rift area in green. Velocities, temperature, and salinity are determined one grid point from the ice-ocean interface. For these diagnostics, the total basal area is defined in red and purple and the rift alone in purple. The area inside and in the proximity of the rift as used in subsection 3.2.2 is enclosed by the black dotted lines. The model bathymetry is given in blue.

The top of the rift area (used in subsection 3.2.2 & section 3.3) is enclosed by along shelf grid points 255 till 262 [63.75 - 65.50 km]. To exclude the closed boundaries at the sides, it covers the total cross

shelf width from grid point 1 to 298. When the proximity of the rift is included (in subsection 3.2.2), the along shelf area is enclosed by grid points 251 and 266 [62.75 - 66.75 km] instead. The total basal ice shelf area (used in subsection 3.1 & section 3.2.1) is represented by the complete ice-ocean interface of the domain, including the rift. The three different areas are shown in figure 2.9, where an along shelf section of the ice-ocean interface is indicated with orange and the bathymetry with blue. The total basal ice shelf area is visualized with orange and green or with red and purple, for the gridpoints at and one beneath the ice shelf base respectively. The area inside the rift is shown in green and purple only. The area in proximity of the rift is enclosed with black dotted lines.

2.6. Runs

To investigate the effect of basal channels on a rifted Antarctic ice shelf, sensitivity runs are performed where only the ice-ocean interface (2.2.3) is altered. Results from the four runs will be compared. The runs contain an ice shelf without a rift and basal channels, an ice shelf with only a rift, an ice shelf without a rift and with basal channels, and an ice shelf with a rift and basal channels. The runs are shown in the table below, where $N_a r_b$ represents the inclusion or exclusion of basal channels and a rift. Here 'a' is the number of channels and 'b' is the rift width. Therefore, $N_0 r_0$ is the control run.

Furthermore, the channel number used is equal to 10, and the maximum crest depth $d_{crest,max}$ = 100 [m]. Since the width of the domain is fixed, the size $\Delta x_{channel,max}$ depends on the channel number and is equal to 5 [km] for 10 channels. These assumptions are based on observed general melt channel sizes [Alley et al., 2016]. The rift width y_{rift} is equal to an average value of 2 km [Poinelli, 2022].

Run	Name	Reference	$N_{channel}$	$\Delta x_{channel,max}$ [km]	$d_{c,max}$ [m]	Δy_{rift} [km]
1	Base run	$N_0 r_0$	0	0	0	0
2	Rift	$N_0 r_2$	0	0	0	2
3	Channels	$N_{10} r_0$	10	5	100	0
4	Channels & rift	$N_{10} r_2$	10	5	100	2

3

Results

The model results are divided into three sections. The mean basal melt and freezing rate of the four runs are shown in section 3.1. In section 3.2, the melting/freezing and horizontal flow pattern are visualised. Horizontal velocities, salinity, and temperature are used in an offline calculation of the three-equation model in section 3.3.

3.1. Mean basal melting and freezing rates

The mean basal melt rates, the averages of all the ice shelf freshwater fluxes as defined in 2.5 for one run, are computed to determine whether the presence of basal channels results in a decrease (subsection 3.1.1). The difference in freshwater flux between run $N_{10}r_2$, with channels and a rift, and the base run N_0r_0 is resolved. This value can be compared to the deviations between N_0r_2 and $N_{10}r_0$ with the base run, to determine whether the simultaneous occurrence of basal channels and a rift results in an additional melt decrease. The mean freezing rates, where only the negative freshwater fluxes are considered, are shown in subsection 3.1.2 to visualize whether channels and rifts influence freezing in the domain. The key findings of this section are summarized in subsection 3.1.3.

3.1.1. Annual mean freshwater flux

Figure 3.1 shows the average q_i , melting and freezing rates on the ice-ocean interface, of the domain. The sensitivity runs are shown on the x-axis and the annual basal melting [m/year] on the y-axis.

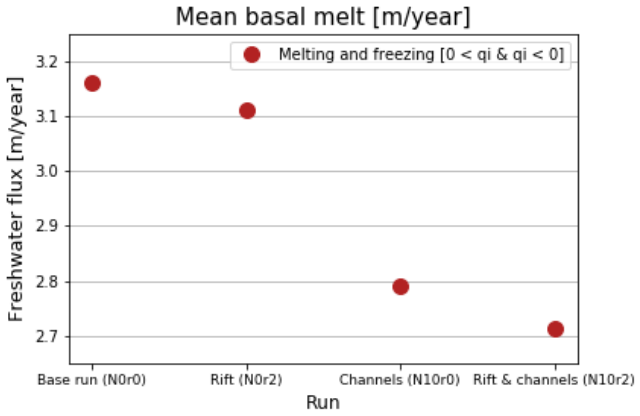

Figure 3.1: The four runs mentioned in section 2.6 against the resulting freshwater flux [m/year], the average of all the ice-ocean boundary melting and freezing rates.

One can observe that base run N_0r_0 shows the highest positive freshwater flux q_i, which indicates melting: 3.16 [m/year]. Run $N_{10}r_2$, including basal channels and a rift, gives the lowest melt rate: 2.71 [m/year]. The rates for run N_0r_2 and $N_{10}r_0$ are 3.11 [m/year] and 2.79 [m/year] respectively. Adding a rift therefore results in a melt reduction of ((3.16-3.11)/3.16) * 100 = -1.59 %. The introduction of only channels gives a decrease of -11.7 %. Channels and a rift combined reduce the melting by -14.2 %. Therefore, the following can be stated:

$$(N0r0–N10r2) > (N0r0 - N0r2) + (N0r0 - N10r0) \tag{I.3.1.1}$$

$$0.45 > 0.42 \tag{I.3.1.2}$$

Run $N_{10}r_2$ shows an additional ~ 7% melt reduction when compared to the combined decrease of N_0r_2 and $N_{10}r_0$ with respect to base run N_0r_0. Furthermore, the addition of channels seems to have a larger impact on melt reduction (-11.7 %) than the addition of a rift (-1.59 %).

3.1.2. Mean freezing rate

The average freezing rates are shown in figure 3.1. The sensitivity runs are shown on the x-axis and the freezing rate (mean of all negative annual freshwater fluxes q_i [m/year]) on the y-axis. The runs without a rift (N_0r_0 & $N_{10}r_0$) give negligible (10^{-3}) mean freezing in the domain. The average freezing is highest in the run with channels and a rift ($N_{10}r_2$): -0.5374 [m/year]. A lower annual rate is found in the run with only a rift (N_0r_2): -0.4388 [m/year]. Therefore, freezing increases with -0.5374/-0.4388 = 1.2247 ~ 22.47 %, when one compares $N_{10}r_2$ to N_0r_2.

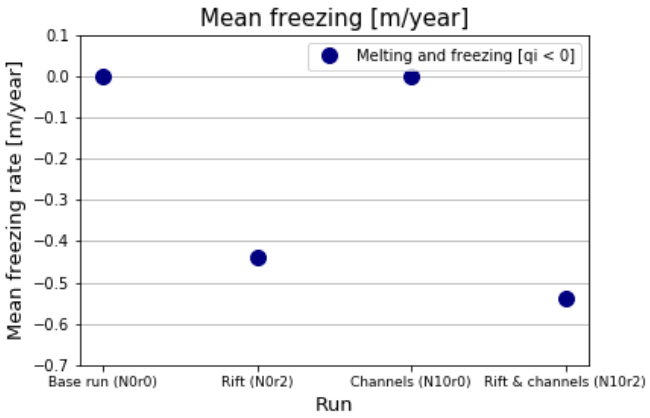

Figure 3.2: Mean freezing rates [m/year] for the four runs as introduced in section 2.6. These rates are calculated as the average of all negative melt rates on the ice-ocean boundary.

3.1.3. Summary mean melting/freezing results

The highest mean annual melt rate, a positive freshwater flux q_i, occurs in the base run (N_0r_0), where the lowest can be found in the run containing melt channels and a rift ($N_{10}r_2$). The runs with only channels or a rift show intermediate decrease, but the effect of channels seems to be about seven times as high. The melt reduction of $N_{10}r_2$ with respect to the base run is % 7 larger than the sum of the lessening of N_0r_2 and $N_{10}r_0$. Furthermore, freezing is negligible in the runs without a rift (N_0r_0 & $N_{10}r_0$). When compared to N_0r_2, the annual mean freezing rate increases with 22.47 % in $N_{10}r_2$.

3.2. Melting/freezing & horizontal flow pattern

The melting/freezing at the ice-ocean interface is visualized in this section, together with the velocity magnitude. The velocity magnitude is related to melting/freezing intensity (2.1.6). First, the melting/freezing and flow patterns of the ice shelf basal surface, as defined in 2.5.2, are regarded for the four runs (subsection 3.2.1). The melt and flow pattern observations from 3.2.1 can be compared to existing knowledge about rifts and basal channels influencing an ice shelf (4.1.2). Section 3.1 shows that, in this study, freezing only occurs inside the rift. Subsection 3.2.2 therefore focuses separately on horizontal velocities inside and in the proximity of the through-surface fractures of run N_0r_2 & $N_{10}r_2$ (as defined in 2.5.2), together with the freezing patterns inside the rifts. A summary of the main observations is given in subsection 3.2.3.

3.2.1. Ice shelf basal surface

This subsection contains observations from figures 3.3, 3.4, 3.5, and 3.6. The horizontal velocity (u,v) is regarded, together with the melt/freeze pattern at every fifth grid point. The x-axis shows the cross shelf direction and the y-axis the along shelf direction. Therefore, the figures represent the horizontal velocity and ice shelf freshwater flux q_i pattern in the horizontal plane along the ice shelf base, where the bottom refers to the grounding line side and the top to the ocean side of the domain. The rift area will be discussed in detail in subsection 3.2.2. The horizontal velocity pattern is given in vectors, of which the size relates to the magnitude. The melting/freezing intensity is visualized with a colour bar, where blue represents freezing and red melting. The darker the colour, the higher the intensity. When channels are present, the locations of the troughs are indicated in green.

Horizontal velocity pattern ice shelf

Figures 3.3 & 3.4 show that without channels (N_0r_0 & N_0r_2) the flow pattern (u,v) in the boundary layer has the shape of a boundary current: the ice shelf melts at the grounding line and rises due to buoyancy while it deflects towards the left under the influence of the Coriolis force. Figures 3.5 & 3.6 show that when channels are present ($N_{10}r_0$ & $N_{10}r_2$), the boundary current flow pattern changes to a return flow in each channel. The flow vectors are small at the channel crests but large at the channel keels and sides. Large velocity vectors near the grounding line are observed in all cases.

Freshwater flux pattern

Figures 3.3, 3.4, 3.5, and 3.6 show that strong melting appears when large velocity vectors are present. The strongest melting appears near the grounding line of the domain, where the ice shelf is situated in deeper and warmer water. The strongest melting in the base run occurs on the Coriolis favoured side of the domain. The melt pattern of run N_0r_2 is comparable to that of base run N_0r_0, but with the addition of a freezing area in the rift further discussed in subsection 3.2.2. Melting in the area after the ocean side of the rift increases. In $N_{10}r_0$, the boundary current observed in the base run is replaced with melting along the flanks and keels of the channels. Little melt occurs in the channel crests, but the strong melting area at the flanks and keels reaches further towards the ocean boundary when compared to the base run. The pattern in $N_{10}r_2$ is comparable to that of $N_{10}r_0$, with the addition of a freezing area in the rift. The freezing area will be further discussed in section 3.2.2.

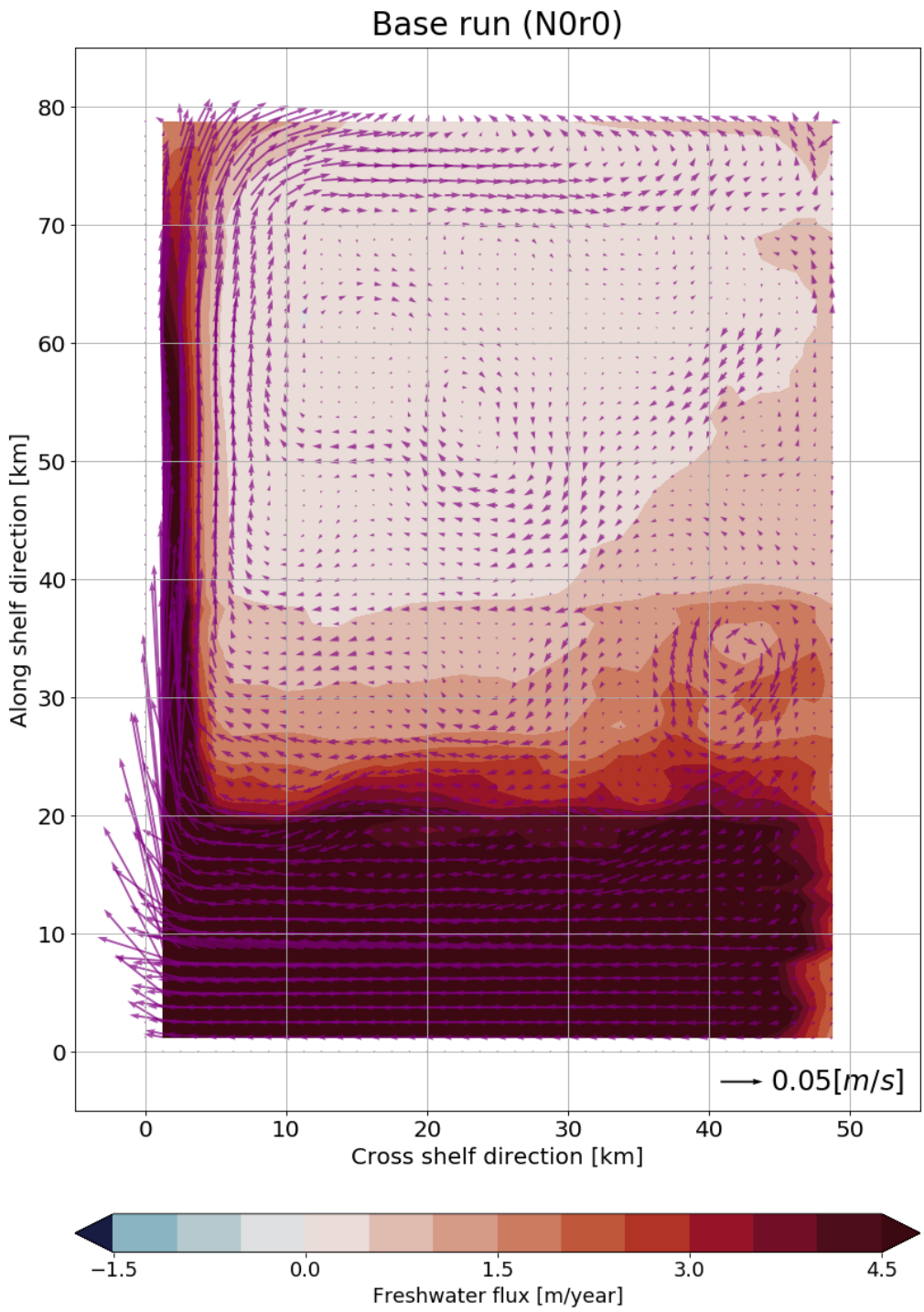

Figure 3.3: A contour plot of the ice shelf freshwater flux in the boundary layer for base run N_0r_0, together with the horizontal velocity vector pattern at the first grid point beneath the ice-ocean interface (2.5.2). To obtain a proper visualisation, only every fifth value of the diagnostics is shown.

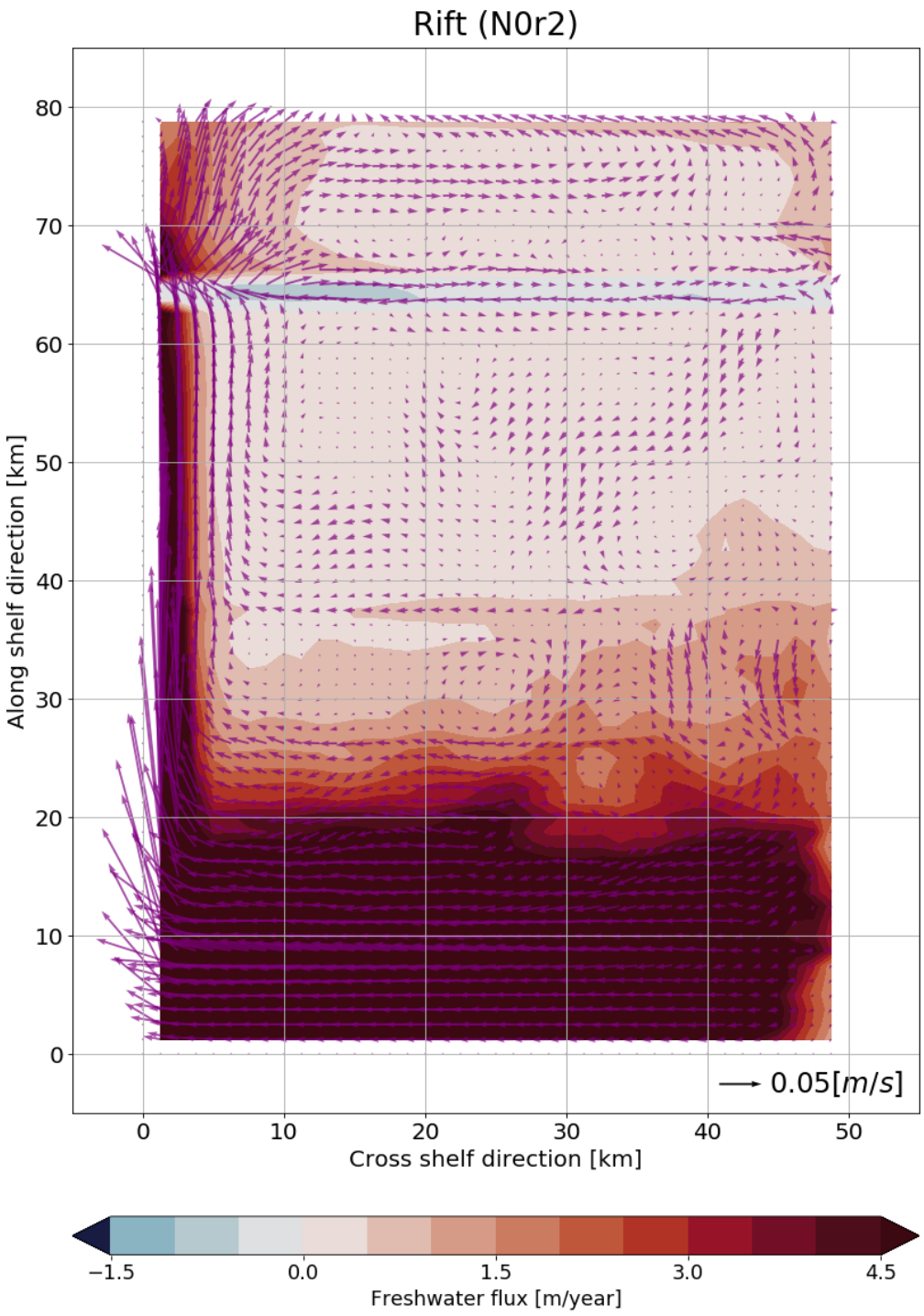

Figure 3.4: A contour plot of the ice shelf freshwater flux in the boundary layer for run N_0r_2, together with the horizontal velocity vector pattern at the first grid point beneath the ice-ocean interface (2.5.2). To obtain a proper visualisation, only every fifth value of the diagnostics is shown.

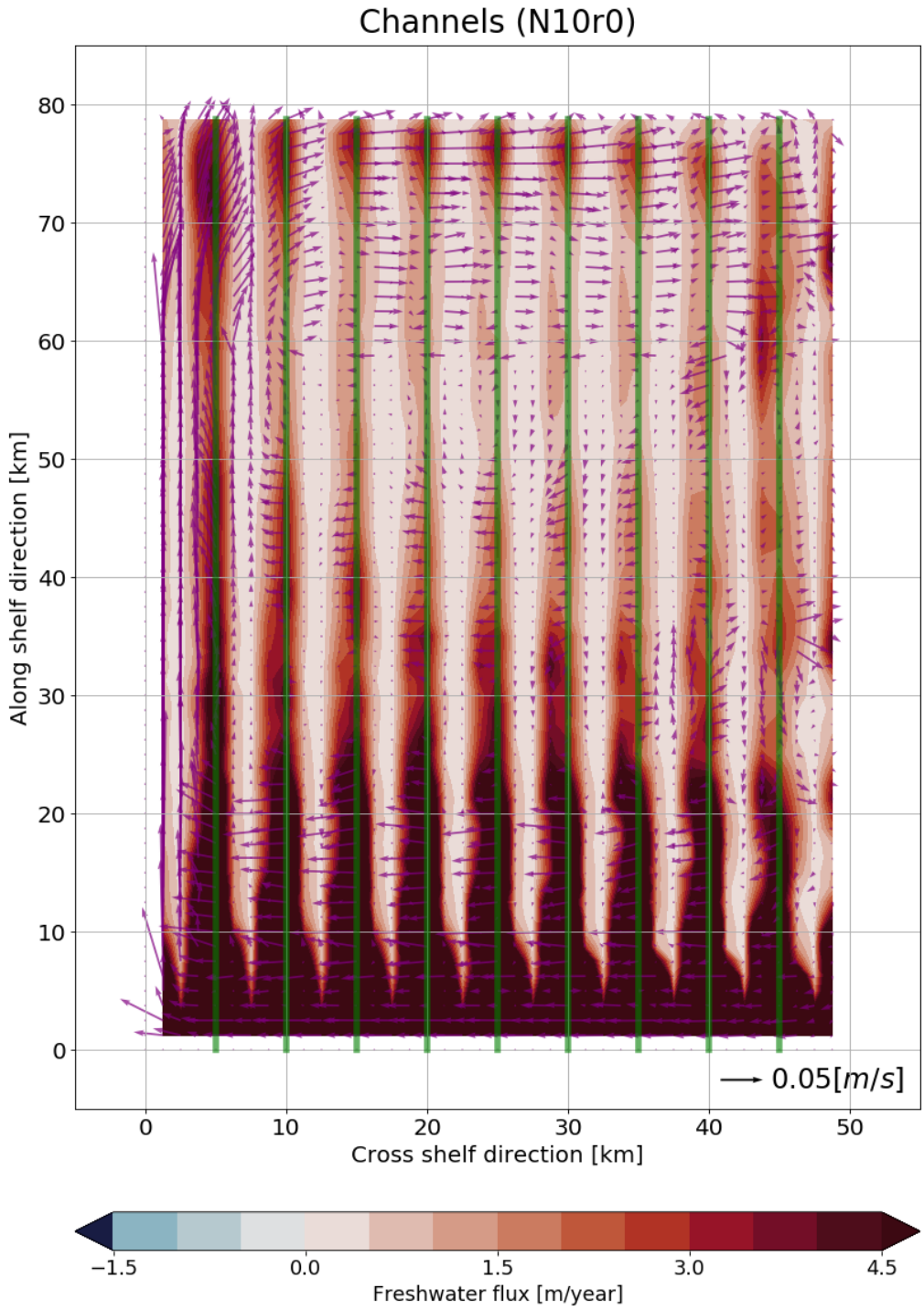

Figure 3.5: A contour plot of the ice shelf freshwater flux in the boundary layer for run $N_{10}r_0$, together with the horizontal velocity vector pattern at the first grid point beneath the ice-ocean interface (2.5.2). To obtain a proper visualisation, only every fifth value of the diagnostics is shown. The locations of the channel troughs are indicated with green lines.

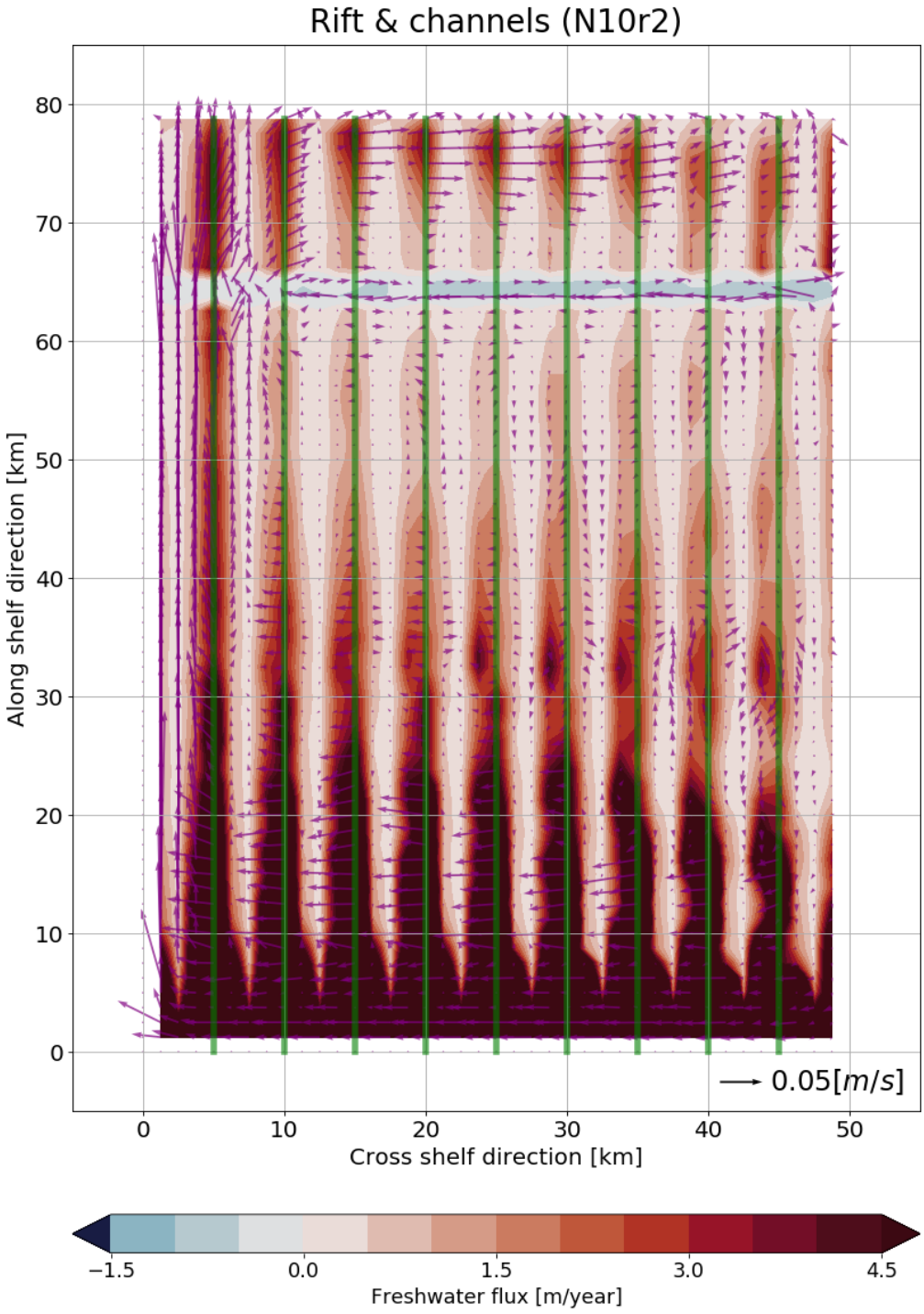

Figure 3.6: A contour plot of the ice shelf freshwater flux in the boundary layer for run $N_{10}r_2$, together with the horizontal velocity vector pattern at the first grid point beneath the ice-ocean interface (2.5.2). To obtain a proper visualisation, only every fifth value of the diagnostics is shown. The locations of the channel troughs are indicated with green lines.

3.2.2. Inside and in the proximity of the rift

The following subsection will further focus on runs including a rift: $N_{10}r_2$ and N_0r_2. Detailed circulation patterns at one grid point beneath the ice shelf base are given in figures 3.7 (N_0r_2) and 3.8 ($N_{10}r_2$). Due to the difference in observed along and cross shelf length, the area is divided into segments of 10 [km] along the x-axis. The top segment is the area that starts at zero [km] in cross shelf direction. The x-axis shows the full cross shelf direction and the y-axis the along shelf direction . The figures represent the horizontal velocity and ice shelf freshwater flux pattern in the horizontal plane along the ice shelf base inside and in the proximity of the rift at every fifth grid point. The horizontal velocity pattern is shown in vectors, of which the size again relates to the magnitude. The melting/freezing intensity is visualized with a colour bar, where blue indicates freezing and red melting. A darker the colour represents higher intensity. When channels are present, the locations of the troughs are indicated in green. The patterns inside and in the proximity of the rift are discussed. The latter indicates where buoyant plume water enters the rift. Furthermore, the freezing inside the rift is examined.

Horizontal velocity pattern inside and in the proximity of the rift

One large return flow can be observed inside the rift visualized in 3.7 (N_0r_2). The direction of the circulation is clockwise. Figure 3.8 ($N_{10}r_2$) on the other hand indicates multiple small clockwise return flows after every channel. The velocity patterns in both figures suggest that the buoyant plume rises on the grounding line side of the rift as it deflects to the left under the influence of the Coriolis force. The water sinks at the ocean boundary of the domain, where it again deflects to the left. This flow pattern results in the clockwise motion observed in both runs. From figure 3.7 (N_0r_2) it can be determined that the velocity vectors are parallel to the rift everywhere except in the boundary current. Buoyant plume water possibly enters the rift around this location. At the grounding line edge of the rift, figure 3.8 ($N_{10}r_2$) shows a strong inflow at the Coriolis favoured side of each channel. A weaker inflow can be observed at the Coriolis favoured side of the channels at the ocean flank of the rift.

Freezing rate inside rift

Following observations in 3.2, figures 3.7 (N_0r_2) and 3.8 ($N_{10}r_2$) show relatively strong freezing rates where large velocity vectors are present. When figures 3.7 & 3.8 are compared, only more freezing occurs in N_0r_2 for the first two 10 kilometres in cross shelf direction. Furthermore, freezing appears to be comparable from 10-20 kilometres. Run $N_{10}r_2$ indicates more freezing from 20-50 kilometres. In figure 3.8, most freezing arises just after the Coriolis favoured flank of the channels at the grounding line side of the rift. Figure 3.7 shows the highest freezing rates just after the boundary current described in 3.2.1.

3.2.3. Summary freshwater flux and flow pattern results

High melting and freezing rate intensities coincide with strong horizontal velocity vector strength. Melting is strong in all runs at the grounding line, where the ice shelf is situated in a deeper and warmer part of the water column. Additionally, runs without channels (N_0r_0 & N_0r_2) show strong melting in the form of a boundary current on the Coriolis favoured side of the domain. Instead of in a boundary current, strong melting in runs with channels ($N_{10}r_0$ & $N_{10}r_2$) can be observed at the flanks and keels of the ice shelf topography. Little melting occurs in the channel crest, this results in a reduction in mean melt near the grounding line.

In this study, freezing only appears in the rift and therefore exclusively in runs N_0r_2 & $N_{10}r_2$. In both runs, a clockwise circulation can be observed, driven by buoyant meltwater mainly entering the rift at the grounding line side and leaving at the ocean side. Without channels (N_0r_2), the velocity pattern in the rift shows that meltwater enters the rift in the boundary current. However, when channels are present the single clockwise return flow in the rift changes to multiple small clockwise return flows after every channel. After every channel inflow occurs, instead of only at the boundary current. Inflow then also appears at the ocean side of the rift, although still in a generally smaller magnitude when compared to the grounding line side. When the freezing pattern inside the rifts of N_0r_2 and $N_{10}r_2$ are compared, N_0r_2 shows only higher values at and next to the boundary current. For the rest of the rift area, $N_{10}r_2$ returns a higher freezing rate.

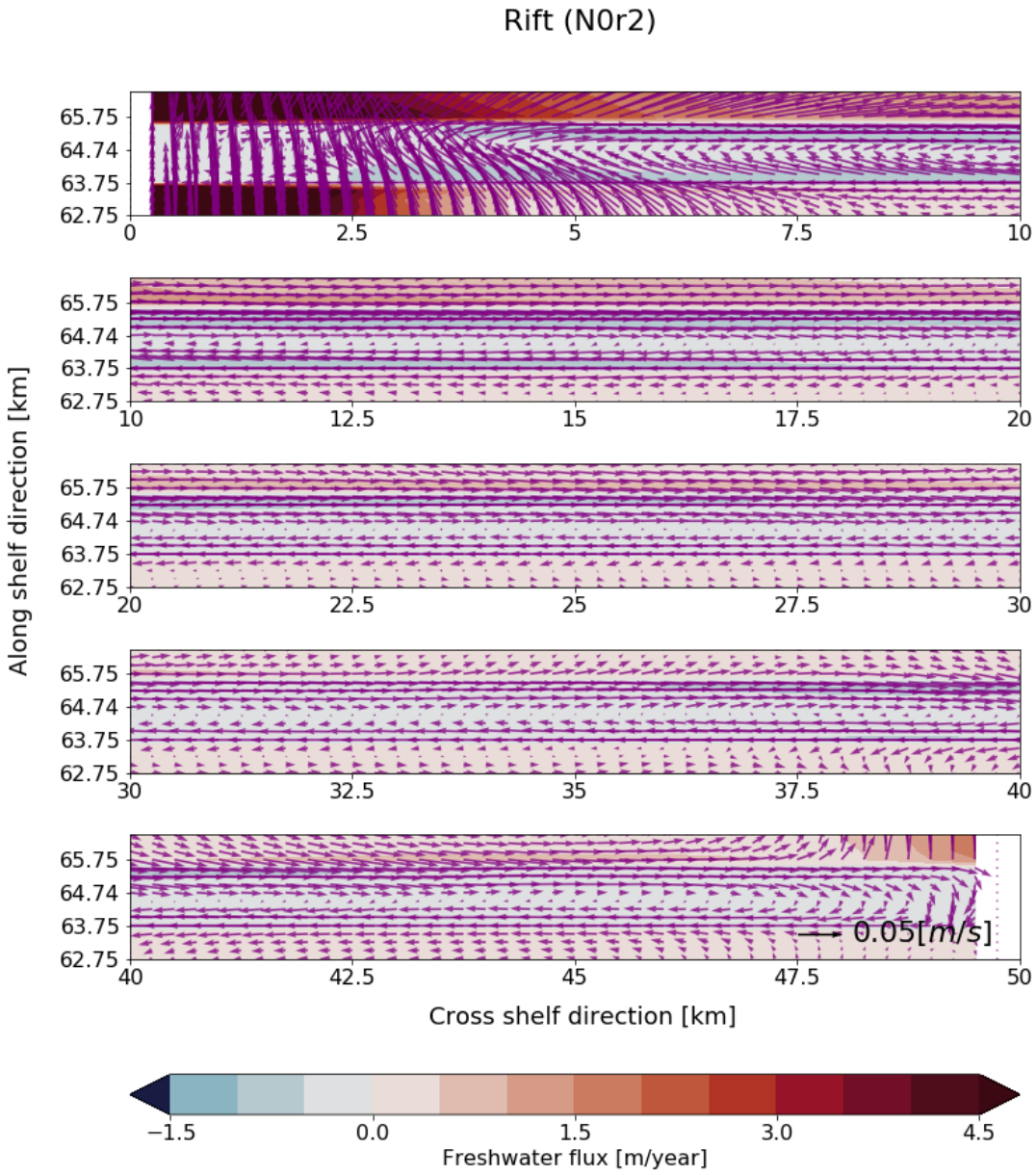

Figure 3.7: A detail of contour plot 3.4 containing the ice shelf freshwater flux in the boundary layer for run N_0r_2, together with the horizontal velocity vector pattern at the first grid point beneath the ice-ocean interface (2.5.2). In contrast with figure 3.4, all the diagnostics values are shown.

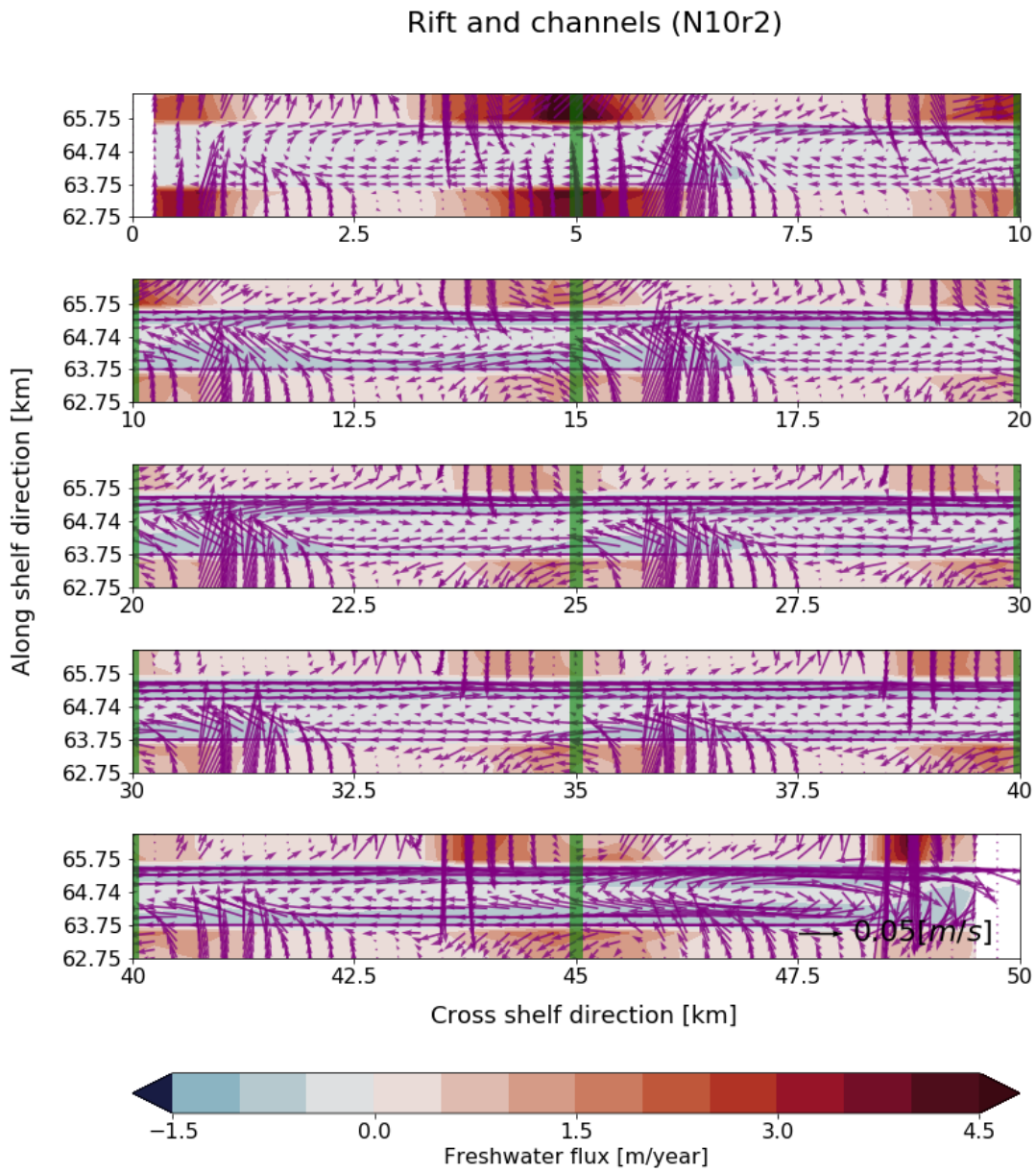

Figure 3.8: A detail of contour plot 3.6 containing the ice shelf freshwater flux in the boundary layer for run $N_{10}r_2$, together with the horizontal velocity vector pattern at the first grid point beneath the ice-ocean interface (2.5.2). In contrast with figure 3.6, all the diagnostics values are shown. The locations of the channel troughs are indicated with green lines.

3.3. Influence channels on freezing rate inside the rift

Subsection 3.1 and 3.2 show dissimilarity in freezing rate inside the rift between run N_0r_2 & $N_{10}r_2$. The goal of this section is therefore to gain insight into the possible processes altering the freezing rate in the rift. To determine the factors and their relative contribution, the three-equation model from 2.1.6 is considered. As the separate components of the three-equation model are not given as model output, the freezing rate for each grid point in the first layer beneath the top of the ice-ocean interface inside the rift is calculated (subsection 3.3.1) for $N_{10}r_2$ & N_0r_2. The three-monthly mean diagnostics for temperature, salinity, and horizontal velocity (u,v) are used.

Sub-subsection 3.3.1 shows that the contribution of the heat conduction term in equation I.2.1.19 is negligible. The freezing rate is then expressed as the product of multiple constant coefficients (c_p [J/kg/K], ρ_c [kg/m^3], $\frac{1}{L}$ [J/kg]), the heat transfer coefficient γ_T [m/s], and the thermal forcing (T-T_f) [ΔK]. Therefore, the increase between runs $N_{10}r_2$ & N_0r_2 is related to deviations of the two varying parameters between runs. The contribution of the two factors is approximated in subsection 3.3.2. A summary of the results is given in subsection 3.3.3.

3.3.1. Three-equation freezing rate calculation

The three-equation model as presented in subsection 2.1.6 is used to calculate the freezing rate q_i [m/s] for every first grid point beneath the ice shelf base at the top of the rift. The calculation requires four input values for every grid point: in-situ temperature T [° C], in-situ salinity S [PSU], horizontal velocity component u [m/s], and horizontal velocity component v [m/s]. The three-monthly mean diagnostics returned by the model, as described in 2.5, are used. First, the heat transfer coefficient is calculated, followed by the thermal forcing. The thermal forcing and heat transfer coefficient are used to obtain the freezing rate. Lastly, the contribution of the diffusive flux term in the three-equation model is discussed.

Heat transfer coefficient

To determine the heat transfer coefficient γ_T for each grid point, the frictional velocities u_* must first be determined with equation I.2.1.26:

$$u_*^2 = 0.0021 * \left(u^2 + v^2\right) \tag{I.3.3.3}$$

The three-monthly mean horizontal velocity component u [m/s] and horizontal velocity component v [m/s] are used for each grid point. The frictional velocity is then substituted into equation I.2.1.24, together with the constant values described in subsection 2.1.6:

$$\Gamma_{Turb} = \frac{1}{0.4} \ln\left(\frac{u_*^2 * 0.052 * 1^2}{(1.4 * 10^{-4}) * 5 * (1.95 * 10^{-6})}\right) + \frac{1}{2 * 0.052 * 1} - \frac{1}{0.4} \tag{I.3.3.4}$$

Furthermore, equation I.2.1.25 gives:

$$\Gamma^T_{\text{Mole}} = 12.5 * (13.8)^{2/3} - 6 \approx 65.9 \tag{I.3.3.5}$$

Expressions I.3.3.3, I.3.3.4, and I.3.3.5 are substituted into I.2.1.23 to obtain the heat transfer coefficient for each grid point.

Furthermore, relation I.2.1.27 is applicable when Γ^T_{Mole} is large compared to Γ_{Turb}. The mean values for Γ_{Turb} are approximately 17.15 [-] and 16.95 [-], for $N_{10}r_2$ and N_0r_2 respectively. When compared to the magnitude of I.3.3.5, one can assume that the heat transfer coefficient is roughly linearly related to the frictional velocity.

Thermal forcing
Before the thermal forcing can be calculated, the pressure at the base of the ice shelf p_b needs to be determined. It is assumed that the density of the ice shelf is constant. Since in the top of the rift the ice shelf depth is constant with a value of 15 [m], equation I.2.1.18 can be simplified to:

$$p_b = p_a + g * \rho_I * h = \frac{101325 + 9.81 * 917 * 15}{10000} = 23.6261[dBar] \quad \text{(I.3.3.6)}$$

The pressure at the base of the ice shelf is used in equation I.2.1.21 for the calculation of the freezing point temperatures T_f [°C]:

$$T_f = (0.0901 - 0.0575S_b) - 7.61 \times 10^{-4} * 23.6261 \quad \text{(I.3.3.7)}$$

From equation I.3.3.7 it can be observed that the freezing point temperature also depends on the salinity in the boundary layer between the ice shelf and the ocean. For simplicity, it is assumed that the salinity in the boundary layer can be equalized to the in-situ salinity S [PSU] in the first grid point beneath the ice shelf, an approach that is common in two-equation models as shown in D. M. Holland and Jenkins, 1999. A study by McPhee et al., 1999 shows that this assumption results in minor errors. Therefore, S_b in equation I.3.3.7 is replaced with the in-situ salinity S [PSU]. The thermal forcing is equal to the difference between the freezing point and in-situ temperature.

Freezing rate
The oceanic freezing rate q_{ocean} [> 0 m/year for freezing] can be computed by rewriting equation I.2.1.19 to:

$$q = \left(\frac{c_{p,I}\kappa_{I,T}\rho_I(T_s - T_f)}{L * \rho_c} + \frac{c_p\rho_c\gamma_T * (T - T_f)}{L}\right) * \frac{-3600 * 24 * 356}{1000} \quad \text{(I.3.3.8)}$$

In the three-equation model, q_{ocean} $[kg/m^2s]$ represents the oceanic freezing. However, this study uses ice shelf freezing q_i [< 0 m/year for freezing]. Therefore relation I.2.5.37, given in section 2.5, is applied. While substituting all the constant parameters, the following expression is obtained:

$$q_i = \left(\frac{3994 * (1.56 * 10^{-6}) * 917 * (-20 - T_f)}{334000 * 1027.5} + \frac{3994 * 1027.5 * \gamma_T * (T - T_f)}{334000}\right) * \frac{-3600 * 24 * 356}{1000}$$

The mean of the freezing rates obtained with the three-monthly mean diagnostics of run $N_{10}r_2$ is equal to approximately -0.5645 [m/year]. Furthermore, a freezing rate of approximately -0.4043 [m/year] is calculated when the three-monthly mean diagnostics of run N_0r_2 are applied. The calculated mean freezing rates can be compared to the mean values returned by the model as shown in 3.2. The flux deviation for run $N_{10}r_2$ is equal to -0.5645/-0.537 = 1.052 or +5%. For run N_0r_2 the deviation is -0.404/-0.439 = 0.920 or -8%.

Contribution diffusive flux term
The first term in equation I.3.3.8 represents the diffusive flux from the ice shelf, which is generally negligible [P. R. Holland et al., 2008]. When the diffusive term is neglected while calculating the mean freezing rates for $N_{10}r_2$ & N_0r_2, fluxes equal to -0.5648 and -0.4047 [m/year] are obtained. Since the diffusive term only increases the freezing rate with less than 0.01%, the effect is indeed negligible. Therefore, equation I.3.3.8 reduces to:

$$q = \left(\frac{c_p\rho_c\gamma_T(T - T_f)}{L}\right) * \frac{-3600 * 24 * 356}{1000} \quad \text{(I.3.3.9)}$$

3.3.2. Contribution heat transfer coefficient and thermal forcing

Equation I.3.3.9 shows that the freezing rate depends on two variables: the heat transfer coefficient and the thermal forcing. Therefore, the following can be stated:

$$q_{N_0r_2} * \frac{q_{N_{10}r_2}}{q_{N_0r_2}} = \left(\frac{c_p * \rho_c * \gamma_{N_0r_2} * \frac{\gamma_{N_{10}r_2}}{\gamma_{N_0r_2}} * (T - T_f)_{N_0r_2} * \frac{(T-T_f)_{N_{10}r_2}}{(T-T_f)_{N_0r_2}}}{L}\right) * \frac{-3600 * 24 * 356}{1000} \quad \text{(I.3.3.10)}$$

Which can be rewritten as:

$$\frac{q_{N_{10}r_2}}{q_{N_0r_2}} = \frac{\gamma_{N_{10}r_2}}{\gamma_{N_0r_2}} * \frac{(T - T_f)_{N_{10}r_2}}{(T - T_f)_{N_0r_2}} \quad \text{(I.3.3.11)}$$

The contribution of the two parameters to the increase in freezing rate between run $N_{10}r_2$ & N_0r_2 can be determined by regarding the scaling in parameter magnitude. To determine the contribution of the heat transfer coefficient, the difference between the mean magnitudes of N_0r_2 & $N_{10}r_2$ is approximated:

$$\frac{\gamma_{N_{10}r_2,mean}}{\gamma_{N_0r_2,mean}} = \frac{1.8837704825467104 * 10^{05}}{1.780966720735069 * 10^{05}} \approx 1.058 \quad \text{(I.3.3.12)}$$

Therefore, the relative increase in heat transfer coefficient magnitude for $N_{10}r_2$ when compared to N_0r_2 is approximately 5.8%. A comparable approach is used to approximate the increase in thermal forcing between the two runs:

$$\frac{(T - T_f)_{N_{10}r_2,mean}}{(T - T_f)_{N_0r_2,mean}} = \frac{-0.07799042200032935}{-0.05849646061191478} \approx 1.33 \quad \text{(I.3.3.13)}$$

Thermal forcing increases 33% when one compares run $N_{10}r_2$ to N_0r_2.

The deviations in mean freezing rate between the model output and the results from the calculations in subsection 3.3.1 result in a freezing rate increase of -0.5645/-0.4043 = 1.396 or +39.6%, which is not in line with the 22.47% found in section 3.2. Since the heat transfer coefficient does not depend on the salinity in the boundary layer, a correction must be made to the thermal forcing to obtain a proper contribution indication:

$$\frac{q_{N_{10}r_2}}{q_{N_0r_2}} * \left(\frac{1.0504}{0.9214}\right) = \frac{\gamma_{N_{10}r_2}}{\gamma_{N_0r_2}} * \frac{(T - T_f)_{N_{10}r_2} * 1.0504}{(T - T_f)_{N_0r_2} * 0.9214}$$

$$1.2247 * 1.14 = 1.058 * \left(\frac{(T - T_f)_{N_{10}r_2}}{(T - T_f)_{N_0r_2}} * 1.14\right)$$

$$1.396 = 1.058 * \left(\frac{(T - T_f)_{N_{10}r_2}}{(T - T_f)_{N_0r_2}} * 1.14\right)$$

$$\frac{(T - T_f)_{N_{10}r_2}}{(T - T_f)_{N_0r_2}} = \frac{1.33}{1.14} = 1.167$$

Gives:

$$1.2246 \approx 1.058 * 1.167 \approx 1.2347$$

Therefore, the contribution of thermal forcing compared to the heat transfer coefficient is approximately 16.7 % / 5.8 % = 2.88. The relation can be expressed as: $(T - T_f) \approx 3 * \gamma_T$.

3.3.3. Summary freezing rate rift results

Since the contribution of the diffusive flux term is negligible, the freezing rate depends on the product of two variables: the heat transfer coefficient and the thermal forcing. The heat transfer coefficient is approximately linearly related to the frictional velocity. The increase of these two factors causes the freezing rate increase in the rift when one compares the run including channels ($N_{10}r_2$) to the run without (N_0r_2). The contribution of the thermal forcing is approximately three times as large as the heat transfer coefficient.

4

Discussion

This chapter contains the model evaluation (section 4.1) and result analysis (section 4.2). Furthermore, the implications of the results of this study and possibilities for further research are discussed in section 4.3.

4.1. Model evaluation

Although a highly idealized model deviates from reality, results can be used to increase insight into physical processes when the set-up is evaluated. The evaluation in this study consists of a comparison of our model results with modelled mean basal melt rate by Rignot et al., 2013 the Thwaites Ice Shelf [Rignot et al., 2013] (4.1.1), and existing literature on rift [Jordan et al., 2014] and channel [Millgate et al., 2013] modelling (4.1.2). The comparison with the mean basal melt rate of the Thwaites Ice Shelf by Rignot et al., 2013 indicates whether our model returns reasonable basal melt rates. Furthermore, the comparison to existing rift and channel modelling literature can be used to determine whether the same physical processes are observed while using the model in this study.

4.1.1. Basal melt rate evaluation

Before comparing the model results of this study to the estimated annual basal melt rate of the Thwaites Ice Shelf by Rignot et al., 2013, it must be stressed that our model is not an accurate representation of the Thwaites Ice Shelf. This suits the research aim, which is also not to accurately reproduce the Thwaites Ice Shelf but gain insight into key physical processes concerning the potential effects of basal channels on a rifted ice shelf. As given in subsection 2.3.1, the modelled basal melt rate of the Thwaites Ice Shelf is estimated as 17.7 ± 1.0 [m/year] [Rignot et al., 2013]. Our model returns between the 2.71 [m/year] and 3.16 [m/year] (subsection 3.1), depending on the applied ice-ocean interface. With a difference of about a factor of six, the modelled basal melt rates in this study are low compared to the Thwaites Ice Shelf. This is to be expected regarding the model simplifications. The model domain size differs from the dimensions of the reference location, 4000 and 5499 km^2 respectively. A smaller domain could potentially result in smaller velocities at the ice-ocean interface and thus less melting. Furthermore, the model ice-ocean interface is simplified and the bathymetry is generic (2.2) but their shape could affect basal melting rates [P. R. Holland et al., 2008]. The initial and boundary conditions are schematized profiles from reference data measured in the proximity of the ice shelf and not underneath, while the latter would be preferable since values potentially differ and could thus affect basal melting. The measurements are also taken at a fixed moment in time. Therefore, a variation in velocity magnitude inside the cavity related to a differing wind strength is not considered, together with seasonality and tides.

Taking all the simplification into account, this comparison is only used to observe whether the model returns reasonable results in the same order of magnitude as the reference location. As the order of magnitude is comparable, the model is considered adequate to gain insight into physical processes concerning cavity circulation beneath a rifted ice shelf. The forced return flow on the ocean boundary, representing CDW and HSSW entering the cavity together with ISW leaving the cavity, does seem to roughly reproduce basal melting by the cavity circulation. As the addition of an open ocean is computationally heavy, this could be a valuable observation for future ice shelf cavity modelling studies.

4.1.2. Rift and melt channel evaluation

A comparison is made between the model results in this study and existing modelling studies on rifts [Khazendar and Jenkins, 2003;Jordan et al., 2014] and melt channels [Millgate et al., 2013]. The model is evaluated by determining whether the physical processes are comparable. The annual basal melt rate (3.1), the mean annual freezing rates (average of all negative freshwater fluxes) (3.2), the melting/freezing and horizontal flow patterns (3.2) at the ice-ocean interface of the base run, run including a rift and run including channels are used for this comparison.

Rift

Figure 3.2 shows freezing is negligible in runs excluding a rift. Therefore, it can be concluded that in this study freezing only occurs inside the rift and not along the ice shelf base. This can be explained by the chosen warm initial and boundary conditions, as the water temperature beneath the shelf base remains too high to reach the freezing point. Due to the pressure dependency of the freezing point temperature (1.1.3), only inside the rift the buoyant meltwater reaches altitudes high enough to

freeze. The freezing of marine ice in the rift is following modelling results of Khazendar and Jenkins, 2003 and Jordan et al., 2014.

This study finds an annual basal melt rate (negative and positive freshwater fluxes averaged) reduction in the presence of a rift of 1.59% (3.1). The influence of the rift on the basal melt rate is very small compared to the channels shown below, as is to be expected since channels presumably significantly reduce sub-shelf melting by altering the flow pattern [Millgate et al., 2013] (1.1.4). From figure 3.4 it can be observed that the sub-shelf flow pattern and melting near the grounding line are not significantly altered by the addition of a rift. It is reasoned that the presence of a rift only results in freezing instead of melting at that exact location of the ice shelf and thereby reduces the basal melting by a small amount. Since the basal melt rate is a mean of all ice shelf freshwater fluxes at the ice-ocean interface combined, it goes down when a certain melting area turns into a freezing area. However, the rift area is small compared to the total ice shelf base dimensions and therefore the reduction in basal melting is little. From research by Jordan et al., 2014 it is known that freezing inside the rift decreases when the ocean´s temperature is high. Therefore, the freezing in the rift depends on the chosen initial conditions. One of the most important limitations of this study is the minimal amount of runs available to analyse. Additional runs including initial and boundary conditions derived from different warm and cold areas in Antarctica would be preferable to be more comprehensive.

Melt channels

Following existing literature [Millgate et al., 2013;Gladish et al., 2012], this study finds an ice shelf mean melt rate (negative and positive freshwater fluxes averaged) reduction in the presence of basal channels: 1.59% and 11.7% respectively (figure 3.1). Basal channels alter the horizontal circulation beneath the shelf base and thereby impact the annual melting pattern near the grounding line (figures 3.3 & 3.5), as described by Millgate et al., 2013. Without channels the flow and melt pattern, which are related in terms of strength, follow the shape of a single boundary current on the Coriolis favoured side of the domain (figure 3.3). When channels are present (figure 3.5) the boundary current is replaced by a horizontal return flow in each channel. Millgate et al., 2013 define two types of channels, as discussed in subsection 1.1.4. Wide channels create a horizontal return current inside each channel and narrow channels cause a vertical overturning circulation beneath each channel. The channels applied in this study can therefore be defined as wide. Inside the channels, strong flow, and melting occurs at the flanks and keels. In contrast, little flow and melt are found at the channel crest. This is following the theory by Millgate et al., 2013, stating that the addition of 'no-flow' regions in the channel crests reduces the annual mean melt rate at the grounding line. Melting is also more evenly distributed over the ice shelf and not only concentrated near the grounding line and in the boundary current.

A limitation of this study is that it does not study the influence of narrow channels on a rifted ice shelf. The horizontal return flows in the channels would then be replaced by vertical overturning motions. The study by Alley et al., 2016 mentions a typical channel width in Antarctica of 1-5 kilometres, indicating that channels narrower than those implemented in this study will be present.

4.2. Result analysis

The three sub-questions, as stated in 1.2, are explored by referring to the three sections of Chapter 3. Each section, in chronological order, contains the results used to answer a sub-question. The influence of basal channels on basal melting of a rifted ice shelf is determined in subsection 4.2.1 while using results from section 3.1. The influence of basal channels on the circulation in the proximity of and inside the rift is explored in subsection 4.2.1 while referring to results from section 3.2. Results from section 3.3 are used to determine how the freezing inside the rift is altered by basal channels (subsection 4.2.3). A summary where all findings are combined is given in subsection 4.2.4.

4.2.1. Rifted ice shelf basal melting affected by basal channels

This study finds an annual basal melt rate (negative and positive ice shelf freshwater fluxes averaged) reduction when the ice shelf contains a rift, basal channels, and both features of 1.59%, 11.7%, and 14.2% respectively (figure 3.1). It can be observed that the influence of the rift is small compared to

that of channels. The melt reduction by only channels or a rift is explained in detail in 4.1.2. In this study, a rift causes freezing instead of melting at that exact location of the ice shelf. Since the rift area is small compared to the total ice shelf basal surface area, the resulting influence on annual basal melting is little when compared to the influence of channels. The combined presence of melt channels and a rift causes an additional 7% annual basal melt reduction when compared to the sum of the individual impacts (figure 3.1). This can be explained by the annual freezing rate inside the rift being 22.47% higher when basal channels are present (figure 3.2). The increase in freezing is likely the cause of the observed additional decrease in basal melting since it is defined as the mean value of all melting and freezing on the ice-ocean interface. The difference in the rate of change between the two factors is presumably due to dissimilarity in rift and complete shelf area.

The observations from 3.1 imply that basal channels decrease annual oceanic melting at the grounding line of a rifted ice shelf. This is an addition to observations by Millgate et al., 2013 on basal channels affecting oceanic melting of an intact ice shelf, as the driving mechanism is comparable. Basal channels alter the sub-shelf flow pattern and thereby add no-flow regions to the circulation. These no-flow regions result in regions of little melting, as the velocity magnitude is related to the freezing/melting intensity. Therefore, the annual basal melt rate is decreased. As basal channels alter the circulation beneath the ice shelf base, the flow pattern in the proximity of and inside the rift is also altered. This is further investigated below.

4.2.2. Basal channels altering circulation in and around rift

The influence of basal channels on the flow pattern in and in the proximity of the rift is analysed in this subsection. The observations from figures 3.7 & 3.8 are visualized in figure 4.1; while emphasizing the horizontal flow pattern, the freezing inside the rift, and the entrance of ice shelf meltwater into the rift. Figure 4.1 shows the ice-ocean interface of a rifted ice shelf along the ice shelf base with and without channels, from the grounding line to the ocean. The ice shelf base is shown in white and the rift in blue. The sub-shelf circulation is represented by black arrows. The places where buoyant meltwater enters the rift are indicated with turquoise arrows. When channels are present in the ice-ocean interface, their troughs are shown with light green dotted lines. When no channels are present (figure 3.7; figure 4.1, left), one large clockwise circulation occurs between the ice shelf base and the rift. As this is comparable to the sub-shelf flow pattern of the base run, the addition of the rift does not alter the cavity circulation outside the rift area. From the grounding line, buoyant meltwater rises along the ice shelf base towards the rift on the Coriolis favoured side of the domain. Therefore, buoyant meltwater enters the rift in the boundary current when no channels are present. Buoyant meltwater enters the rift on the grounding line side while it rises, and deflects due to Coriolis and leaves while sinking at the ocean side. This motion creates a single clockwise circulation in the horizontal plane at the top of the rift. In the presence of ten channels, as used in the model set-up, the single clockwise return flow between the grounding line and the rift is transformed to a clockwise return flow in each channel, from the grounding line to the ocean (figure 3.8; figure 4.1, right). Meltwater now mainly enters the rift at the Coriolis favoured flank of each channel, from the grounding line side of the rift. A generally smaller inflow also appears at the Coriolis favoured flank of each channel from the ocean side of the rift. The circulation inside the rift is transformed into multiple small clockwise return flows, one after each channel. The top of the rift shows in both cases a melt-driven flow pattern, as discussed by Jordan et al., 2014 and described in subsection 1.1.4 (figures 3.7 & 3.8). This can be determined by regarding the clockwise motion inside the rifts. Since the flow is deflected to the left in the Southern Hemisphere by the Coriolis force, a clockwise return flow inside the rift is created by the deflection of rising meltwater at the grounding line side and sinking water at the ocean side. A melt-driven flow pattern inside the rift occurs in warm water regions, which is following the chosen initial and boundary conditions.

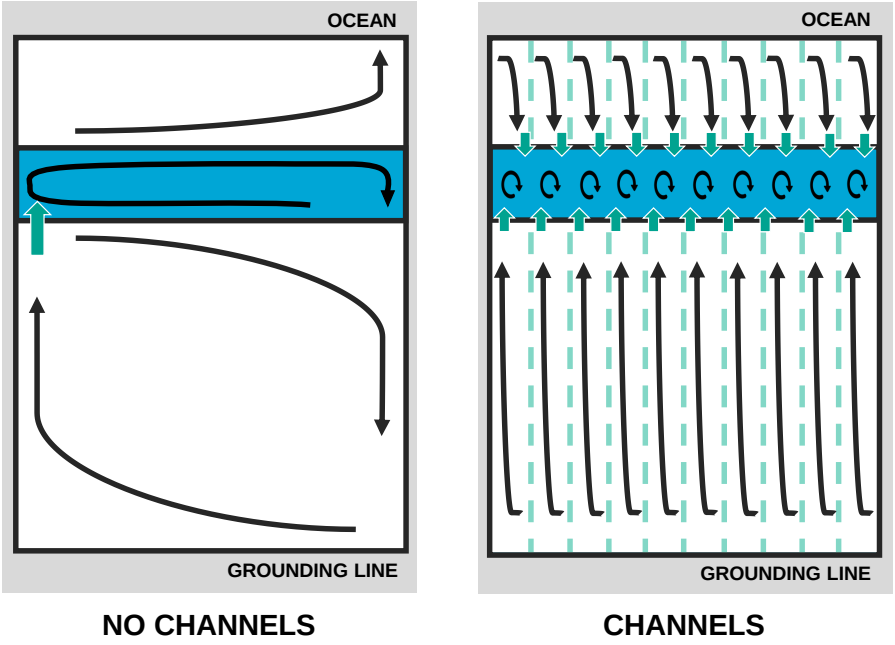

Figure 4.1: An illustration of the sub-shelf circulation along the base of a rifted ice shelf without (left) and with (right) ten basal channels. The ice shelf base is shown in white; the flow pattern is given with black arrows and the rift is represented with blue. When channels are present, the locations of their troughs are shown with light green dotted lines. The places where meltwater enters the rift are shown with turquoise arrows.

As the circulation is related to freezing/melting intensities, the flow pattern adjustment by basal channels discussed above presumably alters freezing inside the rift. Subsection 4.2.1 already briefly mentioned an increase in freezing when basal channels are present. The physical processes behind this observation are further investigated below.

4.2.3. Basal channels altering freezing inside rift

The results from section 3.3 are used to investigate the parameters influencing the freezing rate at the top of the rift and their alternation by melt channels. The freezing rate can be determined from I.2.1.19, which is a balance between the diffusive flux from the ice, the advective heat that is carried by the freshwater mass flux, and the latent heat flux due to melting and freezing. By calculating and comparing the terms and resulting mean freezing rate of two calculations, one using three-monthly mean diagnostics from a model run including a rift without and one with channels as input, the influence of the separate factors can be determined. For simplicity, the salinity in the boundary layer is equalized to the in-situ salinity at the first grid point beneath the ice shelf. When compared to the mean freezing rates in the rift returned by the model, this assumption gives a dissimilarity of about +5% when channels are included and -8 % when channels are not included.

Subsection 3.3.1 showed that the influence of the diffusive flux is negligible, and the freezing rate thus depends on the product of two variables: the heat transfer coefficient and the thermal forcing. This result is also following the study by D. M. Holland and Jenkins, 1999. Since the heat transfer coefficient equation I.2.1.23 shows no dependence on the salinity in the boundary layer, the dissimilarities of the calculated mean freezing rates mentioned above should originate from the determination of the thermal forcing that does depend on the parameter through the freezing point relation (equation I.2.1.21). To approximate the relative contribution to the freezing increase of the two factors more accurately, the enlargement of the thermal forcing is scaled with the same dissimilarity as the freezing rate. This approach does not consider round-off errors that could also influence the dissimilarity between the calculated mean freezing rates and the modelled magnitudes. However, we aim to obtain an indication of the relative influence of the two components, not an exact determination, and therefore this approach is considered to be sufficient.

Both factors in a rift increase when channels are present compared to when channels are absent. Furthermore, the increase in thermal forcing (16.7%) is approximately 2.88 times as large as the increment of the heat transfer coefficient (5.8%). The heat transfer coefficient is approximately linearly related to the frictional velocity (relation I.2.1.27), which again depends on the magnitude of the velocities in the horizontal plane u,v (equation I.2.1.26). Therefore, it can be reasoned that the change from one large return flow in a rift without melt channels to small return flows after each channel results in a generally larger horizontal velocity, friction velocity, and heat transfer coefficient. The thermal forcing is equal to the difference between the local freezing point and the in-situ temperature at the top of the rift. Subsection 4.2.2 showed that buoyant cold meltwater enters the rift after every channel instead of only in the boundary current, therefore resulting in more grid points with colder in-situ temperatures at the top of the rift. The number of grid points where the in-situ temperature is lower than the freezing point increases as well, resulting in a larger mean freezing rate when channels are present. It must be mentioned that while applying the hydrostatic pressure assumption (subsection 2.1.2), the vertical accelerations are neglected. Since this study finds an increase in meltwater entering the rift, this rising motion appears to be an important vertical movement that is not fully resolved.

4.2.4. Summary

Basal channels decrease basal melting of a rifted ice shelf near the grounding line since the sub-shelf circulation is altered. Additionally, the oceanic circulation pattern inside and in the proximity of the rift is adjusted. The boundary current on the Coriolis favoured side of the domain is transformed to a clockwise return flow in each channel. Therefore, the circulation in the rift is altered from a single clockwise return flow to one after every channel. Buoyant meltwater does not only enter the rift in the boundary current at the grounding line side but at both flanks after every channel. The flow pattern alternation results in an increase in friction velocity inside the rift, together with an enlargement of the cold buoyant meltwater that enters the rift. Both processes together result in an additional 22.47% freezing, although the contribution of the thermal forcing is approximately three times larger. Basal channels thus also increase the freezing rate inside the rift.

4.3. Implications & further research

As for an intact ice shelf [Millgate et al., 2013], it is found that basal channels decrease the basal melting of a rifted ice shelf by altering the oceanic circulation. Additionally, it is found that freezing inside a rift is increased. A higher freezing rate inside the rift suggests the additional accretion of marine ice. However, a limitation of this model is that it does not model marine ice accretion but a boundary layer flux between the ice shelf and the ocean. Marine ice consists of consolidated frazil ice, which is not explicitly modelled in this study. Therefore, a direct link between the additional freezing in the modelled rift and marine ice cannot be made. Nevertheless, the observation in this research can be seen as an indication of additional marine ice formation which does depend on freezing intensity. Further exploration of the impact of basal channels on marine ice formation could be valuable as marine ice is a component of mélange. Since mélange is thought to be mechanically resistant to iceberg calving stresses, additional marine ice and therefore presumably mélange formation could potentially delay rift propagation. A next step to increase insight into basal channels altering marine ice accretion inside rifts could be to create a 3D plume model of a rifted ice shelf including basal channels, while using the approach of Jenkins and Bombosch, 1995 as it explicitly treats frazil ice formation. Furthermore, the width of the rift in this study is constant while in reality, it is temporarily variable. The potential impact of this variability on the freezing rate inside the rift is however unknown. It might therefore also be valuable to also include multiple rift widths in such a plume model. Additionally, the ice shelf topography and bathymetry used in this study are highly idealized. A more realistic model than the one used in this study could give insight into the implications of the basal channel and rift presence for the cavity circulation and melting/freezing of a real ice shelf. This can be relevant for areas with rapid mass loss to potentially increase insight into its future response to oceanic warming. A three-dimensional high-resolution plume model could be applied while reproducing the ice-ocean interface and bathymetry of an area including basal channels

and a rift. Sections created with the 500-m resolution grid BedMachine Antarctica database [Morlighem et al., 2020] can be used as a reference while reproducing the ice-ocean interface and bathymetry. Ideally, reference data for temperature, salinity, and horizontal velocity from underneath the ice shelf base would be available to base the initial and boundary conditions of such a model on. Developments in obtaining observational data while using an autonomous underwater vehicle (AUV) in ice shelf cavities [Dowdeswell et al., 2008] could be promising in this regard.

Since basal channels and rifts are small-scale km-wide features, they are often not resolved in coarse ice-ocean models. This study implies that rift propagation might be altered by the presence of basal channels because mélange accretion is possibly enhanced. As rift propagation occurs prior to iceberg calving and basal melting has the potential to result in ice shelf thinning, basal channels could possibly alter both ice shelf change processes. Basal channels affecting these processes could especially be important as these topographic incisions mainly occur in regions that are potentially sensitive to ice sheet instabilities and rapid mass loss: the Western Antarctic Ice Sheet and the Western Antarctic Peninsula. Hence, basal channels and rifts should be included in high-resolution ice shelf cavity models to robustly reproduce oceanic circulation and basal melt. However, like in this study, when a modelled ice shelf is static, it does not include rift propagation and ice shelf thinning. Alternatively, a study using satellite imagery in high-resolution could focus on monitoring mélange thickness in the presence and absence of basal channels. A comparison of such results could possibly confirm the potential link between the presence of basal channels and mélange accretion. Furthermore, observations of ice shelf thinning rates in the presence and absence of basal channels could give further insight into a potential melt reduction at the grounding line.

5

Conclusions and recommendations

The conclusions from this study are described in section 5.1. Furthermore, section 5.2 elaborates on the most important recommendations that follow from Chapter 4.

5.1. Conclusions

In combination with unknown future emission rates, a limited understanding of Antarctic Ice Sheet mass loss causes large uncertainty in sea level rise projections important for coastal protection planning. Ice shelves, the floating parts of the ice sheet that fringe most of the Antarctic coastline, regulate sea level rise by restricting upstream snow and ice discharge toward the ocean. Antarctic ice sheet mass loss is largely controlled by ice shelf change through oceanic forcing, in the form of ice shelf thinning by basal melting and iceberg calving following the propagation of rifts. Enhanced thinning and iceberg calving presumably decrease the buttressing effect and accelerate grounded ice discharge toward the ocean. In the Western Antarctic Ice Sheet and Western Antarctic Peninsula, large ice shelf change could potentially result in ice sheet instability processes with very rapid mass loss. Knowledge of this ice shelf change is however limited, also because km-wide rift propagation is largely unexplored and generally not resolved in coarse climate models. The cavity circulation is believed to influence rift propagation as it is closely related to melting/freezing intensities. Sea water can freeze in the rift in the form of marine ice. Marine ice is one of the components of mélange, a mixture of snow and ice that could be mechanically resistant to iceberg calving stresses. When filled with mélange, rift propagation might potentially be delayed. Previous studies showed that basal melt channels alter the sub-shelf flow pattern of an intact ice shelf from a strong boundary current to multiple return flows, thereby reducing overall basal melting rates. Therefore, the cavity circulation beneath a rifted ice shelf could also be altered. Hence, the effect of basal channels on the cavity circulation of a rifted Antarctic ice shelf was not yet explored but could influence its melting/freezing.

We applied the Massachusetts Institute of Technology general circulation model to increase knowledge of the effect of basal channels on the oceanic melting/freezing of a rifted ice shelf. Since this study is the first to investigate such a potential effect, the research aimed to obtain a qualitative description of the physical processes potentially caused by melt channels on a rifted ice shelf. To this end, four simulations were performed high-resolution idealized ice shelf model domain with idealized boundary and initial conditions. Four simulations runs were performed, while only varying the inclusion of basal channels and a rift in the topography of the ice-ocean interface. The simulations correspond to a cavity with melt channels, a prominent rift close to the ice shelf front, both, and none of them. The influence of differences in bathymetry, ice shelf geometry, tides, and seasonality are neglected to be able to determine the fundamental physical processes of interest and limit computational time. This study compared the horizontal flow and melting/freezing pattern and average values as previous work showed that basal channels alter these components. The results are used to answer the research objective, expressed in one main question. Three sub-questions were defined to answer the main question. The sub-questions are first discussed in this section. As the study by Millgate et al., 2013 showed that basal channels decrease basal melting of an intact ice shelf by altering the sub-shelf flow pattern, we first determined whether this effect also occurs beneath a rifted ice shelf. Therefore, the first sub-question is:

What is the effect of basal channels on the oceanic melting of a rifted ice shelf?

Basal channels decrease rifted ice shelf basal melting near the grounding line. The driving mechanism is comparable to the one described by a previous study by Millgate et al., 2013 on basal channels affecting intact ice shelf melting. The sub-shelf flow pattern changes from a single boundary current in the simulation without channels to a horizontal return flow in each channel. The addition of no-flow regions in the channel crests reduces annual basal melt. Furthermore, the addition of only a rift does not change the ice shelf melting/freezing and velocity pattern. As basal channels decrease melting by altering the cavity circulation of the ice shelf, the flow pattern in the proximity of and inside the rift is also altered when both features are present. Therefore, the second sub-question is answered:

What is the influence of basal channels on the circulation inside and in the proximity of the rift?

Basal channels alter the flow pattern beneath the ice shelf. A solitary boundary current on the Coriolis favoured side of the domain is reformed to a clockwise return flow in each channel. As a result, the circulation in the rift changes from a single clockwise return flow to one for each channel. Buoyant

meltwater does not only enter in the boundary current but after every incision, on both flanks of the rift instead of only at the grounding line side of the rift. As the oceanic circulation is related to melting/freezing intensities, the flow pattern adjustment by the presence of basal channels can impact the freezing inside the rift. The third sub-question, to investigate this process, is:

How is the oceanic freezing inside the rift altered by basal channels?

Both the thermal forcing and friction velocity at the top of the rift are increased by the presence of basal channel topography. The thermal forcing represents the difference between the temperature at the top of the rift and the freezing point. When the water temperature at the top of the rift deviates more from the freezing point, freezing is stronger. More freezing occurs due to increasing availability of cold water with a temperature below the freezing point at the top of the rift. Additionally, the friction velocity at the top of the rift increases when channels are present. Freezing rate intensities are related to the horizontal velocity magnitude and therefore the friction velocity. The contribution of the thermal forcing is about three times as large as that of the friction velocity.

The answers from the three sub-questions were combined to answer the main research question:

What is the effect of basal channels on the oceanic melting and freezing of a rifted Antarctic ice shelf?

We found that basal channels decrease oceanic basal melting at the grounding line of a rifted ice shelf and increase oceanic freezing inside the rift.

Previous work on rift propagation suggests that the increase in freezing implies a potential increase in marine ice formation inside the rift. As marine ice is a component of mélange, which is potentially resistant to calving stresses, fracture propagation might be delayed by the presence of basal channels. The potential impact on fracture propagation and basal melting can be especially important since basal channels largely occur in the Western Antarctic Ice Sheet and Western Antarctic Peninsula, regions that could be sensitive to ice sheet instabilities and rapid mass loss. As this study did not directly model marine ice formation, further research exploring this process inside the rift when basal channels are present is recommended. Nevertheless, this study stresses the importance of including basal channels and rifts in ice shelf cavity models to robustly reproduce oceanic circulation and basal melting.

5.2. Recommendations

We created a base to increase further insight into the influence of basal channels on rifted Antarctic ice shelf melting/freezing. This section elaborates on the most important recommendations that follow from Chapter 4, to expand current knowledge with future studies.

5.2.1. Basal channels and rifts in ice shelf cavity models

We showed that basal channels alter the cavity circulation of a rifted ice shelf and alter melting/freezing. Therefore, it is recommended that basal channels and rifts are included in future ice shelf cavity models to robustly reproduce cavity circulation and basal melt.

5.2.2. Return flow at the ocean boundary in ice shelf cavity models

The intrusion of CDW and HSSW into and the exit of ISW out of the cavity were schematized by a return flow at the ocean boundary of the domain. As an open ocean is computationally heavy, we recommend using such a return flow in highly idealized ice shelf models to roughly reproduce cavity circulation.

5.2.3. A 3D plume model explicitly modelling frazil ice

We found that basal channels increase freezing inside the rift, which might imply additional marine ice accretion. Marine ice consists of consolidated frazil ice, which is not directly modelled in this study. Hence, we propose the use of a 3D plume model that explicitly models frazil ice formation to further increase insight into rifted ice shelf melting/freezing in the presence of basal channels.

5.2.4. Non-hydrostatic modelling

The vertical rising motion of buoyant meltwater into the rift is not simulated with the model used in this study. As basal channels increase the fresh meltwater enters the rift, this is however an important movement. It is recommended to perform an additional study while using a non-hydrostatic 3D plume model to simulate this motion.

5.2.5. Variation in initial and boundary conditions

The freezing rate and circulation inside the rift are related to the ocean temperature [Jordan et al., 2014]. Additional runs of the model used in this study including initial and boundary conditions derived from different warm and cold areas in Antarctica are recommended for the sake of comprehensiveness.

5.2.6. Variation in channel geometry

The influence of narrow channels on rifted ice shelves, which are observed in Antarctica [Alley et al., 2016], is not investigated in this study. As the horizontal return flow in wide channels transforms to a vertical overturning motion in narrow channels [Millgate et al., 2013], it is a natural extension of the work in this thesis to perform sensitivity runs with multiple channel widths while using our model set-up for the sake of comprehensiveness.

5.2.7. Monitoring of mélange and ice shelf thickness in the presence of channels

Previous work on rift propagation and basal melting suggests that the results of this study imply that a possible link between basal channels and ice shelf change could exist. However, static ice shelf cavity models like the one used in this study do not simulate ice shelf thinning and frontal retreat. Knowledge about the potential relationship between these two ice shelf change processes and the presence of basal channels could be increased by monitoring mélange and ice shelf thickness while using satellite imagery in high resolution. Observations of areas including and excluding basal channels can be compared. A possible link between a reduction in frontal retreat and basal channels could be suggested by comparing mélange thinning rates. A reduction in basal melting could be indicated by comparing ice shelf thinning rates.

Bibliography

Adcroft, A., Campin, J., Dutkiewicz, S., Evangelinos, C., Ferreira, D., Forget, G., Fox-Kemper, B., Heimbach, P., Hill, C., Hill, E., et al. (2008). Mitgcm user manual. *Massachusetts Institute of Technology*.

Adcroft, A., Hill, C., & Marshall, J. (1997). Representation of topography by shaved cells in a height coordinate ocean model. *Monthly Weather Review*, *125*(9), 2293–2315.

Alley, K. E., Scambos, T. A., Siegfried, M. R., & Fricker, H. A. (2016). Impacts of warm water on antarctic ice shelf stability through basal channel formation. *Nature Geoscience*, *9*(4), 290–293.

Amundson, J. M., Kienholz, C., Hager, A. O., Jackson, R. H., Motyka, R. J., Nash, J. D., & Sutherland, D. A. (2020). Formation, flow and break-up of ephemeral ice mélange at leconte glacier and bay, alaska. *Journal of Glaciology*, *66*(258), 577–590.

Bamber, J. L., Oppenheimer, M., Kopp, R. E., Aspinall, W. P., & Cooke, R. M. (2019). Ice sheet contributions to future sea-level rise from structured expert judgment. *Proceedings of the National Academy of Sciences*, *116*(23), 11195–11200.

Bassis, J. N., Fricker, H. A., Coleman, R., & Minster, J.-B. (2008). An investigation into the forces that drive ice-shelf rift propagation on the amery ice shelf, east antarctica. *Journal of Glaciology*, *54*(184), 17–27.

Bassis, J., Coleman, R., Fricker, H., & Minster, J. (2005). Episodic propagation of a rift on the amery ice shelf, east antarctica. *Geophysical Research Letters*, *32*(6).

Bentley, C. G., Thomas, R. H., & Velicogna, I. (2007). *Ice sheets*.

Bindschadler, R., Vaughan, D. G., & Vornberger, P. (2011). Variability of basal melt beneath the pine island glacier ice shelf, west antarctica. *Journal of Glaciology*, *57*(204), 581–595.

Bradley, A., Bett, D., Dutrieux, P., De Rydt, J., & Holland, P. (2022). The influence of pine island ice shelf calving on basal melting. *Journal of Geophysical Research: Oceans*, e2022JC018621.

Buckley, M. W., & Marshall, J. (2016). Observations, inferences, and mechanisms of the atlantic meridional overturning circulation: A review. *Reviews of Geophysics*, *54*(1), 5–63.

Clark, P. U., Shakun, J. D., Marcott, S. A., Mix, A. C., Eby, M., Kulp, S., Levermann, A., Milne, G. A., Pfister, P. L., Santer, B. D., et al. (2016). Consequences of twenty-first-century policy for multi-millennial climate and sea-level change. *Nature climate change*, *6*(4), 360–369.

Davis, P. E., & Nicholls, K. W. (2019). Turbulence observations beneath larsen c ice shelf, antarctica. *Journal of Geophysical Research: Oceans*, *124*(8), 5529–5550.

DeWeerdt, S. (2019). Ocean explorers delve beneath the ice. *Nature*, *575*(7782), S2–S2.

Dinniman, M. S., Asay-Davis, X. S., Galton-Fenzi, B. K., Holland, P. R., Jenkins, A., & Timmermann, R. (2016). Modeling ice shelf/ocean interaction in antarctica: A review. *Oceanography*, *29*(4), 144–153.

Dowdeswell, J., Evans, J., Mugford, R., Griffiths, G., McPhail, S., Millard, N., Stevenson, P., Brandon, M., Banks, C., Heywood, K., et al. (2008). Autonomous underwater vehicles (auvs) and investigations of the ice–ocean interface in antarctic and arctic waters. *Journal of Glaciology*, *54*(187), 661–672.

encounteredu.com. (2022).

Fahnestock, M., Abdalati, W., Joughin, I., Brozena, J., & Gogineni, P. (2001). High geothermal heat flow, basal melt, and the origin of rapid ice flow in central greenland. *Science*, *294*(5550), 2338–2342.

Fürst, J. J., Durand, G., Gillet-Chaulet, F., Tavard, L., Rankl, M., Braun, M., & Gagliardini, O. (2016). The safety band of antarctic ice shelves. *Nature Climate Change*, *6*(5), 479–482.

Gill, A. E., & Adrian, E. (1982). *Atmosphere-ocean dynamics* (Vol. 30). Academic press.

Gladish, C. V., Holland, D. M., Holland, P. R., & Price, S. F. (2012). Ice-shelf basal channels in a coupled ice/ocean model. *Journal of Glaciology*, *58*(212), 1227–1244.

Grumbine, R. W. (1991). A model of the formation of high-salinity shelf water on polar continental shelves. *Journal of Geophysical Research: Oceans*, *96*(C12), 22049–22062.

Haasnoot, M., Kwadijk, J., Van Alphen, J., Le Bars, D., Van Den Hurk, B., Diermanse, F., Van Der Spek, A., Essink, G. O., Delsman, J., & Mens, M. (2020). Adaptation to uncertain sea-level rise; how uncertainty in antarctic mass-loss impacts the coastal adaptation strategy of the netherlands. *Environmental Research Letters*, *15*(3), 034007.

Heeszel, D. S., Fricker, H. A., Bassis, J. N., O'Neel, S., & Walter, F. (2014). Seismicity within a propagating ice shelf rift: The relationship between icequake locations and ice shelf structure. *Journal of Geophysical Research: Earth Surface*, *119*(4), 731–744.

Hellmer, H. H., & Olbers, D. J. (1989). A two-dimensional model for the thermohaline circulation under an ice shelf. *Antarctic Science*, *1*(4), 325–336.

Hinkel, J., Nicholls, R. J., Vafeidis, A. T., Tol, R. S., & Avagianou, T. (2010). Assessing risk of and adaptation to sea-level rise in the european union: An application of diva. *Mitigation and adaptation strategies for global change*, *15*(7), 703–719.

Holland, D. M., & Jenkins, A. (1999). Modeling thermodynamic ice–ocean interactions at the base of an ice shelf. *Journal of Physical Oceanography*, *29*(8), 1787–1800.

Holland, P. R., Jenkins, A., & Holland, D. M. (2008). The response of ice shelf basal melting to variations in ocean temperature. *Journal of Climate*, *21*(11), 2558–2572.

Hulbe, C. L. (1998). *Heat balance of west antarctic ice streams, investigated with a numerical model of coupled ice sheet, ice stream, and ice shelf flow*.

Huybrechts, P., & De Wolde, J. (1999). The dynamic response of the greenland and antarctic ice sheets to multiple-century climatic warming. *Journal of Climate*, *12*(8), 2169–2188.

Jackett, D. R., & Mcdougall, T. J. (1995). Minimal adjustment of hydrographic profiles to achieve static stability. *Journal of Atmospheric and Oceanic Technology*, *12*(2), 381–389.

Jenkins, A., & Bombosch, A. (1995). Modeling the effects of frazil ice crystals on the dynamics and thermodynamics of ice shelf water plumes. *Journal of Geophysical Research: Oceans*, *100*(C4), 6967–6981.

Jenkins, A., Hellmer, H. H., & Holland, D. M. (2001). The role of meltwater advection in the formulation of conservative boundary conditions at an ice–ocean interface. *Journal of physical oceanography*, *31*(1), 285–296.

Jordan, J. R., Holland, P. R., Jenkins, A., Piggott, M. D., & Kimura, S. (2014). Modeling ice-ocean interaction in ice-shelf crevasses. *Journal of Geophysical Research: Oceans*, *119*(2), 995–1008.

Joughin, I., & MacAyeal, D. R. (2005). Calving of large tabular icebergs from ice shelf rift systems. *Geophysical research letters*, *32*(2).

Khazendar, A., & Jenkins, A. (2003). A model of marine ice formation within antarctic ice shelf rifts. *Journal of Geophysical Research: Oceans*, *108*(C7).

Kundu, P. K., Cohen, I. M., & Dowling, D. R. (2015). *Fluid mechanics*. Academic press.

Large, W. G., McWilliams, J. C., & Doney, S. C. (1994). Oceanic vertical mixing: A review and a model with a nonlocal boundary layer parameterization. *Reviews of geophysics*, *32*(4), 363–403.

Larour, E., Rignot, E., Poinelli, M., & Scheuchl, B. (2021). Physical processes controlling the rifting of larsen c ice shelf, antarctica, prior to the calving of iceberg a68. *Proceedings of the National Academy of Sciences*, *118*(40).

Larour, E., Rignot, E., & Aubry, D. (2004). Modelling of rift propagation on ronne ice shelf, antarctica, and sensitivity to climate change. *Geophysical research letters*, *31*(16).

Lenaerts, J. T., Medley, B., van den Broeke, M. R., & Wouters, B. (2019). Observing and modeling ice sheet surface mass balance. *Reviews of Geophysics*, *57*(2), 376–420.

Lewis, E., & Perkin, R. (1983). Supercooling and energy exchange near the arctic ocean surface. *Journal of Geophysical Research: Oceans*, *88*(C12), 7681–7685.

Liu, Y., Moore, J. C., Cheng, X., Gladstone, R. M., Bassis, J. N., Liu, H., Wen, J., & Hui, F. (2015). Ocean-driven thinning enhances iceberg calving and retreat of antarctic ice shelves. *Proceedings of the National Academy of Sciences*, *112*(11), 3263–3268.

Losch, M. (2008). Modeling ice shelf cavities in az coordinate ocean general circulation model. *Journal of Geophysical Research: Oceans*, *113*(C8).

Lumpkin, R., & Speer, K. (2007). Global ocean meridional overturning. *Journal of Physical Oceanography*, *37*(10), 2550–2562.

Mankoff, K. D., Jacobs, S. S., Tulaczyk, S. M., & Stammerjohn, S. E. (2012). The role of pine island glacier ice shelf basal channels in deep-water upwelling, polynyas and ocean circulation in pine island bay, antarctica. *Annals of Glaciology*, *53*(60), 123–128.

Marshall, J., Hill, C., Perelman, L., & Adcroft, A. (1997). Hydrostatic, quasi-hydrostatic, and nonhydrostatic ocean modeling. *Journal of Geophysical Research: Oceans*, *102*(C3), 5733–5752.

Marzeion, B., Cogley, J. G., Richter, K., & Parkes, D. (2014). Attribution of global glacier mass loss to anthropogenic and natural causes. *Science*, *345*(6199), 919–921.

McKay, N. P., Overpeck, J. T., & Otto-Bliesner, B. L. (2011). The role of ocean thermal expansion in last interglacial sea level rise. *Geophysical Research Letters*, *38*(14).

McPhee, M. G., Kottmeier, C., & Morison, J. H. (1999). Ocean heat flux in the central weddell sea during winter. *Journal of Physical Oceanography*, *29*(6), 1166–1179.

Millero, F. J., & Poisson, A. (1981). International one-atmosphere equation of state of seawater. *Deep Sea Research Part A. Oceanographic Research Papers*, *28*(6), 625–629.

Millgate, T., Holland, P. R., Jenkins, A., & Johnson, H. L. (2013). The effect of basal channels on oceanic ice-shelf melting. *Journal of Geophysical Research: Oceans*, *118*(12), 6951–6964.

Morlighem, M., Rignot, E., Binder, T., Blankenship, D., Drews, R., Eagles, G., Eisen, O., Ferraccioli, F., Forsberg, R., Fretwell, P., et al. (2020). Deep glacial troughs and stabilizing ridges unveiled beneath the margins of the antarctic ice sheet. *Nature Geoscience*, *13*(2), 132–137.

Nakayama, Y., Greene, C. A., Paolo, F. S., Mensah, V., Zhang, H., Kashiwase, H., Simizu, D., Greenbaum, J. S., Blankenship, D. D., Abe-Ouchi, A., et al. (2021). Antarctic slope current modulates ocean heat intrusions towards totten glacier. *Geophysical Research Letters*, *48*(17), e2021GL094149.

NSIDC. (2021). National snow & ice data center: Quick facts on ice sheets.

Orsi, A. H., Johnson, G. C., & Bullister, J. L. (1999). Circulation, mixing, and production of antarctic bottom water. *Progress in Oceanography*, *43*(1), 55–109.

Pachauri, R. K., & Meyer, L. A. (2014). Ipcc, 2014: Climate change 2014: Synthesis report. contribution of working groups i, ii and iii to the fifth assessment report of the intergovernmental panel on climate change.

Peltier, W. (1999). Global sea level rise and glacial isostatic adjustment. *Global and Planetary Change*, *20*(2-3), 93–123.

Pietrzak, P. J. (2020). *An introduction to stratified flows for civil and offshore engineers*.

Poinelli, M. (2022).

Portner, H., Roberts, D., Masson-Delmotte, V., Zhai, P., Tignor, M., Poloczanska, E., Mintenbeck, K., Nicolai, M., Okem, A., Petzold, J., et al. (2019). Ipcc, 2019: Ipcc special report on the ocean and cryosphere in a changing climate.

Pritchard, H., Ligtenberg, S. R., Fricker, H. A., Vaughan, D. G., van den Broeke, M. R., & Padman, L. (2012). Antarctic ice-sheet loss driven by basal melting of ice shelves. *Nature*, *484*(7395), 502–505.

Rignot, E., Jacobs, S., Mouginot, J., & Scheuchl, B. (2013). Ice-shelf melting around antarctica. *Science*, *341*(6143), 266–270.

Rignot, E., Mouginot, J., Scheuchl, B., Van Den Broeke, M., Van Wessem, M. J., & Morlighem, M. (2019). Four decades of antarctic ice sheet mass balance from 1979–2017. *Proceedings of the National Academy of Sciences*, *116*(4), 1095–1103.

Rosier, S. H., & Gudmundsson, G. H. (2018). Tidal bending of ice shelves as a mechanism for large-scale temporal variations in ice flow. *The Cryosphere*, *12*(5), 1699–1713.

Schmidtko, S., Heywood, K. J., Thompson, A. F., & Aoki, S. (2014). Multidecadal warming of antarctic waters. *Science*, *346*(6214), 1227–1231.

Shepherd, A., Ivins, E., Rignot, E., Smith, B., Van Den Broeke, M., Velicogna, I., Whitehouse, P., Briggs, K., Joughin, I., Krinner, G., et al. (2018). Mass balance of the antarctic ice sheet from 1992 to 2017. *Nature*, *558*, 219–222.

Shukla, P. R., Skea, J., Slade, R., Al Khourdajie, A., van Diemen, R., McCollum, D., Pathak, M., Some, S., Vyas, P., Fradera, R., Belkacemi, M., Hasija, A., Lisboa, G., Luz, S., Malley, J., et al. (2022a). Ipcc, 2022: Climate change 2022: Mitigation of climate change. contribution of working group iii to the sixth assessment report of the intergovernmental panel on climate change.

Shukla, P. R., Skea, J., Slade, R., Al Khourdajie, A., van Diemen, R., McCollum, D., Pathak, M., Some, S., Vyas, P., Fradera, R., Belkacemi, M., Hasija, A., Lisboa, G., Luz, S., Malley, J., et al. (2022b). Ipcc, 2022: Summary for policymakers. in: Climate change 2022: Mitigation of climate change. contribution of working group iii to the sixth assessment report of the intergovernmental panel on climate change.

Stanton, T. P., Shaw, W., Truffer, M., Corr, H., Peters, L., Riverman, K., Bindschadler, R., Holland, D., & Anandakrishnan, S. (2013). Channelized ice melting in the ocean boundary layer beneath pine island glacier, antarctica. *Science*, *341*(6151), 1236–1239.

Thompson, A. F., Stewart, A. L., Spence, P., & Heywood, K. J. (2018). The antarctic slope current in a changing climate. *Reviews of Geophysics*, *56*(4), 741–770.

Trenberth, K. E., & Caron, J. M. (2001). Estimates of meridional atmosphere and ocean heat transports. *Journal of Climate*, *14*(16), 3433–3443.

Turner, J., Bindschadler, R., Convey, P., Di Prisco, G., Fahrbach, E., Gutt, J., Hodgson, D., Mayewski, P., & Summerhayes, C. (2009). *Antarctic climate change and the environment*.

Vellinga, P., & Leatherman, S. P. (1989). Sea level rise, consequences and policies. *Climatic Change*, *15*(1), 175–189.

Wåhlin, A., Graham, A., Hogan, K., Queste, B., Boehme, L., Larter, R., Pettit, E., Wellner, J., & Heywood, K. (2021). Pathways and modification of warm water flowing beneath thwaites ice shelf, west antarctica. *Science Advances*, *7*(15), eabd7254.

Wåhlin, A. K., Steiger, N., Darelius, E., Assmann, K. M., Glessmer, M. S., Ha, H. K., Herraiz-Borreguero, L., Heuzé, C., Jenkins, A., Kim, T. W., et al. (2020). Ice front blocking of ocean heat transport to an antarctic ice shelf. *Nature*, *578*(7796), 568–571.

Walker, C., Bassis, J., Fricker, H., & Czerwinski, R. (2013). Structural and environmental controls on antarctic ice shelf rift propagation inferred from satellite monitoring. *Journal of Geophysical Research: Earth Surface*, *118*(4), 2354–2364.

Wen, J., Wang, Y., Wang, W., Jezek, K., Liu, H., & Allison, I. (2010). Basal melting and freezing under the amery ice shelf, east antarctica. *Journal of Glaciology*, *56*(195), 81–90.

Zhiyin, Y. (2015). Large-eddy simulation: Past, present and the future. *Chinese journal of Aeronautics*, *28*(1), 11–24.

Zijlema, M. (2021). *Computational modelling of flow and transport*.

A

MICI & MISI

Both MISI and MICI would be a result of a large ice shelf retreat rate and a decrease of upstream flow restriction by basal melting and iceberg calving [Portner et al., 2019]. Figure A1 shows a schematized representation of MISI and MICI, where the effect of hydrofracturing on MICI is neglected [Portner et al., 2019]. An ice shelf is shown at three phases of grounding line retreat, where the point of detachment retracts inland. The black arrows represent the buttressing effect of ice shelves and the discharge of grounded ice toward the ocean. At locations where the bedrock is below sea level and retrograde sloping, downwards towards the interior of the ice sheet, ice shelf reduction can trigger a self-enhancing mechanism called MISI (figure A.1(a)). The point where the ice detaches from the bed, the grounding line, deepens and therefore the grounding line thickness enlarges. As the relation between the seaward ice flow and grounding line thickness is non-linear, the discharge towards the ocean will increase at an accelerating rate. Furthermore, ice shelf retreat can cause the disintegration of a part of the ice shelf while producing an ice cliff (MICI) (A.1(b)). If the cliff is at least ~800 meters thick or about 100 m of ice above the water line, the stresses that occur exceed the ice strength and the cliff structurally fails. This single cliff failure can trigger multiple events, causing rapid ice shelf retreat. The potential impact of MISI and MICI on GMSL rise is large, but the timescale and likeliness of these unstable retreats and thinning processes are uncertain. Observational data on bed topography is scarce. Furthermore, future ice shelf melting and calving rates are unknown due to a limited understanding of the influence of cavity circulation.

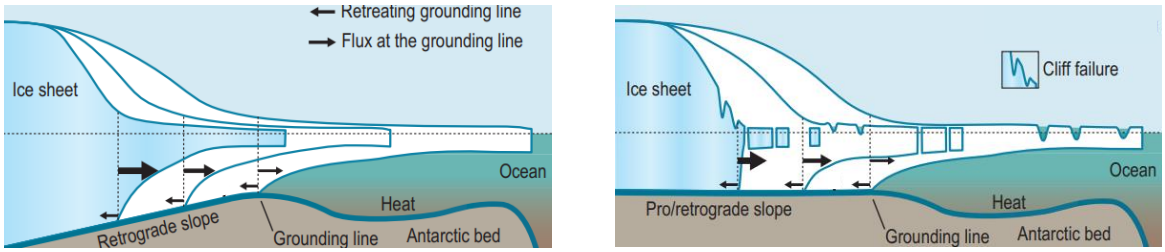

(a) (b)

Figure A1: Altered figure from Portner et al., 2019. The influence of hydrofracturing on MICI is neglected. A representation of Marine Ice Sheet Instability (MISI, a) and Marine Ice Cliff Instability (MICI, b). (a) Ice shelf retreat results in an acceleration of upstream snow and ice discharge toward the ocean. Because of the retrograding bed slope, the retreating ice shelf increases the grounding line depth and therewith the seaward ice flux. This mechanism is self-enhancing and results in even more ice shelf retreat. (b) The disintegration of an ice shelf due to its retreat causes cliff formation, if cliffs are large enough (larger than 800 m thick, or +100 m above the water line) structural failure occurs.

B

Isomorphic equations of motion

The Boussinesq incompressible oceanic equations of motion in a spherical reference frame, as described by Marshall et al., 1997, are:

$$\frac{\partial \mathbf{v}_h}{\partial t} = \mathbf{G}_{v_h} - \nabla_h p \tag{B.0.1}$$

$$\frac{\partial w}{\partial t} = G_w - \frac{\partial p}{\partial r} \tag{B.0.2}$$

$$\nabla \cdot \mathbf{v} = 0 \tag{B.0.3}$$

$$\frac{\partial T}{\partial t} = G_T \tag{B.0.4}$$

$$\frac{\partial S}{\partial t} = G_S \tag{B.0.5}$$

$$\rho = \rho(T, S, p) \tag{B.0.6}$$

Coefficient r represents either depth z [m] or pressure p [mbar], depending on the model representing the oceanic or atmospheric state respectively. The operators in a spherical reference frame and velocity components are written as:

$$\nabla \equiv \left(\frac{1}{r \cos\phi} \frac{\partial}{\partial \lambda}, \frac{1}{r} \frac{\partial}{\partial \phi}, \frac{\partial}{\partial r} \right) \tag{B.0.7}$$

$$\nabla \cdot \mathbf{v} \equiv \frac{1}{r \cos\phi} \left\{ \frac{\partial u}{\partial \lambda} + \frac{\partial}{\partial \phi}(v \cos\phi) \right\} + \frac{1}{r^2} \frac{\partial \left(r^2 w\right)}{\partial r} \tag{B.0.8}$$

$$\mathbf{v} = (\mathbf{v}_h, w) = (u, v, w) \tag{B.0.9}$$

Equations B.0.1 and B.0.2 are the horizontal momentum equation consisting of inertia, a combination term G (B.0.11, B.0.12, B.0.13, B.0.14), and a pressure term (B.0.10). Expression B.0.3 shows the continuity equation, where B.0.4 and B.0.5 are the advection-diffusion equations for temperature and salinity with combination terms B.0.15 and B.0.16. The equation of state is given by B.0.6. The pressure term and combination terms G for the momentum equations are:

$$p = \frac{\delta p}{\rho_{\text{ref}}} \tag{B.0.10}$$

$$\mathbf{G}_v = (G_u, G_v, G_w) \tag{B.0.11}$$

$$G_u = -\mathbf{v} \cdot \nabla u - \left\{ \frac{uw}{r} - \frac{uv \tan \phi}{r} \right\} - \{-2\Omega v \sin \phi + 2\Omega w \cos \phi\} + F_u \tag{B.0.12}$$

$$G_v = -\mathbf{v} \cdot \nabla v - \left\{ \frac{vw}{r} + \frac{u^2 \tan \phi}{r} \right\} - \{2\Omega u \sin \phi\} + F_v \tag{B.0.13}$$

$$G_w = -\mathbf{v} \cdot \square\mathbf{w} + \left\{ \frac{\left(u^2 + v^2\right)}{r} \right\} + 2\Omega u \cos \phi - g \frac{\delta \rho}{\rho_{\text{ref}}} + F_w \tag{B.0.14}$$

The terms in G_u, G_v, and G_w consist of advection, curvature, Coriolis, and forcing. The vertical combination term G_w also includes buoyancy. The combination terms for temperature and salinity consist of diffusion and forcing:

$$G_T = -\nabla \cdot (\mathbf{v}T) + F_T \tag{B.0.15}$$

$$G_S = -\nabla \cdot (\mathbf{v}S) + F_S \tag{B.0.16}$$

When the hydrostatic pressure assumption is made, all the terms containing w are equalized to zero. Furthermore, the vertical momentum equation B.0.2 reduces to a balance between the pressure and the buoyancy term.

C

Derivation maximum crest depth

The evolution of a single melt channel crest depth in along shelf direction is derived while using the approach by Millgate et al., 2013:

$$d_c = \begin{cases} ay^2 + by + c & \text{if } y \leq Y \ [-] \\ -d + ey & \text{if } y > Y \ [-] \end{cases} \quad \text{(C.0.1)}$$

With y the grid points in along shelf direction. One can observe that the shape starts quadratically, before becoming linear. Parameter Y represents the grid point in along shelf direction where the transition occurs and where the maximum crest depth is defined. For this study, Y is equalized to 50 [-]. Shape parameters a, b, c, d, and e depend on the chosen maximum crest depth at Y = 50. The values used for this study are dcrest,Y 100 and 150 [meters]. The derivation of the shape parameters is given below. One can assume the quadratic part has the shape of a parabola with its maximum at Y = 50. The first derivative of the equation is then equal to zero:

$$d_c' = 2ay + b = 0 \quad \text{(C.0.2)}$$

$$b = -2ay = -2a * 50 = -100a \quad \text{(C.0.3)}$$

Furthermore, the parabola starts at (y = 0, d_c = -400). Therefore, one can calculate c:

$$a0^2 + b0 + c = -400 \quad \text{(C.0.4)}$$

So, c = -400. Substituting the expressions for b and c in the first part of C.0.1 gives:

$$d_c = ay^2 - 100ay - 400 \quad \text{(C.0.5)}$$

One ends up with one equation and one unknown. Substituting the coordinates of the top of the parabola, which is known as (Y, (c + $d_{crest,Y}$)), gives parameter a.

The linear part of equation C.0.1 contains parameters d and e. Because the ice shelf base slope is gentle at this part, one should also expect a gentle channel slope. It is assumed the channel only increases by 20 meters over 320 - 50 = 270 grid points, resulting in e = 20 / 270 = 0.074. Parameter d represents the starting point of the linear channel. Therefore, d is equal to the dc value at the top of the parabola $d_{crest,Y}$ plus (Y+1) * e to correct for y ranging from grid point 51 to 320:

$$d = (c + d_{crest,Y})) + (Y + 1) * e = (c + d_{crest,Y})) + (50 + 1) * 0.074 = (c + d_{crest,Y})) + 3.774 \quad \text{(C.0.6)}$$

Using the method above, the parameters used in this study for the $d_{crest,Y}$ = 100 [m] are:

$d_{crest,Y}$	Y	a	b	c	d	e
100	50	-0.072	7.2	-400	-223.774	0.074

D

Derivation sine function channel cross-section

The evolution of the melt channels in a cross-section can be described by a sine function [Millgate et al., 2013]:

$$y = A\sin(Bx + C) + D \tag{D.0.1}$$

Where A is the amplitude, B = $\frac{2\pi}{T}$ with period T, C/B the phase shift and D the vertical shift. The amplitude is defined as the difference between the channel crest and ice shelf base:

$$A = \frac{d_c - d_k}{2} \tag{D.0.2}$$

Furthermore, the period T is equal to the maximum distance covered by one melt channel in cross shelf direction: T = $\Delta x_{channel,max}$.

$$B = \frac{2\pi}{\Delta x_{channel,max}} \tag{D.0.3}$$

A phase shift is applied to ensure the channel structure starts with a trough on the boundaries, which is in accordance with Millgate et al., 2013.

$$C = \frac{3\pi}{2} \tag{D.0.4}$$

The sine profile is vertically shifted upward. The lowest point of the sine function is then equal to the base of the ice shelf:

$$D = d_k + \frac{d_c - d_k}{2} \tag{D.0.5}$$

Substitution of D.0.2, D.0.3, D.0.4 and D.0.5 in D.0.1 gives:

$$d_{c,x} = \frac{d_c - d_k}{2}\sin\left(\frac{2\pi}{\Delta x_{channel,max}}\left(x - \frac{3\Delta x_{channel,max}}{4}\right)\right) + \left(d_k + \frac{d_c - d_k}{2}\right) \tag{D.0.6}$$

The used parameters are shown in figure D1, where $d_{c,x}$ is the channel profile in x-direction (black), d_c the crest depth (orange), d_k is the cavity base (green), and $\Delta x_{channel,max}$ the width of one channel (blue).

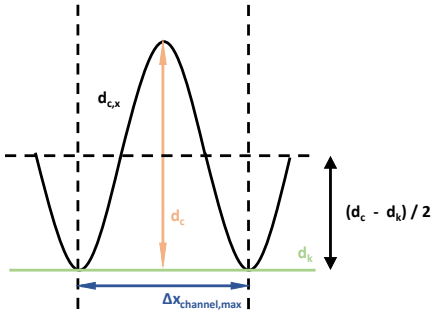

Figure D1: A visualisation of the parameters used to define the channel dimensions used in the ice-ocean interface: $d_{c,x}$ is the channel profile in x-direction, d_c the crest depth, d_k is the cavity base, and $\Delta x_{channel,max}$ the width of one channel. One channel is defined from trough to trough.

E

Reference measurements initial and boundary conditions

The potential temperature, salinity, and velocity profiles used for the initial and boundary conditions are derived from field data measured by A. Wåhlin et al., 2021. A. Wåhlin et al., 2021 measured ADCP and CTD data in two troughs near the Thwaites Ice Shelf front. Figure E1 shows the two different measurement locations in white boxes b (T2) and c (T3). Furthermore, the bed elevation is given in a colour spectrum from black (deep) to white (shallow). The hatched lines show grounded ice and its historic boundary location is indicated with different years. The black line shows the ice shelf front. The orange dots indicate the locations of CTD measurements. White stars refer to irregular ridges which are not discussed in this thesis but can be found in A. Wåhlin et al., 2021. The measurements used in this study originate from section T2 (see figure E1), as the depth is comparable to that used in the model.

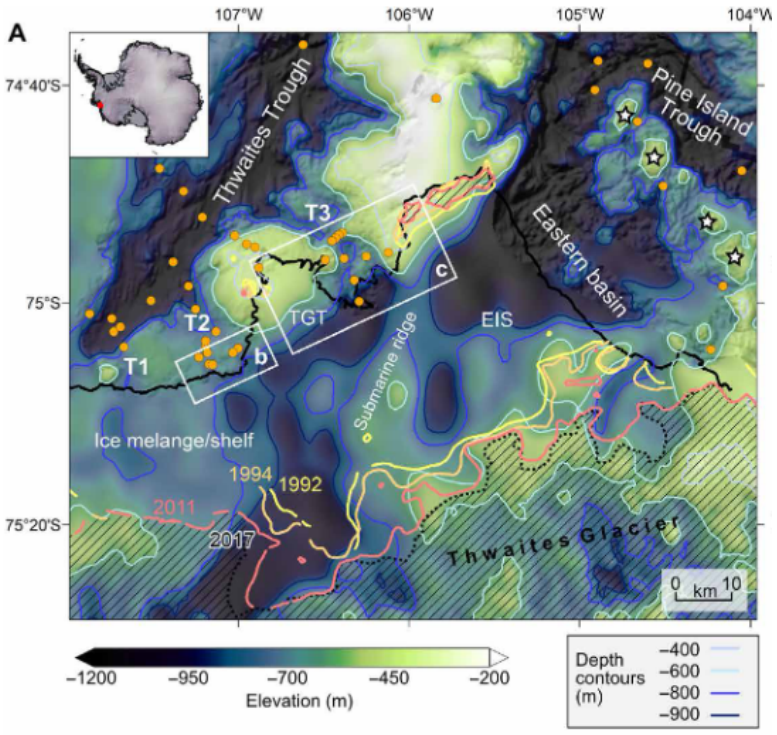

Figure E1: Detail of a figure in A. Wåhlin et al., 2021: regions of interest in A. Wåhlin et al., 2021. The bathymetry is shown in colours with notations to indicate specific areas. The hatched lines show grounded ice and its historic boundary location is indicated with different years. The black thick line represents the ice shelf front. Coloured lines visualize the grounding line in various years. Orange dots indicate CTD measurements. White stars indicate an irregular ridge which is discussed in A. K. Wåhlin et al., 2020 but not in this study.

F

Salinity time series

To determine whether the model is in quasi-steady state (2.4.2), time series of the mean salinity in the domain are shown for each run (2.6). The salinity time series of the base run N_0r_0 is given in subsection 2.4.2 (figure 2.8) and the figures corresponding to run N_0r_2, $N_{10}r_0$ & $N_{10}r_2$ are presented below (figure F1). The left figures show the monitoring time in days on the x-axis against the mean salinity of the domain. The spin-up time appears up until day 250. The period after day 250 is indicated with a grey boxes and shown in the right subfigures. Quasi-steady state is assumed to occur after five years of numerical time, Tend = 1825 [days], when the time series shows little deviation from the mean value of one year. The min, max and mean value of this period are indicated with the grey lines in the right subfigures.

It is assumed that the model is in quasi-steady state when the maximum and minimum salinity over a certain period does not deviate more than 1 % from its mean value. A year equal to 365 days is presumed to be a sufficiently long period. The maximum and minimum deviations from the mean value for the last year, from day 1460 till day 1825, are computed with:

$$\Delta_{max,min} = \frac{S_{mean} - S_{max,min}}{S_{mean}} * 100\% \qquad \text{(F.0.1)}$$

The results are shown in the table below. All deviations are below the threshold of 1 %.

Run	Reference	S_{mean} [PSU]	S_{max} [PSU]	Δ_{max} [%]	S_{min} [PSU]	Δ_{min} [%]
1	N_0r_0	34.5555596	34.5561840	0.0018	34.5542668	0.0037
2	N_0r_2	34.5355381	34.5364296	0.0026	34.5345431	0.0029
3	$N_{10}r_0$	34.4922177	34.4934738	0.0036	34.4910648	0.0033
4	$N_{10}r_2$	34.4799736	34.4815649	0.0046	34.4789870	0.0029

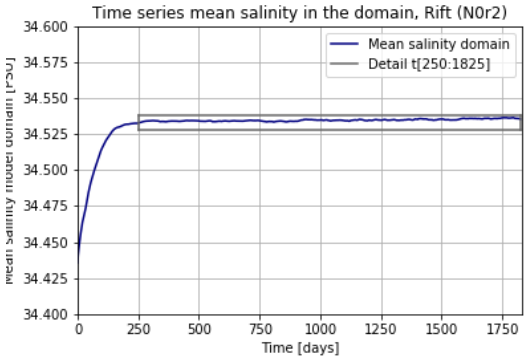

(a)

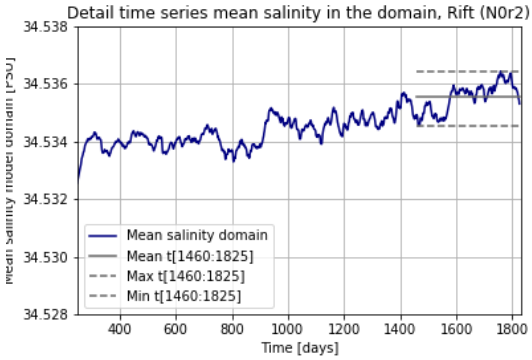

(b)

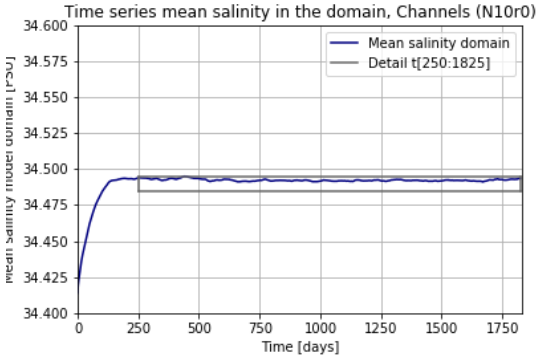

(c)

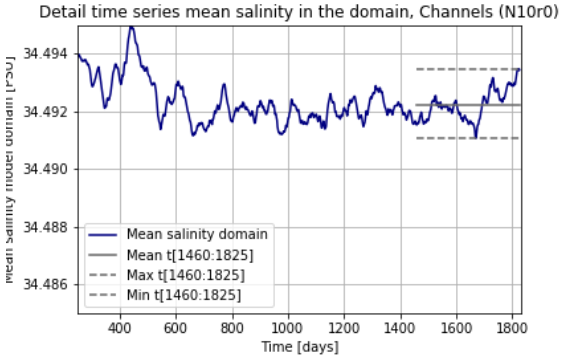

(d)

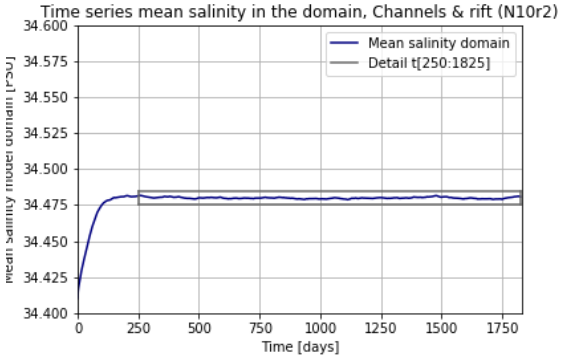

(e)

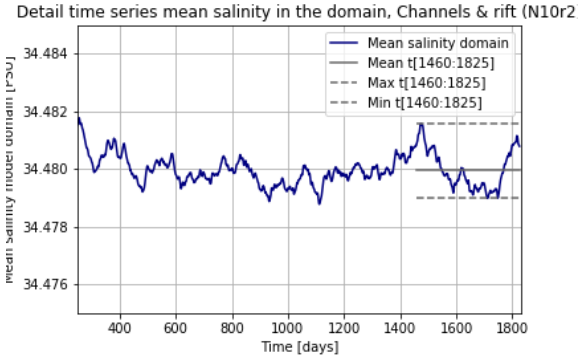

(f)

Figure F1: Monitoring time in days against mean salinity of the domain for run N_0r_2 (F.1(a)), $N_{10}r_0$ (F.1(c)) & $N_{10}r_2$ (F.1(e)). Detail from day 250 until day 1825 for run N_0r_2 (F.1(b)), $N_{10}r_0$ (F.1(d)) & $N_{10}r_2$ (F.1(f)).